



Universiteit
Leiden

The Netherlands

Living on the edge: STM studies of the creation, diffusion and annihilation of surface vacancies

Schoots, K.

Citation

Schoots, K. (2007, June 27). *Living on the edge: STM studies of the creation, diffusion and annihilation of surface vacancies*. Retrieved from <https://hdl.handle.net/1887/12101>

Version: Corrected Publisher's Version

License: [Licence agreement concerning inclusion of doctoral thesis in the Institutional Repository of the University of Leiden](#)

Downloaded from: <https://hdl.handle.net/1887/12101>

Note: To cite this publication please use the final published version (if applicable).

LIVING ON THE EDGE

**STM Studies of the Creation, Diffusion and
Annihilation of Surface Vacancies**

LIVING ON THE EDGE

STM Studies of the Creation, Diffusion and Annihilation of Surface Vacancies

Proefschrift

ter verkrijging van
de graad van Doctor aan de Universiteit Leiden,
op gezag van de Rector Magnificus prof. mr. P.F. van der Heijden,
volgens besluit van het College voor Promoties
te verdedigen op woensdag 27 juni 2007
te klokke 15:00 uur

door

Koen Schoots

geboren te Borculo
in 1978

Promotiecommissie

Promotor: prof. dr. J.W.M. Frenken

Referent: prof. dr. ir. H.J.W. Zandvliet (Universiteit Twente)

Overige leden: prof. dr. J. Aarts
prof. dr. G.T. Barkema (Universiteit Utrecht)
prof. dr. Th. Michely (Universität zu Köln, Duitsland)
dr. M.J. Rost
prof. dr. J.M. van Ruitenbeek
prof. dr. R.M. Tromp (IBM Research Division,
Yorktown Heights, USA)

ISBN/EAN: 978-90-9021923-3

The work described in this thesis was performed at the
Kamerlingh Onnes Laboratorium
Universiteit Leiden
Niels Bohrweg 2
2333 CA LEIDEN

The work is part of the research program of the
'Stichting voor Fundamenteel Onderzoek der Materie'

Contents

1	Introduction	1
1.1	General background on metal surfaces	2
1.2	Diffusion transport on metal surfaces	4
1.3	Vacancies versus adatoms	5
1.4	Evolution of surfaces with vacancy islands	7
2	Experimental setups	9
2.1	Introduction	10
2.2	Programmable temperature STM	10
2.3	Artist STM system	12
2.4	Improved programmable temperature STM system	14
2.5	Design for a UHV-pre-vacuum system for the improved programmable temperature STM vacuum system	18
3	Vacancy creation/annihilation: Experiment and analysis	23
3.1	Introduction	24
3.2	Experimental procedures	24
3.3	Qualitative observations	26
3.4	Quantitative analysis	29
3.4.1	Jump length distributions inside and outside a vacancy island	29
3.4.2	Waiting time distributions inside and outside a vacancy island	31
3.4.3	Diffusion constants inside and outside a vacancy island . . .	34
3.5	Discussion and conclusion	35
4	Vacancy creation and annihilation: Theory	37
4.1	Introduction	38
4.2	Vacancy lifetime dependence on the border length of a vacancy island	40
4.3	Exact numerical calculations	43
4.4	Exact numerical calculations application in 2D islands	47
4.5	Jump length distribution in small islands	50
4.5.1	Monte Carlo simulations	51

4.5.2	Application to jump length distributions	52
4.5.3	Application to the distribution of indium atom positions . . .	55
4.6	Recombination barrier at the upper and lower sides of a step	57
4.7	Vacancy encounter probability as a function of the distance to an ideal source-and-sink	60
4.8	Conclusion	63
5	Direct observation of the diffusion of an individual surface vacancy	65
5.1	Introduction	66
5.2	Experimental procedures	66
5.3	Qualitative observation and quantitative analysis	68
5.4	Birth, life and death of a surface vacancy in Cu(100)	69
6	Coalescence of vacancy islands	71
6.1	Introduction	72
6.2	Experimental procedures	74
6.3	Qualitative observations	75
6.4	Quantitative analysis	77
6.5	Discussion and conclusion	80
6.5.1	Accelerated Ostwald ripening	82
6.5.2	Step fluctuations	83
6.5.3	Spontaneous clustering of surface vacancies	84
6.5.4	Step interactions	84
6.5.5	Surface Stress	85
	Appendix	89
A	Image processing	89
A1	Indium recognition	89
A2	Drift correction	91
A3	Vacancy island detection	92
	References	95
	English Summary	
	Living on the Edge: Birth, Life and Death of Surface Vacancies	101
	Nederlandse Samenvatting	
	Levend op het randje:	
	Geboorte, leven en dood van oppervlakte vacatures	103
	Curriculum Vitae	107
	Nawoord	109

CHAPTER 1

Introduction

A general introduction on the subjects, discussed in this thesis, is presented in this chapter. The basic introduction is devoted to general aspects of the structure and diffusional transport on metal surfaces. The wealth of knowledge about adatoms is contrasted with the relative lack of knowledge on surface vacancies, which form the primary subject of Chapters 3, 4 and 5 of this thesis. We also discuss surface coarsening phenomena, as an introduction to chapter 6.

1.1 General background on metal surfaces

Understanding the behavior of metals is relevant because they are widely used in everyday applications. Many properties of metals such as the electrical conductance, chemical properties, but also color and reflectivity, are affected and in some cases even dominated by the surfaces. This aspect is gaining further significance as the length scale of structures in many applications are shrinking to the nanometer regime (nanotechnology), thereby strongly increasing the surface-to-volume ratio of these structures. In addition to plain curiosity, this provides a strong technological motivation to investigate the detailed, atomic-scale properties of material surfaces: surface science. The work described in this thesis concentrates on the atomic-scale surface properties of a prototypical metal surface: Cu(100).

One can imagine creating a metal surface by cleaving a larger piece of metal. Such a dramatic process does not take place spontaneously. A certain amount of energy has to be invested, the surface formation energy. Due to the reduced number of neighbors, atoms at the surface are less strongly bound than atoms in the bulk of a metal. In response to the reduced coordination at the surface, the distances between the outermost atomic layers of metals often deviate from the bulk interlayer distance, usually starting with a contraction of the distance between the outermost layers. In the case of Cu(100) this contraction has been measured to be $1.10 \pm 0.40\%$ [1]. In spite of this surface relaxation, Cu(100) has been calculated to be under a substantial tensile stress of 1.38 N/m [2]. This means that by itself, the surface would prefer a shorter in-plane lattice period than the value dictated by the underlying bulk lattice.

Only in theory a surface can be perfectly flat. In practice however, this is never the case. A variety of additional structures is usually present in or on top of a surface. An atomistic description of these structures has been introduced by Kossel and Stranski in the late twenties of the previous century [3, 4]. Their model distinguishes terraces, steps, kinks, adatoms and surface vacancies and is known as the Terrace Ledge Kink model (TLK-model). The intrinsic surface defects from the TLK-model that are most relevant for this thesis are shown in figure 1.1.

Atoms at these surface defects are even less strongly bound than atoms in a flat terrace. As a consequence, the creation of surface defects on a perfect surface involves the investment of a certain amount of energy, for example the step formation energy. In addition, there can be an energy barrier that needs to be overcome in the defect creation process and in this thesis we will encounter such a barrier for the creation of surface vacancies. Although steps can be considered defects, they can also host further (point) defects in the form of kinks (figure 1.1), again with their own characteristic formation energy.

In principle, these microscopic energies can be determined by atomic-scale observations with suitable microscopy techniques. For example, formation energies can be found directly from the observed densities of spontaneously formed defects at finite temperatures. Equivalently, activation energies can be obtained from the

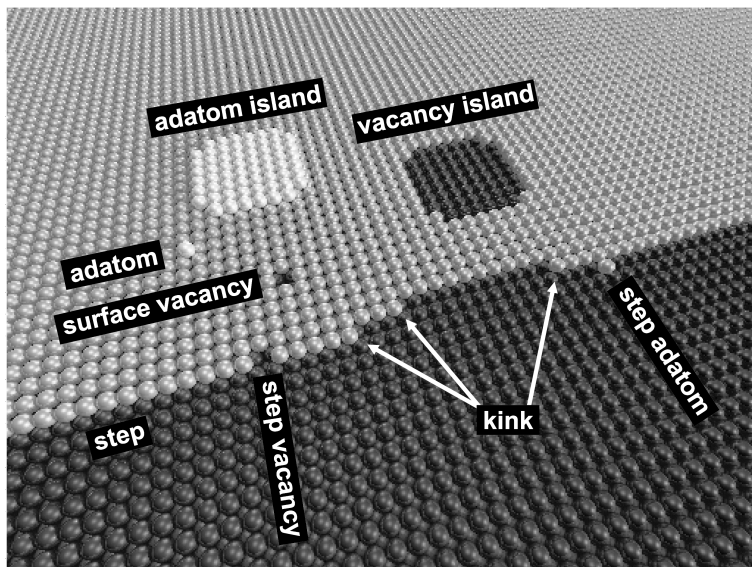


Figure 1.1: A schematic ball model of an fcc (100)-surface with several defects as defined in the TLK-model. The defects shown, are relevant for this thesis.

temperature dependence of the frequencies of the corresponding processes (diffusion, reaction, creation, annihilation). Scanning probe techniques, such as scanning tunnelling microscopy, are popular tools for these types of observations [5, 6, 7, 8]. These energies form a very fruitful testing ground for theoretical calculations of various degrees of sophistication. Although the more accurate values come from Density Functional Theory [9], empirical models, such as the Embedded Atom Model (EAM), remain very popular tools to guide the intuition and provide first numerical estimates [10, 11, 12, 13]. For the surface investigated in this thesis, Cu(100), many formation and activation energies have been predicted by P. Stolze on the basis of the Effective Medium Theory, an approach closely related to EAM [13]. Extended surface defects, for example adatom islands and vacancy islands, often consist of a set of steps and kinks that form a closed contour. The formation energy of the complete structure can be approximated by the corresponding sum of the step formation energies and the kink formation energies [14].

The roughness of homo- or heteroepitaxially grown crystals can be changed by the presence surface defects. For example, point defects often act as local growth centers, where new layers are nucleating easily. A natural role for steps is that of growth site, since they provide locations with an extra high coordination number for the new atoms. This makes that often crystal growth proceeds in so-called step-flow mode [15, 16]. However, G. Ehrlich and R.L. Schwoebel have found independently in 1966 that diffusing adatoms can experience an extra energy barrier

for a downward ‘jump’ over a step edge [17, 18, 19]. As a consequence of this Ehrlich-Schwoebel barrier, during growth, newly arriving atoms tend to stay longer on a terrace rather than to be incorporated immediately at the nearest step. This enhances the probability with which these atoms encounter each other to form new clusters and make the growth three-dimensional, i.e. rough.

In addition to the potential nucleating role of surface impurities, it has been found in the heteroepitaxial growth of semiconductors, that the addition of particular types of impurities leads to two-dimensional growth, resulting in surfaces to grow flat [20, 21, 22, 23, 24, 25, 26, 27]. The first report of a metal surface growing flat by the addition of an impurity in the form of a tiny amount of Pb on Cu(111), was published in 1988 [28]. Other combinations of metal surfaces and impurities were found later [29, 30, 31, 32, 33]. The required type of impurity is a surfactant, a substance that lowers the surface tension. The surfactant atoms tend to reside in the top layer in stead of being incorporated in the bulk of the crystal. Another essential property for the impurities added in epitaxial growth is that they stimulate interlayer transport [34, 35]. A detailed study of surfactant action on Cu(100) has been described in [36, 37].

Indium acts as a surfactant on Cu(100). In chapter 3, indium is used as a tracer particle to track the effect of the formation, diffusion and annihilation of surface vacancies [36, 38, 39, 40, 41, 42, 43]. Van Gastel et al. have determined previously that the indium atoms are the surfactant of choice for tracking vacancies. Although indium locally changes the properties with respect to the perfect, impurity-free Cu(100) surface, it was proven that its effect does not show up in the measurement of jump frequencies. Indium used as a tracer particle, is a close approximation of a “marked” copper atom.

1.2 Diffusion transport on metal surfaces

This thesis concentrates on one of the atomic-scale mechanisms of material transport, namely surface diffusion. Traditionally, this phenomenon is associated with the motion of adatoms, hopping over the surface between lattice positions. In figure 1.2 the corresponding energy landscape is shown. An adatom is indicated in the figure on the upper terrace. It resides in a local energy minimum, pictured as a hollow site between terrace atoms. Diffusion is a thermally activated process. In order to get to one of the neighboring energy minima, the adatom has to overcome the energy barrier for diffusion E_D . The direction in which the adatom makes its next move is left to chance. The attempt frequency ν_0 , with which the adatom tries to overcome E_D is in the order of a typical phonon frequency of 10^{13} Hz. The successful fraction of these attempts to jump is governed by the absolute temperature T . The average jump rate ν_D of adatom diffusion on the surface is expected to

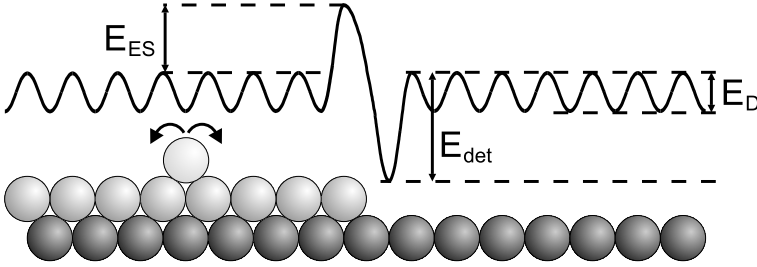


Figure 1.2: The energy landscape of an adatom diffusing over a terrace and crossing a step. The activation energy barrier for diffusion over the terrace is E_D . In order to cross the step edge, the adatom has to overcome the Ehrlich-Schwoebel barrier E_{ES} . After crossing the step, the adatom is attached to the downward side of the step. The activation energy barrier for detachment from the step E_{det} has to be overcome, before the adatom can proceed diffusing over the lower terrace.

follow the Arrhenius relation

$$\nu_D = \nu_0 e^{-\frac{E_D}{k_B T}} \quad (1.1)$$

where k_B is the Boltzmann constant.

In the energy landscape of figure 1.2 the adatom that encounters a downward step experiences an energy barrier to jump over the step that is higher than the regular energy barrier E_D for terrace diffusion. The excess activation energy at the step edge is the Ehrlich-Schwoebel barrier E_{ES} that was already mentioned before [17, 18, 19]. The deep minimum in the energy landscape in figure 1.2 indicates that the energetically most favorable position for an adatom is at the lower side of the step. One should imagine that in addition to the one-dimensional situation depicted in figure 1.2 the step adatom can diffuse along the step (usually with a relatively modest activation barrier) until it reaches a kink position where it will lose its ‘adatom’ character. The deep energy minimum at the step corresponds to an almost prohibitively high barrier E_{det} for a step adatom to escape onto the terrace.

Adatoms are not the only species responsible for atomic scale mass transport on a surface. In this thesis, the ‘life cycle’ of the morphological counterpart of an adatom, a surface vacancy, is investigated. In chapter 3 and chapter 4, the creation and annihilation of surface vacancies in Cu(100) is discussed. The search for the activation energy for the diffusion of a surface vacancy, through a Cu(100) terrace is described in chapter 5. We will see that in the case of Cu(100) the vacancies play a significant role in the mobility of the surface as a whole.

1.3 Vacancies versus adatoms

The TLK model defines adatoms as single atoms placed on top of a terrace, while vacancies are positions in a terrace, where one single atom is absent. Adatoms and

vacancies are each others morphological counterpart (figure 1.1). Both species can play a major role in transport on surfaces.

In spite of the obvious symmetry between adatoms and vacancies, most experimental and theoretical research on atomic-scale surface diffusion has focused on adatoms. The activation energy for the diffusion of adatoms on Cu(100) has been experimentally determined to be between 0.36 eV and 0.40 eV [44, 45, 46, 47]. Experimental work on step-flow growth on this surface has revealed the existence of an Ehrlich-Schwoebel barrier for adatoms descending from a step [48]. In more detailed studies, the Ehrlich-Schwoebel barrier for adatoms on Cu(100) was determined to be 0.15 eV [49]. However, in the same work a different path was revealed for the descent of an adatom from a step via a kink (Kink-Ehrlich-Schwoebel barrier $\approx 0.41\text{ eV}$). The activation energy for the detachment of an adatom from a kink was found to be 0.65 eV [50], while the activation energy for the diffusion of an adatom along a step edge is $0.45 \pm 0.09\text{ eV}$ [51]. Next to experimental work, effective medium theory calculations [13] and embedded atom model calculations [52, 53] have been performed to investigate the life cycle of adatoms. Two mechanisms by which adatoms diffuse over a flat Cu(100) surface are conceivable, exchange diffusion and simple hopping. Calculated diffusion barriers for adatoms on a flat Cu(100) surface are in favor of the simple hopping mechanism [54, 55].

The large body of available knowledge on the formation, diffusion and re-incorporation of adatoms contrasts with how little is known about surface vacancies. Early STM observations by Flores et al. of the diffusion of manganese incorporated in Cu(100) have been interpreted as an indication that surface vacancies indeed contribute to atomic mobility on/in a metal surface [56, 57]. The interpretation in terms of vacancy mediated diffusion on Cu(100) was further put on solid, quantitative ground by Van Gastel et al., who indicated the analogy with the rearrangement that is possible in the square lattice of a slide puzzle and therefore named the phenomenon "the atomic slide puzzle" [38, 39]. In the experiments by Van Gastel, indium atoms, incorporated in the top layer of Cu(100), were used as tracer particles. The motion of the indium atoms, like the manganese atoms in [56, 57], reflects the vacancy mediated diffusion of all the copper atoms in the surface. Somfai et al. have performed both analytical and numerical calculations of the probabilities for a vacancy to return to an embedded indium atom from each of the four nearest-neighbor sites, following a previous encounter. An important element in these calculations is that the vacancy is given a non-zero probability not to return to the indium atom but to annihilate instead and, thus, terminate the sequence of displacements of the indium atom. Using the calculated return probabilities, Somfai et al. were able to compute the distribution of vacancy-induced displacements of the indium atoms [42]. Although the shape of this distribution immediately corresponded convincingly with the measurements of Van Gastel et al., a quantitative fit was only possible when also the attractive interaction between the embedded indium atom and the surface vacancy was taken into account. This attraction makes

the jump length distribution of the indium tracer particles wider, but hardly affects the shape of this distribution. Van Gastel et al. have further measured that the temperature dependence of the jump rate of the indium atoms in Cu(100) follows Arrhenius behavior (equation 1.1), demonstrating the thermally activated nature of the process. From the slope of the Arrhenius plot they derived that the sum of the formation energy of a surface vacancy and the activation energy for its diffusion is $717 \pm 30 \text{ meV}$ [41]. First-principle calculations by Grant et al. predict a value for the formation energy of a surface vacancy in Cu(100) of 474 meV [58]. The high formation energy means that at room temperature, the density of vacancies is very low, only approximately 1 in 10^9 atoms is missing. On the other hand, the low activation energy for the diffusion of surface vacancies, which should be the difference $717 - 474 = 243 \text{ meV}$, makes their jump rate at this temperature very high $\approx 10^8 \text{ Hz}$. The product of these two extreme numbers, vacancy density times vacancy jump rate, is in the order of 0.1 Hz , which shows that surface vacancies are indeed important for transport on the surface at room temperature; on average every ten seconds, all atoms in Cu(100) are displaced by a surface vacancy.

Several intriguing questions about surface vacancies have remained unanswered. For example the work of Flores et al. and Van Gastel et al. contained clear indications that surface vacancies are created (and annihilated) primarily at steps. In this respect, we are interested in precise formation mechanisms and the formation and activation energies involved. An important aspect of this matter is formed by the difference between the two sides (upper and lower) of the step, which must be present in the creation and annihilation behavior of surface vacancies. For example, it may well be that a surface vacancy experiences an extra energy barrier, equivalent to the Ehrlich-Schwobel barrier for adatoms, when it approaches the step from one of the two sides. These issues form the core of Chapters 3 and 4 of this PhD thesis. Another issue is the combination of the vacancy formation energy and the vacancy diffusion barrier. As explained above, Van Gastel's measurements have provided an experimental value for the sum of these energies. Chapter 5 presents a low-temperature experiment from which we obtain an accurate estimate of the diffusion barrier and thereby can also determine the vacancy formation energy. Together, these energies provide a detailed energy landscape, quantifying the essential aspects of the formation, mobility and annihilation ('birth, life and death') of vacancies in the Cu(100) surface.

1.4 Evolution of surfaces with vacancy islands

The last chapter of this thesis is devoted to the evolution in time of surfaces with a high density of vacancies, much higher than the equilibrium density of e.g. 10^{10} at room temperature, mentioned in the previous section. High vacancy densities can be obtained by deliberate ion erosion of a flat metal surface [59, 60, 61, 62].

When given enough mobility, the vacancies cluster into vacancy islands with a well-defined equilibrium shape and with a depth of a single monolayer. As a function of time, the configuration of vacancy islands will tend to evolve to larger length scales, thus steadily reducing the density of steps on the surface.

Two main general coarsening mechanisms can be recognized [63, 64], which apply to the evolution of ensembles of both adatom islands and vacancy islands and will be briefly discussed here in the framework of the coarsening of vacancy islands. In the process of Ostwald ripening, single vacancies are exchanged between the vacancy islands [65]. This type of coarsening is driven by the fact that the local density of surface vacancies, in the direct vicinity of a small vacancy island is higher than that close to a large vacancy island.

The alternative coarsening mechanism is coalescence dynamics, where vacancy islands fluctuate in position and shape. When two of these structures encounter each other they merge into a single, larger island which evolves towards its equilibrium shape [66].

Shape and position fluctuations of a vacancy island can take place by diffusion of individual vacancies or adatoms across the island or along its perimeter or by the statistics of the exchange of vacancies between the island and its surroundings [8, 67]. The merger of islands leads to a reduction in the total step length, which again serves as the energetic driving force for the evolution. This ripening mechanism is also called Smoluchowski ripening, after Smoluchowski, who formulated the theory for kinetic coalescence in 1916 [68]. Static coalescence is only observed during growth, when immobile islands touch because of their increasing sizes.

In chapter 6, we investigate the dynamic coalescence events of neighboring vacancy islands in the Cu(100) surface. Our observations reveal a peculiar feature. Vacancy islands are found to always merge prematurely, i.e. before the islands touch. An explanation for this early coalescence behavior is presented in terms of the tensile stress in the surface, which is argued to lead to a mechanical instability for the remaining portion of the first atomic layer between two nearby vacancy islands.

CHAPTER 2

Experimental setups

This chapter presents the principles of the programmable temperature scanning tunnelling microscope (STM) used for the experiments performed in this thesis. The experimental setups on which the experiments were performed are described, including the design for a pre-vacuum system for a new, combined variable temperature setup. This new setup has two main chambers where two scanning tunnelling microscopy experiments can run independently at the same time.

2.1 Introduction

All measurements in this thesis were performed in ultrahigh vacuum (UHV). Two different setups were used. The measurements of chapter 3 were performed in the Artist STM vacuum system, described in [69, 70, 71, 72]. The measurements of chapter 5 were performed in the improved programmable temperature STM vacuum system, described in [73]. In section 2.2 the principle of the programmable temperature STM is explained. Sections 2.3 and 2.4 briefly describe these two UHV-setups. Finally, in section 2.5, a design for a pre-vacuum system for the combined version of the Artist setup and the improved programmable temperature STM setup is proposed, which enables users to simultaneously use the two setups.

2.2 Programmable temperature STM

Many atomic processes on surfaces can be monitored using a scanning tunnelling microscope. Since the birth of the STM technique in the early 1980's [74, 75], scanning probe microscopy has developed in several directions. Scanning tunnelling microscopy makes use of the tunnel current between two (semi-)conductors that are biased with respect to each other by a modest voltage. When one of the two is a flat surface and the other is shaped in the form of an atomically sharp tip, this tunnel current has a typical magnitude of 1 nA when the two (semi-)conductors are between 0.5 and 1.0 nm apart. The tip is usually addressing a rectangular area of the surface, by scanning over it line-by-line, building up a two-dimensional map of the local density of states at the surface [76, 77]. Two approaches can be followed. One, called 'constant current mode', where the tip height is continually adjusted to keep the tunnel current constant, and thus the motion of the tip is recorded, which follows a contour of more or less constant electronic density of states at the Fermi level (assuming a low tunnelling voltage). The other approach, called 'constant height mode', is to keep the vertical position of the tip unchanged and record the changes in the tunnel current. The resolution of the scanning tunnelling microscopy technique is such that individual atoms can be distinguished.

In the design of the STM that is used for all the measurements in this thesis, special attention has been paid to the thermal behavior of the STM and the mechanical (and electronic) behavior of the STM at high tip speeds (0.02 mm/s). The STM is used to follow dynamic processes on surfaces. The speed at which these processes take place strongly depends on the nature of the specific process and on temperature. In the ideal case, the STM should be fast enough for the image rate to keep up with the process of interest. Furthermore, it should be possible to follow the process at a range of temperatures. If the thermal properties of one particular feature on the surface are to be followed, the STM should compensate thermal expansions in all directions sufficiently, to allow one to keep imaging the same field of view over the

full temperature range of interest.

Thermal expansions usually cause the tip of an STM to move over several tens of nanometers in uncontrolled directions if the temperature is changed by only one degree. With a lateral scan range of typically $1.0 \mu\text{m}$ and a vertical range of about $0.5 \mu\text{m}$, this means that only temperature variations up to some 10 K are possible within one measurement session with a standard STM, whereas temperature variations of several hundreds of degrees are often interesting. The STM used in this thesis is a programmable temperature STM. It consists of two separable parts. It is equipped with a scan head, designed by L. Kuipers et al. [69, 70], that compensates for thermal drift in the vertical direction. The scan head rests on the base of the STM of which the top plane serves as a reference plane. All thermal expansions of the sample and the sample holder in the vertical direction act away from this reference plane in such a way that the surface of the sample is geometrically fixed to coincide with this plane. Thermal drift in the lateral direction is compensated in the base of the STM, designed by Hoogeman et al. [71, 72]. The key element in this design is a sample holder that is forced to slide symmetrically with respect to the base of the STM in case of temperature changes. The layout of the scan head on top of the STM base is shown in figure 2.1, a detail view of the sample holder is shown in figure 2.2. The legs of the scan head are made out of a material that has the same

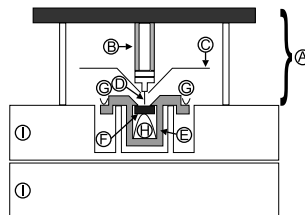


Figure 2.1: *Cross section of the programmable temperature STM. A.) the scan head, B.) the scan piezo, C.) the heat shield protecting the scanpiezo, D.) the STM tip, E.) molybdenum sample holder, F.) the sample, G.) leaf springs pushing the sample holder into the base of the STM, H.) leaf spring pushing the sample onto ridges in the reference plane, I.) molybdenum STM base. After [72].*

thermal expansion properties as the combination of the scan piezo, the tip holder and the STM tip. The legs of the scan head rest on the STM base, whose top provides the reference plane. The three legs are mounted such that they are rotationally symmetric around the STM tip. The STM tip is mounted such that it ends exactly in the reference plane. The sample is pushed from underneath by a leaf spring onto ridges. These ridges keep the sample surface in the reference plane, while the leaf spring allows expansions of the sample with respect to the reference plane. The STM tip is located next to the stable center D of the sample holder, 1 mm off the axis F in figure 2.2a. The sample holder rests on the knife edges E in figure 2.2b. The knife edges E are also in the reference plane. The sample rotates around axis F

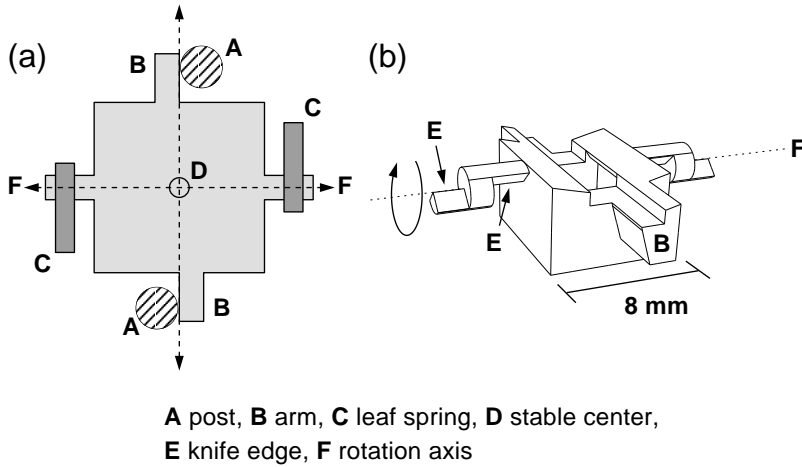


Figure 2.2: a.) Schematic top view of the sample holder. b.) Perspective view of the sample holder. After [72].

in order to approach the sample towards the tip. The knife edges E are pushed by two equally strong leaf springs C on ramps that are oriented such that the sample holder naturally rotates in a clockwise direction around the stable center D. In order to stop this rotation, the sample holder rests with its arms B against the posts A. Like the ramps, the posts A are part of the STM base. The sample is now fixed without being over-defined. The only motion it can make is pivoting around axis F. If the sample is clamped symmetrically in the sample holder and if sample and holder have the same temperature, the only residual thermal drift is a lateral drift that stems from the difference in expansion of the sample material and the (Mo) holder over 1 mm distance between the stable point D and the actual tip location. For a typical expansion coefficient difference of $5 \cdot 10^{-6} K^{-1}$ and a lateral scan range of $\pm 1.5 \mu m$, this provides a 300 K temperature range over which the sample temperature can be changed while keeping the same field of view, without the need for mechanical repositioning [71].

2.3 Artist STM system

All measurements in this thesis have been performed on a Cu(100) sample. Copper is a reactive metal. In order to keep the metal clean over a measurement time of several hours, we have performed the measurements shown in chapter 3 inside a UHV system with a base pressure of $1 \cdot 10^{-10}$ mbar. Apart from STM, other techniques were used to characterize the sample while it was cleaned. These techniques, in particular low energy electron diffraction (LEED) and Auger electron spectroscopy (AES), only work in a UHV environment.

A schematic drawing of the Artist STM vacuum system is shown in figure 2.3. The main chamber of the system is made out of a machined solid stainless steel block. This makes the system heavy and stiff and thus reduces vibrations in the microscope. The system is continuously pumped with an ion getter pump (MECA2000) and a titanium sublimation pump (Riber). The system is pumped down from atmospheric pressure with a small 50 l/s turbo-molecular pump (Pfeiffer-Balzars). This turbo-molecular pump is also used during bake-out and during the ion-erosion treatments when cleaning the sample. The ion erosion is performed with an ion gun (Riber). Connected to the main chamber is a load-lock, fitted with a 50 l/s turbo-molecular pump (Pfeiffer-Balzars) for pumping from atmospheric pressure and bake-out together with a small 50 l/s ion-getter pump (MECA2000) for continuous pumping. This chamber is mainly used for transferring samples and STM scan heads into the main chamber without breaking the vacuum of the main chamber. Scan heads and sample holders are transferred into the main chamber on a small "serving tray" mounted to a linear drive motion feedthrough. Wobble sticks inside the main chamber enable users to transfer sample holders and scan heads to the STM base.

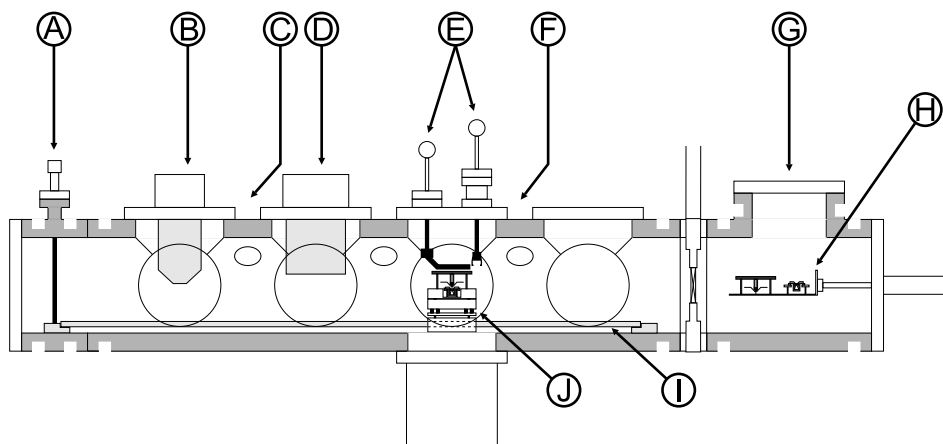


Figure 2.3: Schematic view of the ARTIST STM vacuum system. A.) rotary drive motion feedthrough for moving the STM base with the sample holder. B.) Cylindrical mirror analyzer for AES. C.) Quadrupole mass spectrometer. D.) LEED. E.) Wobble sticks. F.) Flow cryostat. G.) load lock. H.) serving tray on a linear drive motion feedthrough. I.) monorail, J.) programmable temperature STM.

The main chamber is equipped with a quadrupole mass spectrometer (Balzers) for residual gas analysis. Apart from the STM, the composition and structure of the surface of samples can be analyzed with a cylindrical mirror analyzer for AES (Perkin-Elmer) and a LEED system (Vacuum Generators). The sample holder is mounted inside the upper part of two stacked molybdenum blocks. This heavy con-

struction is supported by springs which rest on a stainless steel plate. The complete construction is mounted on top of a carriage which can move along a monorail through the whole main vacuum chamber. The carriage is pulled and pushed by a locomotive that also acts as a support for the electrical connections for the STM. The locomotive is moved by a chain that is driven via a rotary drive motion feedthrough. Without the scan head on top of the stacked molybdenum blocks, this transport mechanism can move the sample underneath all the preparation and analysis equipment. When STM measurements are performed, the scan head is placed on top of the stack of molybdenum blocks with use of the wobble sticks. During measurements the sample can be heated up to 1100 K with a filament, or cooled down to $90 \pm 10\text{ K}$ with a flow cryostat (Oxford Instruments) using liquid helium.

The main chamber is mounted on an optical table, which rests on air suspension legs (Newport). The whole system is placed on a laboratory floor with a separate foundation for optimal vibration decoupling from the rest of the building.

2.4 Improved programmable temperature STM system

The measurements of chapter 5 were performed in an improved version of the setup described in section 2.3. The design and details of this setup have been presented in [73]. The main chamber, shown in figure 2.4, consists of a large cylindrical vessel with a diameter of 0.5 m . The base pressure of this vacuum chamber is $2 \cdot 10^{-10}\text{ mbar}$.

The system is pumped from atmospheric pressure with a 170 l/s magnetically levitated turbo-molecular pump with an integrated drag pump (Pfeiffer Vacuum). The vibration levels of this pump are low. It is possible to use this pump, even without completely destroying atomic resolution during STM measurements. The system is further equipped with a 410 l/s ion getter pump (Varian) and a titanium sublimation pump (Varian) integrated in a cold trap which can be cooled to 77 K using liquid nitrogen. A quadrupole mass spectrometer (Pfeiffer Vacuum) is mounted for residual gas analysis. The system is fitted with a combined LEED/AES system (OCI Vacuum Microengineering) to determine the structure and composition of the sample surface.

The STM is mounted on a carousel inside the vacuum system. This allows for the positioning of the sample underneath cleaning and analysis equipment. Together with a wobble stick, the transport mechanism also allows for the insertion and removal of scanners and sample holders. The rotation mechanism is described in detail in [73].

The samples are cleaned by ion erosion treatments, using a differentially pumped focussed ion gun (SPECS) fitted with a Wien mass filter. The ionization chamber of this ion gun is pumped with a 70 l/s turbo-molecular pump (Pfeiffer Vacuum). The advantage of the differentially pumped ion gun is that the main chamber does not

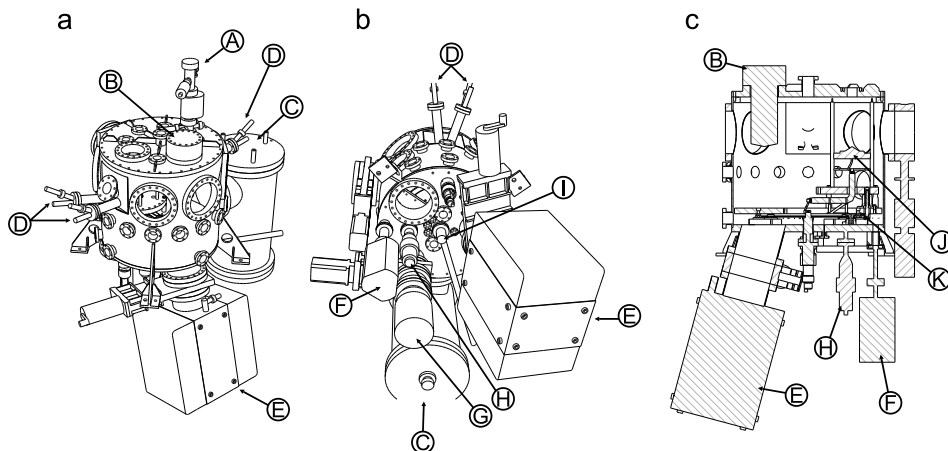


Figure 2.4: *Different views of the main chamber for the new programmable temperature STM. a.) top-side view. b.) bottom side view. c.) cross-section view. The equipment connected to the setup consists of: A.) a differentially pumped, focussed ion gun. B.) a LEED/AES system. C.) a titanium sublimation pump with an integrated cold trap. D.) Knudsen cells. E.) an ion getter pump. F.) a quadrupole mass spectrometer. G.) a turbo molecular pump. H.) a motor for driving the transport mechanism. I.) a flow cryostat. J.) programmable temperature STM on top of an eddy current damping system. K.) carousel for transport through the main chamber.*

have to be flooded with the sputter gas. While the ionization chamber of the ion gun is flooded to $1 \cdot 10^{-4}$ mbar during ion erosion treatments, the pressure in the main chamber with all the pumps running does not exceed $3 \cdot 10^{-9}$ mbar. Together with the mass filter, this geometry only allows the ions of choice to reach the sample. Before the ion gun was put into operation, the ion beam was focussed using beam profile measurements with a Faraday cup mounted on the carousel inside the main chamber. The ion gun was focussed to a current density of $1.4 \cdot 10^{-3}$ A/m² with a beam diameter of 9 mm at the sample.

The latest generation of the programmable temperature STM (Oxford Instruments) was fitted into the main chamber. We have improved this version of the STM in terms of vibration isolation, electrical shielding, thermal stability, temperature measurements and sample cooling. The vibration isolation was improved by suspension of the STM from long springs and adding an eddy current damping system instead of the small push springs underneath the STM in the Artist version of the microscope. The electronic noise in the tunnel current in the setup was reduced by carefully shielding the complete path of the signal wire of the tunnel current from the tip up to the pre-amplifier. Also the signals driving the scan piezo have been carefully shielded. Another measure against electronic noise is to use a buffer amplifier for the tunnel bias voltage with a low pass filter. This amplifier is mounted at an electrical feedthrough, directly outside the main UHV chamber. The used STM

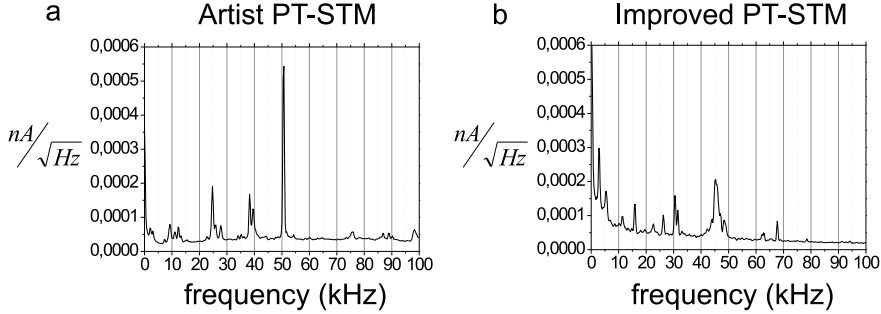


Figure 2.5: *The frequency spectra of the tunnel current noise of a.) the Artist STM described in section 2.3 (courtesy M.J. Rost) and b.) the improved programmable temperature STM described in this section. Both spectra were taken while tunnelling with 0.5 V at 0.1 nA and with the same feedback settings on Cu(100).*

electronics (Leiden Probe Microscopy) is described in [78]. The thermal stability was improved by thermally decoupling the sample holder from the rest of the STM base. The STM base is thermally anchored to the rest of the setup which is at room temperature. This way the temperature variations in the scanner are kept small. Even when the sample is cooled to 77 K for several hours, the STM base does not cool down further than 273 K. The retarded and reduced temperature variations of the base of the STM slows down the thermal drift compared to the Artist version of the STM.

A comparison of the tunnel current noise frequency spectrum between the Artist STM and the improved programmable temperature STM is shown in figure 2.5. The peaks of the improved version are shifted to lower frequencies. The amplitudes of the frequencies above 20 kHz of the improved STM are lower than those of the peaks above 20 kHz in the Artist STM. The improved version has fewer peaks below 20 kHz. Unfortunately, the amplitudes at 2.9 kHz, 5.5 kHz and 16 kHz are higher than in the Artist STM. This might be caused by the construction that provides the thermal decoupling between the sample and the STM base. In this construction, the sample holder carrier is suspended from the STM base with three thin arms.

The setup is fitted with a flow cryostat (Oxford Instruments) to cool down the sample. The cryostat is cooled down using liquid helium. The cryostat is connected to the sample via a cold finger from which the cooling path splits in two parts. These parts have been made of copper braids with a junction half way. These junctions are mechanically fixed to the vacuum chamber (with minimal thermal connection) to provide vibration isolation between the sample and the cryostat. The lowest temperature achieved in the first cooling runs with the new programmable temperature STM was 77 K. This is higher than the 20 K calculated by Rost et al. on the basis

of the available cooling power, the materials and the dimensions involved [73]. In order to diagnose the cause of this big discrepancy, we measured the temperatures at various locations on the cooling path, while cooling down the sample. The result is shown in figure 2.6. The cause of the lack of cooling performance can be found in a heat leak in the junction, right underneath the STM base, nearest to the wall of the main chamber.

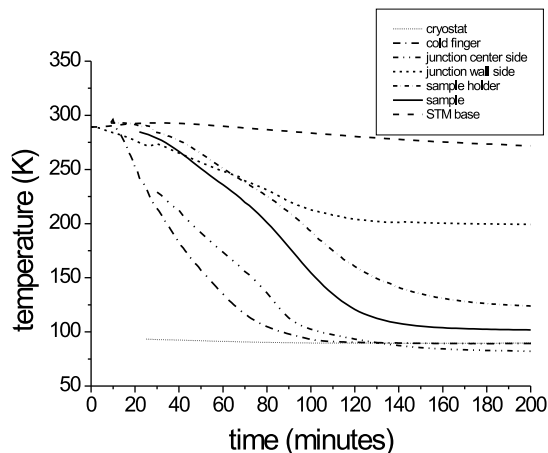


Figure 2.6: Cooling performance at several locations of the cooling path between the cryostat and the sample in the new programmable temperature STM. Plotted are the temperatures versus time. The cryostat was cooled down using liquid helium. The temperature was measured by thermocouples, using the wall of the vacuum system as reference. This causes large errors in the absolute values of the lower temperatures. The cooling path splits in two identical paths after the cold finger. The cooling path closest to the center of the vacuum chamber reaches a lower final temperature in a shorter time than the path closest to the wall of the vacuum chamber. This indicates a heat leak in the latter cooling path.

In the Artist STM the temperature of the sample is measured with respect to the STM base. The STM base is not thermally anchored to the setup. The temperature of the block is measured with respect to temperature of the wall of the setup. The wall of the setup is assumed to be at room temperature. However, variations of order of magnitude 1 K in this reference temperature, cause calibration errors of tens of K at low temperature. In the new programmable temperature STM this problem is solved by placing the reference point of the thermocouple junction for the sample and the STM base outside and away from the setup. This way we can choose any well defined reference temperature, thereby reducing the measurement error in the temperature of the sample.

2.5 Design for a UHV-pre-vacuum system for the improved programmable temperature STM vacuum system

The new programmable temperature STM setup as described in section 2.4 was not complete yet. In the final geometry this new main chamber will be connected with the old main chamber, with a transfer chamber between these two main chambers. The combined setup will eventually look as indicated in figure 2.7. STM measurements will take place in the two main UHV chambers. The analysis equipment that is now fitted to the individual setups, as described in section 2.3 and section 2.4, will stay on these two main chambers in the combined setup. Only the load lock will be shared. The load lock will be mounted to the transfer chamber. The transfer chamber is a UHV chamber, located between the two main chambers. The function of this chamber is to enable exchange of sample holders and scanners between the two main chambers and the outside world without the need for venting one of these three chambers. Furthermore, a storage chamber for sample holders and scanners in UHV together with a chamber for preparing samples in "dirty" conditions, for example high flux growth on samples are fitted.

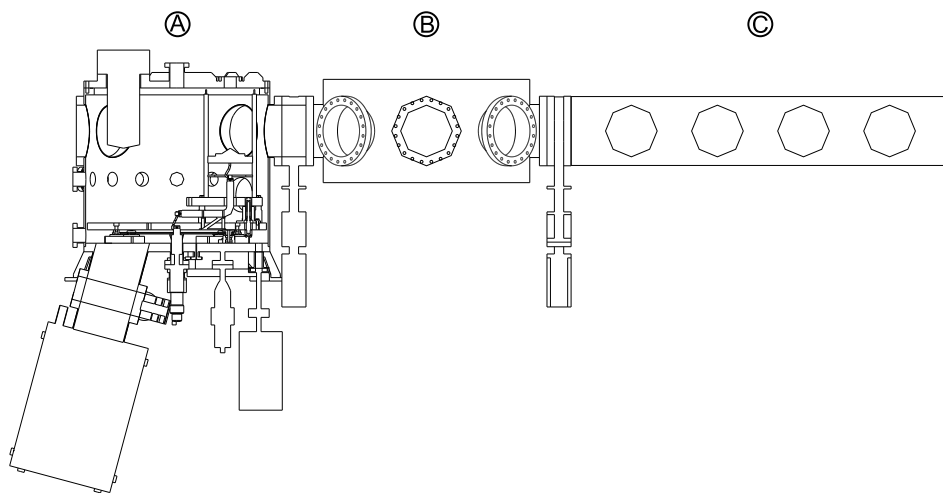


Figure 2.7: Schematic of the final configuration of the combined programmable temperature STMs. A.) The improved programmable temperature STM main chamber. B.) The transfer chamber. Connected to this chamber are a load lock, a storage chamber for scanners and samples and a preparation chamber (all not drawn). C.) The Artist programmable temperature STM main chamber (no details drawn in).

Both main chambers will be pumped by the same type magnetically levitated turbo-molecular drag pump which has already been fitted to the new programmable temperature STM setup. This type of pump is oil-free and has a high compression ratio for all gasses, particularly hydrogen. The capabilities of these turbo-molecular

drag pumps are best used when their exhaust is fitted to another UHV system. This way we can obtain extremely high vacuum in the main chambers in the range of $10^{-11} - 10^{-12}$ mbar without back flow of gasses through the turbo-molecular drag pumps.

The main chamber of the new variable temperature STM is fitted with a differentially pumped ion gun. The differential pumping stage also requires an ultra high vacuum system, that allows for gas flows such that the pressure in the ionization chamber can reach $1 \cdot 10^{-4}$ mbar. The ion erosion treatment of the sample requires pure gases. This demands for regular flushing of the high pressure gas lines that provide these gases. It also requires the background pressure of the differential pumping stage to be low with respect to the $1 \cdot 10^{-4}$ mbar in the ionization chamber.

The construction of the combined setup allows for running two independent experiments at the same time. The idea is to make one UHV pre-vacuum system for all three UHV chambers that meets all the requirements for using the combined setups independent of each other.

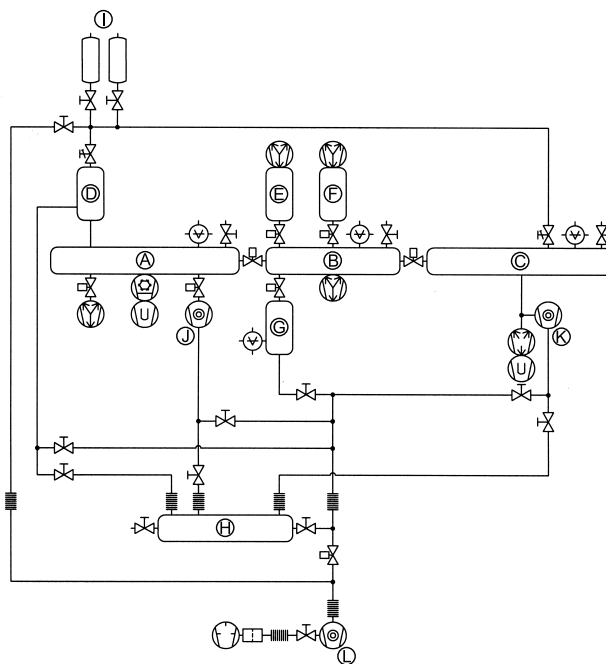


Figure 2.8: Schematic view of the complete vacuum system, including pre-vacuum system. A.) main chamber improved programmable temperature STM, B.) transfer chamber, C.) main chamber Artist STM, D.) ionization chamber differentially pumped ion gun, E.) storage chamber, F.) preparation chamber, G.) load lock, H.) pre-vacuum buffer vessel, I.) Gas handling system for ion erosion, J.) magnetic turbo-molecular drag pump of the main chamber of the improved programmable temperature STM, K.) magnetic turbo-molecular drag pump of the main chamber of the Artist programmable temperature STM, L.) turbo-molecular pump pre-vacuum system.

The design of the complete vacuum system is shown in figure 2.8. The connection to the high vacuum side of the 60 l/s turbo-molecular pump L is such, that the pump is directly connected to the load lock with a piece of 217 cm long tube with an inner diameter of 6.0 cm. One branch of this tube goes to the 120 l buffer vessel and other branches go directly to the magnetically levitated turbo-molecular drag pumps J and K and to the ionization chamber of the sputter gun D. These tubes have the largest diameter possible (6.0 cm) to reach all parts that require pre-vacuum and are partially flexible to reduce vibrations. The buffer vessel provides pre-vacuum for the whole set-up filling up to 10^{-2} mbar in 48 hours. This enables users to switch off pump L to reduce vibrations during a measurement or to perform a full bake-out of part of the set-up without interfering with the other parts. To minimize its own surface area, reducing its own outgassing, the dimensions of the cylindrical buffer vessel are chosen at a diameter of 67.4 cm and a length of 33.7 cm. The valves in the tubes can be set such that the turbo-molecular pump L can be used for pumping one part of the set-up, while the gas pumped from the other chambers can be stored in the buffer vessel. This way, all three main parts A, B and C can be operated individually without the other parts being affected. To reduce vibrations from the pumps, the turbo-molecular pump L is suspended from a bellows with vibration damping. The turbo-molecular pump L is the only pump connected to the pre-vacuum system. It is pumped by a $5 \text{ m}^3/\text{hour}$ rotary vane pump. The provision for replacing contaminated gas, used for ion erosion, is made by connecting the narrow gas tube (inner diameter 0.6 cm) to the turbo-molecular pump L.

Taking geometrical considerations like tube diameter, length and curvature as well as the outgas rate of the used materials into account, pumping capacities and final pressures can be calculated. The calculation method used here is described in [79]. An experimental value for the outgas rate of $(7 \pm 1) \cdot 10^{-10} \text{ mbar} \cdot \text{m}^3/\text{s}/\text{m}^2$ was determined from a well defined part of the Artist main chamber. Taking the position of the parts, pumped down by the pre-vacuum system as shown in figure 2.8 and the diameter of the tubes as stated above, the pumping capacities and final pressures at several positions on the pre-vacuum system, mentioned in figure 2.8, were calculated. In these calculations, only pump L and its roughing pump are considered to be switched on. The result is shown in table 2.1. Comparison of the experimentally obtained final pressure of $2 \cdot 10^{-8} \text{ mbar}$ for differentially pumping the ionization chamber D of the ion gun in the current geometry (not shown here), with its calculated value of $4 \cdot 10^{-8} \text{ mbar}$ shows that these calculations are reliable.

The final pressure of the magnetically levitated turbo molecular pumps J and K in figure 2.8 is $5 \cdot 10^{-11} \text{ mbar}$. The lowest compression ratio for these pumps is $2.5 \cdot 10^5$ for molecular hydrogen. The UHV pre-vacuum system described above will only be necessary when the base pressure in one of the main chambers A or C is below $5 \cdot 10^{-11} \text{ mbar}$. Below this pressure, the magnetically levitated turbo molecular pumps will effectively not pump any more. The pre-vacuum should then be below $1 \cdot 10^{-5} \text{ mbar}$ to prevent hydrogen back flow through the turbo molecular

pumps J and K. Unfortunately, the obtained final pressure in the improved main chamber is only $2 \cdot 10^{-10}$ mbar. Residual gas analysis shows that hydrogen at most contributes half to this final pressure. One reason for this lack in performance can be the limited number of bake-outs of this new system. As the vacuum vessel is baked out more often, volatile species stored in deeper layers of the walls and components inside are removed, so that in time the overall outgas rate lowers, resulting in a lower final pressure. Other reasons might be the presence of compounds in the UHV system with a relatively large outgas rate and the presence of virtual leaks.

Table 2.1: Calculated values for the final pressure and pumping capacity at various locations in figure 2.8 (always on the low vacuum side) after bake-out. Only the turbo-molecular pump L is assumed to be switched on.

location	final pressure (mbar)	pumping capacity (l/s)
D	$5.1 \cdot 10^{-8}$ (a) / $2.1 \cdot 10^{-7}$ (b)	9 (a) / 7 (b)
E	$2.0 \cdot 10^{-7}$	10
F	$2.0 \cdot 10^{-7}$	10
G	$4.1 \cdot 10^{-8}$	10
H	$4.0 \cdot 10^{-8}$	28
I	$5.8 \cdot 10^{-6}$	0.008
J	$4.1 \cdot 10^{-8}$ (a) / $1.6 \cdot 10^{-7}$ (b)	10 (a) / 9 (b)
K	$4.1 \cdot 10^{-8}$ (a) / $1.7 \cdot 10^{-7}$ (b)	10 (a) / 9 (b)

(a) pumping direct via turbo molecular pump L

(b) pumping via buffer vessel H

CHAPTER 3

Vacancy creation/annihilation: Experiment and analysis

This chapter describes the experiments and first analysis on the vacancy assisted diffusion of indium atoms in vacancy islands on the Cu(100) surface. It is shown that the chosen geometry with vacancy islands enables us to determine the difference between the activation energy for the formation and the annihilation of surface vacancies. A first step in the determination of these activation energies, from the presented measurements is made in this chapter. The analysis is concluded with the theory developed in chapter 4.

3.1 Introduction

Over the years, the investigation of surface self-diffusion with STM has mainly been focused on the properties of structures, on top, of a surface, such as adatoms [80, 81], steps [7, 82, 83, 84], adsorbates [5] or larger structures in the top layer like vacancy islands [85, 86]. However, surface diffusion may also proceed very efficiently within the outermost atomic layer, i.e. completely without the need for atoms or other structures on top.

The geometrical counterpart of adatoms are surface vacancies, where in stead of added atoms on top, the surface has a deficit of atoms in the top layer, resulting in empty lattice sites. Previous studies on the Cu(100) surface have indicated, that at room temperature, typically only one in 10^9 [39, 41] lattice sites are vacancies, but they move through the surface at hopping rates in the order of 10^8 Hz [39]. This means that, on average, all atoms in this surface are displaced by vacancies every 10 seconds! In this way, surface vacancies cause substantial, lateral transport within the surface [38, 39, 40, 41, 42, 43, 58, 87, 88, 89]. This mechanism has been nicknamed "slide-puzzle" diffusion. Unfortunately, the low vacancy concentrations and the high hopping rates make it very difficult to determine experimentally where surface vacancies originate and where they annihilate. Previous work on Cu(100) by Van Gastel et al. and Flores et al., has provided a first indication that steps on the surface play an important role in the creation and annihilation of surface vacancies [41, 56, 57]. These authors found indications for a step edge barrier for the motion of surface vacancies, similar to an Ehrlich-Schwoebel barrier [17, 18] for adatoms. This notion leads to new, more detailed questions, such as: Is there a difference between the creation of vacancies at the upper and at the lower side of steps? Is there a special role for kinks? Etcetera.

In this chapter we focus on the issue of the upward and downward steps. We create geometries on a Cu(100) surface which are bounded by only one 'flavor' of steps. By monitoring the "slide-puzzle" diffusion of vacancies inside and outside these geometries, we can measure the activation energy difference for the creation and annihilation of surface vacancies between the upper and lower side of a step on Cu(100).

3.2 Experimental procedures

The Cu sample ($4.8 \times 4.8 \times 2.0$ mm³) was cut by spark erosion from a 5N purity single crystal. The crystal was chemically etched and polished parallel to the (100)-plane with an accuracy of 0.1° [90]. After introducing the sample in the UHV chamber with a background pressure of $1 \cdot 10^{-10}$ mbar, the sample was cleaned by several cycles of ion bombardment with 600 eV Ar⁺ and annealing at 690 K [91]. A typical STM image of the Cu(100) surface after cleaning is shown in figure 3.1.

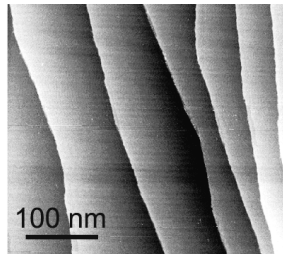


Figure 3.1: STM image of the Cu(100) surface after several cycles of ion bombardment for 10 min with 600 eV Ar^+ , $I_{\text{sputter}} = 4 \mu\text{A}$, $p_{\text{Ar}} = 5 \cdot 10^{-5} \text{ mbar}$ and annealing for 6 min at 690 K in UHV. The image was processed by adding the image containing the error (dZ) signal to the standard height image as described in [78]. ($V_t = 1.5 \text{ V}$, $I_t = 0.1 \text{ nA}$)

After this cleaning, geometries were created on/in the surface with only upward or only downward steps. The procedure for this was as follows. The first step was to introduce a high density of upward and downward steps on the surface. This was achieved by bombarding the surface with Ar^+ ions at room temperature, using the same ion gun parameters as in the cleaning procedure. A typical result is shown in figure 3.2a. This STM image shows that after this treatment the step density is indeed very high. Apart from long steps that cross the entire image, there are also structures like adatom islands and vacancy islands on the surface. These are the geometries that only have one flavor of steps. Adatom islands only have upward steps, while vacancy islands only have downward steps. The steps in these structures are too close to each other to investigate vacancy diffusion inside and outside vacancy or adatom islands. Therefore, the surface was mildly annealed to 333 K, while monitoring the surface with the variable temperature STM [71]. We continued this annealing until a comfortable density of isolated vacancy islands of about $10 \times 10 \text{ nm}^2$ was observed. A typical STM image of the surface after this treatment is shown in figure 3.2b.

The high rate at which the surface vacancies hop through the surface at room temperature, makes it impossible to follow them directly with STM. On the other hand, the rate at which surface vacancies are created at lower temperatures (e.g. 100 K; see chapter 5), is so low that we would have to wait insensibly long for a vacancy to move through our field of view. That is why, like Van Gastel et al., we have been forced to use tracer particles, in particular In atoms, to visualize the effect of vacancies moving through the surface. For this purpose, the final preparation step was to deposit 0.003 ML of In on the surface. The In was deposited by exposing the surface for 20 sec to a flux from a Knudsen cell, filled with In and heated to 1015 K. Even at the low sample temperature (room temperature), the In atoms were rapidly incorporated in the top layer of the surface. The result after In deposition is shown in figure 3.2c.

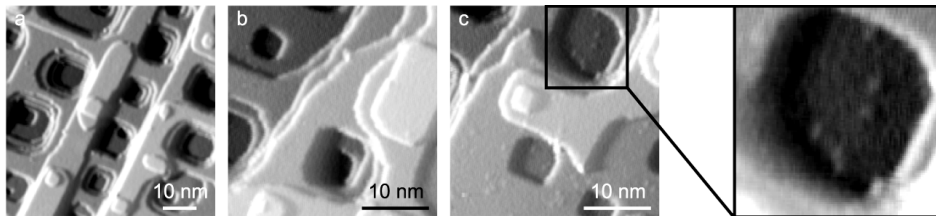


Figure 3.2: STM images of subsequent stages of the preparation of isolated vacancy islands in Cu(100). To increase contrast, the original and the differentiated height maps have been mixed. Vacancy islands are geometries surrounded by upward steps only. (a) Cu(100) surface after ion bombardment at room temperature for 10 min with 600 eV Ar⁺, $I_{\text{sputter}} = 4 \mu\text{A}$, $p = 5 \cdot 10^{-5}$ mbar. (b) Cu(100) surface after mild annealing to 333 K until there were isolated islands. (c) Cu(100) surface after deposition of 0.003 ML In. The In atoms immediately get incorporated in the top layer of the surface. The small protrusions inside the enlarged vacancy island are individual incorporated In atoms. ($V_t = -0.5$ V, $I_t = 0.1$ nA for all images)

3.3 Qualitative observations

Using the STM we selected an area on the surface with an isolated vacancy island of about $10 \times 10 \text{ nm}^2$. The field of view we used was slightly larger than this vacancy island, so that we also had a good view of the terrace directly outside the vacancy island. Inside the vacancy island, as well as on the terrace surrounding it, In atoms were incorporated in the top-layer of the surface. The In atoms move through the surface by changing places with a surface vacancy ("slide puzzle" diffusion). We have investigated the mobility of the In atoms by making series of STM images of the selected area. From these series of images, we have formed movies that show the motion of the embedded In atoms in the surface. Figure 3.3 shows typical images taken out of such a movie. The start of this fragment is shown in fig. 3.3a. In the time interval of 131 seconds between fig. 3.3a and fig. 3.3b, there was no motion of In atoms inside the vacancy island. Figure 3.3b-e are consecutive images that were made with a time intervals of 26.2 seconds. Between fig. 3.3b and fig 3.3c, we see that all the In atoms inside the vacancy island have jumped over large distances. Between fig. 3.3c and fig. 3.3d, only one In atom inside the vacancy island has moved. In fig 3.3e we see that none of the In atoms inside the vacancy island has moved. The In atoms inside the vacancy island have also remained motionless between figure 3.3e and figure 3.3f, which was recorded 210 seconds later. Figures 3.3b-e also show that outside the vacancy island In atoms have been moving over short distances between all subsequent images. This behavior is observed throughout this movie and others, recorded under similar circumstances. Inside the vacancy island, all the In atoms are jumping at the same time over long distances in random uncorrelated directions. The typical waiting time between these synchronized jumps is about one order of magnitude longer than the average waiting time for In atom

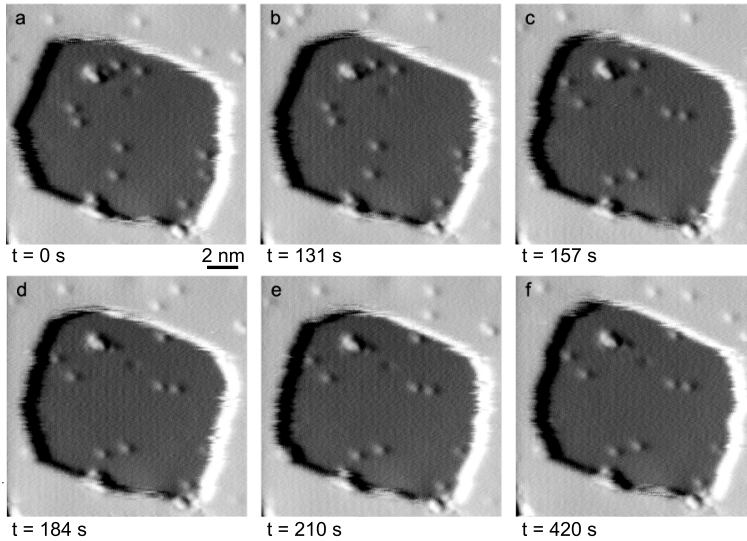


Figure 3.3: Typical images taken from an STM movie at room temperature. To increase contrast, the original and the differentiated height maps have been mixed. The dark area in the images is a vacancy island. Small protrusions inside and outside the vacancy island, are In atoms embedded in the top-layer of Cu(100). a.) Start of the movie fragment. b.-e.) STM images taken directly after each other at time intervals of 26.2 s. Between $t = 131$ s and $t = 157$ s, all In atoms inside the vacancy island have moved substantially. Between $t = 157$ s and $t = 184$ s a single In atom in the vacancy island has moved. Before $t = 131$ s and after $t = 184$ s no motion of In atoms is observed inside the vacancy island. Outside the vacancy island, In atoms have moved over short distances between every pair of images. f.) Even at $t = 420$ s, the In atoms inside the vacancy island have not been displaced again yet. This behavior is observed throughout the movie: long jumps and long waiting times for In atoms inside the vacancy island, short jumps and short waiting times for In atoms outside the vacancy island. ($V_t = -0.6$ V, $I_t = 0.1$ nA for all images)

jumps outside the vacancy island. Outside the vacancy islands, the In atoms do not necessarily move all at the same time, and the typical jump length of these In atoms is about a factor two smaller. Although the mechanism and energy barriers for the vacancy assisted diffusion of the In atoms inside and outside a vacancy island are expected to be the same, we observe this surprising difference in the behavior of In atoms, which demands an explanation.

For the vacancy assisted diffusion of In atoms to take place, a surface vacancy has to be created in the first place. Outside the vacancy island, a possible scenario for the creation of a vacancy island, is that two atoms at the step edge diffuse simultaneously into a kink site, thus forming a vacancy and displacing the kink. Calculations with the embedded atom model (EAM), similar to the calculations performed in [42], show that this simultaneous process is more likely than the two atoms diffusing independently. This one-step process is shown in the upper left panel of figure 3.4.

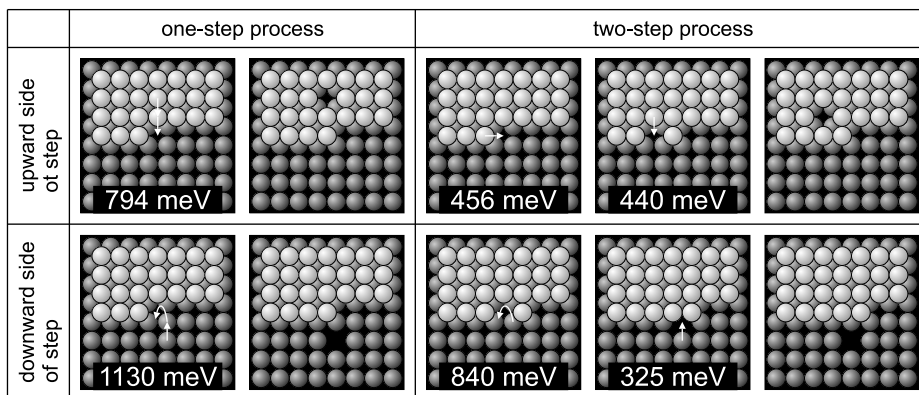


Figure 3.4: The upper panels show cartoons of two possible scenarios for the creation of a surface vacancy at the upper side of a step by rearranging Cu atoms at the step. In the one-step process, two atoms move simultaneously into the kink. In the two-step process, a step vacancy is formed into which an atom from the terrace can move. The lower panels show two possible scenarios for the creation of a vacancy at the lower side of a step. In the one-step process, the vacancy is created by the extrusion of an atom from the lower terrace at the kink site. This atom attaches to the step edge. The void left behind by this atom is simultaneously filled with another atom from the lower terrace. The two-step process is an exchange process, where an atom from the lower terrace is moving into a step vacancy while a neighboring atom moves underneath the step. The values for the activation energies are obtained from Embedded Atom Model (EAM) calculations [13].

A possible two-step process at the upper side is where a vacancy is created from a step vacancy. This process is shown in the upper right panel of figure 3.4. Inside a vacancy island, the creation of a vacancy by the rearrangement of atoms at the step is not possible, because there are only upward steps. A copper atom at the kink site can directly move into the kink, while simultaneously another atom from the lower terrace fills the gap left behind. This one-step process is shown in the lower left panel of figure 3.4. Again, the EAM calculations predict this simultaneous process to be more efficient than the two independent diffusion steps. A possible two-step process can be an exchange process where an atom from the lower terrace is built into a step vacancy, while a neighboring atom moves underneath the step. This process is shown in the lower right panel of figure 3.4. In terms of activation energies, the processes at the lower side of a step seem to be more expensive compared to those involved in the creation of a vacancy at the upper side of a step. It also seems that the most efficient scenarios are two-step mechanisms in which a step vacancy is created first, followed by the diffusion of this step vacancy into either the upper or the lower terrace, where it continues as a regular surface vacancy.

The waiting time between the jumps of embedded In atoms reflects the frequency at which surface vacancies are created. The more unfavorable it is for a vacancy to be created, i.e. the higher the activation energy for the creation process,

the longer the average waiting time. The difference between the observed typical waiting times inside and outside the vacancy island indicates an activation energy difference for the creation of a surface vacancy inside and outside a vacancy island. Because of our choice for a geometry that only has upward steps we may reformulate this in terms of the activation energy difference for the creation of a surface vacancy between the down side and the up side of a step. The observed difference in average waiting time points in the naively expected direction.

3.4 Quantitative analysis

The vacancy-mediated diffusion of In atoms, provides us with a tool to quantitatively analyze the behavior of surface vacancies with STM [41]. The In atoms act as tracer particles for surface vacancies passing by. We have analyzed the distribution of jump lengths and waiting times for jumps of these tracer particles inside and outside a vacancy island. With this, we have quantified the difference in the activation energy for the creation and the annihilation of surface vacancies at the upper and lower sides of a step. The software sequences, used for the analysis are described in the Appendix A (sections A1 and A2).

3.4.1 Jump length distributions inside and outside a vacancy island

A distribution of jump lengths was generated by counting how often a particular jump length occurred. As pointed out in section 3.3, there is a difference in behavior of In atoms inside and outside a vacancy island. Therefore two jump length distributions were produced, one for inside a vacancy island and one for outside. For comparison, both jump length distributions are shown in figure 3.5. The data of the jump length distribution inside the vacancy island is plotted in grey bars, the data from the outside of the vacancy island in white bars. Unlike ordinary diffusion, vacancy-mediated diffusion is a process with an end. Diffusion stops when the surface vacancy is annihilated. This property of vacancy mediated diffusion causes the jump distance distribution to deviate from a Gaussian function. Instead, it can be shown that the distribution can be approximated rather well by a modified 0^{th} order Bessel function [42]:

$$p(r) = \frac{1}{2\pi} R_{eff} K_0 \left(r \sqrt{R_{eff}} \right) \quad (3.1)$$

Where

$$R_{eff} = \frac{4\hat{p}_{rec}}{\hat{p}_{perp} + \hat{p}_{opp}} \quad (3.2)$$

In equation 3.2, \hat{p}_{rec} is the probability that the surface vacancy recombines starting from a position next to the tracer particle. \hat{p}_{perp} and \hat{p}_{opp} are the probabilities that the vacancy returns to the tracer particle from respectively one of the two perpendicular

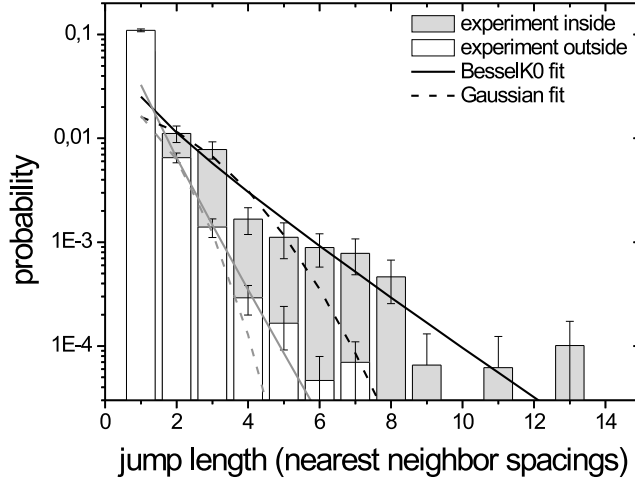


Figure 3.5: *Jump distributions inside (grey bars) and outside (white bars) a vacancy island. Both distributions are fitted by a 0^{th} order modified Bessel function (solid line) and a Gaussian distribution (dashed line). The Bessel function fits the data, which indicates vacancy-mediated diffusion. The typical jump distance inside the vacancy island is significantly larger than that outside the vacancy island.*

sides or the opposite side, with respect to the side where it started its random walk after its previous encounter with that tracer particle¹.

In figure 3.5, the solid lines are modified 0^{th} order Bessel function fits to the experimental data. The dashed lines show a Gaussian fit to the same data. The black lines are fits to the data from inside the vacancy island, the grey lines are fits to the data from the outside of the vacancy island. The fits show that in both cases the modified 0^{th} order Bessel function fits the data better than the Gaussian curve. The best fits are obtained for $R_{eff}^{inside} = 0.25$ and $R_{eff}^{outside} = 1.7$.

Now we focus on the difference between the jump lengths inside and outside the vacancy island. From figure 3.5 it is clear that inside the vacancy island the typical jump lengths of the In atoms are significantly larger than outside the vacancy island. Equations 3.1 and 3.2 show that the width of the distribution depends on two return probabilities and the recombination probability of a surface vacancy. Since we can safely assume for the ratio between the return probabilities that $\hat{p}_{perp} \gg \hat{p}_{opp}$, both on the upper and on the lower side of the step, similar to the situation far away

¹For the case of indium as a tracer particle the exchange barrier with the vacancy is considerably lower than all other barriers. The modified probability \hat{p} compensates for the large number of ineffective back-and-forth exchanges of the vacancy and the tracer atom (see also equation 4.22) [42].

from a step, where $\hat{p}_{perp} = 0.46$ and $\hat{p}_{opp} = 0.018$ [42], and since, by definition $2\hat{p}_{perp} + \hat{p}_{opp} + \hat{p}_{rec} = 1$ [42], the recombination probability on the inside of the vacancy island is obtained from the above value of R_{eff}^{inside} to be 0.031, while on the outside of the vacancy island, the recombination probability is 0.18. From this we conclude that inside the vacancy island, the surface vacancy exists for a much longer period of time than outside the vacancy island. For comparison, the recombination probability that was measured on Cu(100), far away from steps, namely the center of a $100 \times 100 \text{ nm}^2$ terrace amounted to 0.046 [39].

It can be shown that to a very good approximation, the recombination probability is inversely proportional to the logarithm of the distance to the nearest source-and-sink combination for surface vacancies [41, 42]. The value for the return probability outside the vacancy island matches the expected value for the average distance of 2.5 nm from the step at which we measured. Inside the vacancy island, the situation is completely different. The recombination probability we find there corresponds to a distance to the nearest source-and-sink combination of 0.05 nm . This macroscopic distance stands in dramatic contrast with the average radius of the vacancy island of 6 nm ! This shows that in an area that is fully enclosed by only an upward step, the jump distance distribution is much wider than expected and thus surface vacancies "live" much longer than when the area would be surrounded by only downward steps. The upward step acts as a mirror for surface vacancies. This effect can be expressed in an excess activation energy for the annihilation of surface vacancies at an upward step. This is however not straightforward, because the size of the vacancy island is limited and the present indium atoms locally distort the diffusion behavior of the surface vacancies. In chapter 4 we use Monte Carlo simulations to fit the jump length distribution and thereby determine the excess activation energy for the annihilation of a surface vacancy at an upward step to be:

$$E_{act}^{ann-inside} = 114 \pm 30 \text{ meV}$$

3.4.2 Waiting time distributions inside and outside a vacancy island

As has been pointed out in section 3.3, the typical waiting time between the jumps of the In atoms inside the vacancy island is about one order of magnitude longer than outside the vacancy island. This difference in waiting time can be quantified with a waiting time distribution. These distributions were generated by following individual In atoms jumping through the surface and counting how often a particular waiting time between jumps occurred. The waiting time distributions for both inside and outside a vacancy island are shown in figure 3.6. Both waiting time distributions can be described well by exponential decay, from which we can determine the typical jump frequency ν . Inside the vacancy island $\nu_{inside} = (2.6 \pm 0.5) \cdot 10^{-2} \text{ Hz}$, outside the vacancy island $\nu_{outside} = 1.0 \pm 0.1 \text{ Hz}$. The processes that determine the typical jump frequency are the creation of a surface vacancy, the diffusion of

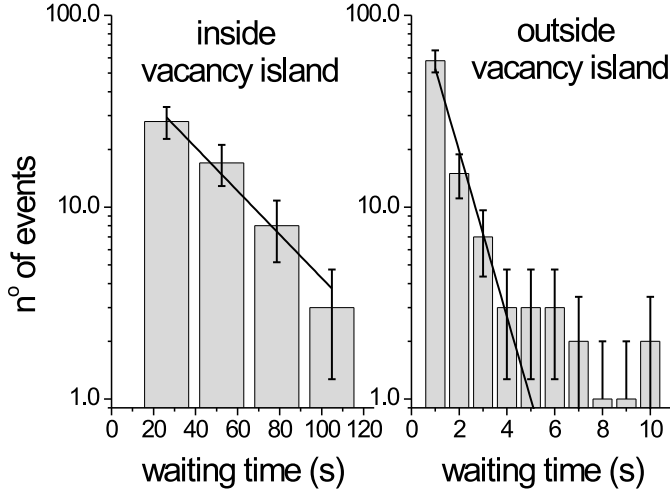


Figure 3.6: *Waiting time distributions for In atom jumps inside (left) and outside (right) a vacancy island. Plotted are the number of times an In atom jumps after a certain waiting time versus the waiting time. In both cases, the waiting time distribution is consistent with an exponential. The typical waiting time (time constant of the exponential fit) inside the vacancy island is 38 s. Outside the vacancy island the typical waiting time is 1.0 s*

the vacancy through the surface and, possibly an extra energy barrier for a surface vacancy to exchange with an In atom embedded in the surface. Naively, one might expect that the behavior of the jump frequency of indium atoms as a function of temperature would be given by:

$$\nu = \nu_0 e^{-\frac{E_F + E_D + \Delta}{k_B T}} \quad (3.3)$$

where E_F is the activation energy for the formation of a surface vacancy, E_D is the activation energy for the diffusion of a surface vacancy and Δ describes the difference between the vacancy-indium exchange barrier and the vacancy diffusion barrier in a clean Cu(100) terrace. In case indium is the tracer particle, Δ is negative [36, 41]. The condition $\Delta/k_B T \ll -1$ is also fulfilled, so that, as argued in [36, 41], the effect of Δ on the jump frequency can safely be ruled out and the jump frequency of indium atoms should exhibit Arrhenius behavior with an effective activation energy of $E_F + E_D$. We expect that the activation barriers E_D for the diffusion of surface vacancies inside and outside the vacancy island are the same. Both inside and outside a vacancy island, they describe diffusion of a surface vacancy through a terrace. The ratio between ν_{inside} and $\nu_{outside}$ would then directly indicate how difficult it is to form a vacancy at the lower side of a step, with respect

to the formation of a surface vacancy at the upper side of a step. This is expressed in the activation energy difference between the creation of a surface vacancy at the lower and at the upper side of a step.

$$E_F^{inside} - E_F^{outside} = 90 \pm 4meV$$

However, there is a significant geometric effect that influences the jump frequency of the indium atoms inside and outside the vacancy island. Inside the vacancy island, the lifetime of the vacancies is long enough to allow it to visit all sites inside the vacancy island. This is reflected by the observation in section 3.3 that the indium atoms inside the vacancy island collectively jump between two consecutive images. This effect is commonly observed. This means that every indium atom inside the vacancy island, registers all surface vacancies that are formed at the inner perimeter of the vacancy island. The average waiting time between long jumps of indium atoms inside the vacancy island, is only determined by the rate at which surface vacancies are created. The correct frequency for long jumps for indium atoms inside a vacancy island ν_{LJ}^{inside} is given by

$$\nu_{LJ}^{inside} = \nu_0 L e^{-\frac{E_F^{inside}}{k_B T}} \quad (3.4)$$

Where ν_0 is the attempt frequency for the creation process and L is the number of positions along the inner perimeter of the vacancy island where a creation event can take place.

Outside the vacancy island, the jump frequency for long jumps from [36, 41] is more appropriate:

$$\nu_{LJ}^{outside} = \nu_0 C' e^{-\frac{E_F^{outside}}{k_B T}} \quad (3.5)$$

Where $C' = 3(1 - C)$ is a geometrical factor strongly influenced by the presence of the downward step. Assuming that there is no extra annihilation barrier for vacancies coming from the upper terrace, this activation energy is the sum of the formation energy for a surface vacancy E_{vac} and the activation barrier for the diffusion over a clean Cu(100) surface E_D .

We determined the ratio between the jump frequencies of long jumps inside and outside a vacancy island for room temperature only. The argument stated above shows that this ratio is not solely determined by the difference in the activation energy for the formation of surface vacancies inside and outside a vacancy island. This ratio also depends on the geometric pre-factors L inside the vacancy island and C' outside the vacancy island. The systematic error arising from the pre-factors, will be determined with a Monte Carlo simulation in section 4.7

The correct value for the activation energy difference between the creation of a surface vacancy at the lower and at the upper side of a step is:

$$E_F^{inside} - E_F^{outside} = E_F^{inside} - E_{vac} - E_D = 136 \pm 12meV$$

3.4.3 Diffusion constants inside and outside a vacancy island

Both inside and outside the vacancy island, the In atoms move through the surface following the "slide-puzzle" diffusion mechanism. Inside the vacancy island we see that the In atoms on average jump over relatively large distances with long time intervals between the jumps. Outside the vacancy island the In atoms on average jump over small distances with short time intervals. One should expect that in both cases the diffusion coefficient has the same value.

$$D = \frac{\langle r^2 \rangle}{4t} = D_0 e^{-\frac{E_D}{k_B T}} \quad (3.6)$$

We determined the mean square displacement $\langle r^2 \rangle$ of the In atoms separately inside and outside the vacancy island. For both cases, we determined the average waiting time t which is the inverse of the typical jump frequencies ν from figure 3.6. With these values we can determine the diffusion coefficients inside and outside the vacancy island, D^{inside} and $D^{outside}$. From equation 3.6 we see that the ratio between the two diffusion coefficients gives us the difference in activation energies for the diffusion of the vacancy inside and outside the vacancy island.

$$\frac{D^{inside}}{D^{outside}} = e^{-\frac{E_{D^{inside}} - E_{D^{outside}}}{k_B T}} \quad (3.7)$$

To our surprise we found a significant difference in the diffusion coefficients inside and outside the vacancy island. Expressed in the activation energy difference, it was:

$$E_D^{inside} - E_D^{outside} = 33 \pm 9 \text{ meV}$$

We suggest that this difference is due to surface stress. Experiments and calculations by Brune et al. and Wang et al. for Ag adatoms on Ag(111) under different amounts of strain show that compressive strain decreases the activation energy for the diffusion and tensile strain increases this activation energy [92, 93]. This effect is caused by the variation of the activation energy with the lattice constant [94]. Cu(100) is a surface under tensile stress. Steps are locations on the surface where the surface can partly relax this stress. Therefore, the interatomic distances in the vicinity of a step are more compressed than those far away from a step and thus the activation energy for the diffusion of an adatom would be lower in the vicinity of a step. We expect that this lowering of the activation energy for the diffusion also holds for surface vacancies. The strength of the effect on the activation energy should, of course, depend on the strain, but for Ag on Ag(111) Brune et al. found a decrease of 36 meV for a compressive strain of 5%. This variation is in the same order of magnitude as the change in activation energy that we have found here for surface vacancies on Cu(100). Calculations by Ratsch et al. show that additional strain in a surface has no significant effect on the diffusion attempt frequency [95].

The difference in diffusion coefficients that we have found can thus probably be attributed to the local lowering of the diffusion activation energy by relaxation of the tensile stress at steps.

3.5 Discussion and conclusion

The experiments reported in this chapter and the analysis, partly based on the Monte Carlo calculations, described in the next chapter, enable us to construct a detailed picture of the 'life' of a surface vacancy. Figure 3.7 shows a compilation of the information derived here, completed with numbers obtained from references [41] and [58] combined in the form of an energy landscape for surface vacancies in the Cu(100) surface. We conclude that surface vacancies on Cu(100) are created predominantly at the upper side of steps, while the lower sides act as efficient mirrors for existing surface vacancies. Although this picture is seemingly complete, there are still several interesting questions left.

The first issue concerns the activation energy for the diffusion of surface vacancies. The experiments described in this section show that there is a difference in diffusion energies that we ascribe to stress relaxation at the step, but these experiments do not allow us to determine the individual activation energies. This requires a different experimental approach, which is followed in chapter 5.

The second issue is the possible existence of finite-size effects. A single vacancy cannot move an embedded indium atom beyond a step. When the indium atom reaches the step it will attach to a kink, after which it has the possibility to diffuse into either the upper or the lower terrace. This confinement limits the sizes of their jumps to the distances between the indium atoms and the surrounding steps, e.g. the edges of the vacancy island. However, the experimentally obtained jump distance distributions already stop at jump lengths of 14 nearest neighbor distances. As the dimensions of our vacancy island are more than three times as large, we expect that this finite-size effect has been rather modest. Nevertheless, near the upper and the lower side of a step, this finite-size effect may reduce the width and further affect the shape of the jump length distribution of In atoms. Throughout the series of STM images we have observed that the number of In atoms inside the vacancy island fluctuated randomly, individual In atoms crossing the step from time to time, both in the upward and in the downward direction.

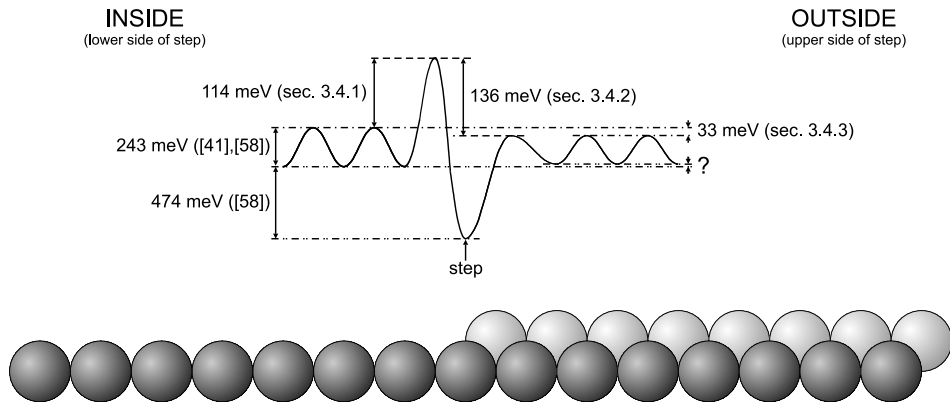


Figure 3.7: Energy landscape for the creation and diffusion of a surface vacancy in the Cu(100) surface. This diagram is completely equivalent to the schematic energy landscape, sketched in figure 1.2 for the creation and diffusion of adatoms. The references between brackets next to the energy value, show from which section or publication the activation energy is obtained. Inside the vacancy island the activation energy for the creation of surface vacancies is 136 meV higher than outside the vacancy island. Accordingly there is also an activation energy for the annihilation of surface vacancies that approach a step from the lower side. This causes the mirror effect for surface vacancies at upward steps. Outside the vacancy island, the activation energy for the annihilation of surface vacancies is as high as the diffusion barrier, although an annihilation barrier lower than the diffusion barrier cannot be ruled out. The activation energy for the diffusion of vacancies is 33 meV lower at the upper side of a step. This effect is attributed to stress relaxation at the step. The formation energy of surface vacancies was taken from calculations with the Vienna ab initio simulation package (VASP) reported in [58]. The diffusion barrier for the vacancy was calculated from the experimental value from [41] for the sum of the activation energy for the diffusion of surface vacancies in Cu(100) and the formation energy of a surface vacancy, from which the formation energy of [58] was subtracted.

CHAPTER 4

Vacancy creation and annihilation: Theory

This chapter describes the theory behind the vacancy-assisted diffusion of tracer atoms inside vacancy or adatom islands on a flat crystal surface. Characteristic distribution functions for this type of diffusion are computed with the use of both exact numerical calculations and Monte Carlo simulations. By fitting the results of these calculations to the experimental results of Chapter 3, for the diffusion of indium tracer atoms in the Cu(100) surface, we are able to determine the activation energy for the annihilation of surface vacancies inside and outside a vacancy island on this surface.

4.1 Introduction

Although the investigation of moving structures on a surface with atomically resolving, state-of-the-art techniques, such as STM and FIM, may seem straightforward, there are many cases where the limits of these techniques require one to measure on smartly chosen systems in order to determine the nature of a particular diffusion process.

The diffusion of surface vacancies is such a process. The density of vacancies is very low; typically only one in 10^9 atoms is missing in a Cu(100) surface at room temperature [39, 41]. The jump rate of these surface vacancies at room temperature is in the order of 0.1 GHz [39]. Because of its resolution, STM is the measurement technique of choice to investigate the diffusion behavior of surface vacancies. However, STM is an inherently slow measuring technique and although the speed limits are pushed further and further [69, 78], the only way to match the scan rate of such an instrument to the diffusion rate of the vacancies is to measure at low temperatures. Unfortunately, this would also reduce the concentration of surface vacancies, such that only one atom would be missing in a surface the size of a small city. This makes it clear that, unless single surface vacancies are artificially created at low temperatures (Chapter 5), STM measurements on vacancies have to take place around room temperature.

The method used to measure the behavior of surface vacancies is to visualize their effect on the atoms in the surface via tracer particles [38, 58]. In the experiments described in Chapter 3, indium atoms embedded in the surface, were used as tracer particles. This method has been applied successfully, also in previous studies [38, 39, 40, 41, 43]. The behavior of these tracer particles differs from traditional diffusion, because it indirectly reflects the diffusion of surface vacancies. The theory behind assisted diffusion has already been developed [87, 96, 97, 98, 99].

Other factors, specific for the system used in this thesis should also be taken into account. The area where the vacancy diffusion takes place is limited by the size of the terraces on the Cu(100) surface. The lifetime of the surface vacancy is limited because the boundaries of a terrace act as traps for surface vacancies. Finally the jump rate of surface vacancies is locally enhanced by the presence of the tracer particle. A theoretical model that specifically describes the vacancy-mediated diffusion of indium atoms in Cu(100) can be found in [42]. Somfai et al. have developed both a continuum model and a numerical model for this system. The continuum model allows for an analytic solution of the diffusion equation and shows that the jump length distribution does not follow a Gaussian curve, like in classical diffusion, but a modified 0^{th} order Bessel function. The width of the distribution is determined by the probability that the vacancy is annihilated rather than to return to the tracer particle. The annihilation of a surface vacancy is also referred to as the recombination of a surface vacancy. The further away a vacancy and a tracer particle are from an ideal sink when they encounter each other, the lower the probability is

that the vacancy will be annihilated before their next encounter, and the more often it is expected to return to a tracer particle and displace it. This results in a wider jump length distribution for the tracer particle.

The distribution of the waiting times between subsequent jumps of the indium atoms follows an exponential curve, as is explained in [41]. This form implies that the (long) jumps are uncorrelated with each other, which means that each one must be caused by a different, independently created vacancy. In the case of the vacancy-mediated diffusion of indium atoms embedded in Cu(100), the activation energy determined from the waiting time distribution is the sum of the formation energy of surface vacancies and the activation energy for their diffusion. As the interaction of the indium tracer atom and the vacancy in Cu(100) is attractive, the waiting time distribution does not depend on the interaction energy between the tracer and the vacancy [41].

In section 3.3 it was shown that there is a significant difference in the average jump length of embedded indium atoms inside and outside a vacancy island in Cu(100). The diffusion mechanism and the tracer particles are the same inside and outside the vacancy island. This surprising difference in behavior of the embedded indium atoms indicates that there is a lower recombination probability for the vacancies on the inside of the vacancy island. Generalizing, this means that the recombination probability is lower for vacancies that approach the step from the lower side.

This chapter extends the description of the vacancy mediated diffusion of indium atoms in Cu(100) of [42] by including one extra, important aspect. Here the focus is on the vacancy mediated diffusion of In atoms in islands on Cu(100). In section 4.2, the dependence of the lifetime of a surface vacancy on the perimeter and area of an island is explained. In section 4.3 and section 4.4 exact numerical calculations show the spatial distribution of vacancy visitation probabilities and occupation times inside an island. We investigate how these depend on the location where the vacancy is created inside the island and the recombination probability at the border of the island. Section 4.5 describes the details of the Monte Carlo simulation, used to simulate the location dependence, the annihilation probability dependence and the indium atom distribution dependence of the vacancy-mediated indium atom diffusion inside a vacancy island. In section 4.6 Monte Carlo simulation results are fitted to the experimental jump length distributions inside and outside a vacancy island. In this chapter, the lower recombination probability of a surface vacancy is expressed in an extra activation barrier for the annihilation of surface vacancies at the upward side of a step. In section 4.6, the value for this energy barrier is determined. In section 3.4.2 it was argued that the measured jump frequencies for indium atoms in the upper terrace require correction for undercounting, since a significant fraction of the vacancies would be annihilated before reaching the indium atoms, embedded in the measurement window. In section 4.7 the Monte Carlo simulation is used to determine the proper correction factor. In section 4.8 the results from

Chapter 4 are summarized.

4.2 Vacancy lifetime dependence on the border length of a vacancy island

The island is assumed to be rectangular, with a size of x_I by y_I lattice sites. The creation of vacancies occurs exclusively along the border. The sites at the corners of the island have a doubled probability to be the starting site, since these positions have two neighboring steps. For a vacancy located at one of the border sites the rate for recombination, i.e. for a ‘jump’ into the step, is λ times the rate for a diffusion jump in any of the remaining terrace directions.

The time it takes for a system to go from one state (i.e. a vacancy position \vec{r}) to another, disregarding other possible transitions, follows an exponential distribution:

$$f(t) = \frac{1}{\tau} e^{-\frac{t}{\tau}} \quad (4.1)$$

$$F(t) = 1 - e^{-\frac{t}{\tau}} \quad (4.2)$$

Here $F(t)$ is the cumulative distribution function (the probability that a transition occurs before time t), and the expectation value τ of the transition time is the inverse of the transition rate, which is proportional to the Boltzmann factor:

$$\tau \sim e^{\frac{E}{k_B T}}, \quad (4.3)$$

where E is the activation energy of the process considered. In our case, there are two types of transitions: regular diffusion (with energy barrier E_D) and recombination (E_R). If we define τ_0 to be the waiting time for regular diffusion, then for recombination we get, from equation 4.3:

$$\tau_R = e^{\frac{E_R - E_D}{k_B T}} \tau_0 \quad (4.4)$$

$$\tau_R = \frac{\tau_0}{\lambda} \quad (4.5)$$

$$\lambda = e^{-\frac{E_R - E_D}{k_B T}} \quad (4.6)$$

From each position \vec{r} the vacancy can go to four other positions, each with an exponential distribution with an average waiting time τ_1 through τ_4 . The average time it takes for the first of these transitions to take place also follows an exponential distribution, with¹:

$$\frac{1}{\tau(\vec{r})} = \frac{1}{\tau_1} + \frac{1}{\tau_2} + \frac{1}{\tau_3} + \frac{1}{\tau_4} \quad (4.7)$$

¹If we define $F(t)$ as the cumulative distribution function for the time at which the first of the four possible transitions takes place, $1 - F(t)$ is the probability that none of these events has occurred yet at time t , which is the product of the probabilities for each event to not have occurred yet. $1 - F(t) = \prod_{i=1}^n [1 - F_i(t)] = \prod_{i=1}^n e^{-\frac{t}{\tau_i}} = e^{-t \sum_{i=1}^n \frac{1}{\tau_i}}$.

This value depends on how many transitions correspond to regular diffusion, and how many involve recombination. Let us define $n(\vec{r})$ to be the number of transitions out of position \vec{r} , corresponding to regular diffusion i.e. the number of nearest neighbors of site \vec{r} within the island. So $n(\vec{r})$ is 4 everywhere, except along the border where it is 3 and at the four corners where it is 2. Using equation 4.5, the expression for $\tau(\vec{r})$ (equation 4.7) can be written as:

$$\frac{1}{\tau(\vec{r})} = n(\vec{r})\frac{1}{\tau_0} + (4 - n(\vec{r}))\frac{\lambda}{\tau_0} \Leftrightarrow \tau(\vec{r}) = \frac{\tau_0}{n(\vec{r}) + (4 - n(\vec{r}))\lambda} \quad (4.8)$$

Let $P(\vec{r}, t)$ be the probability of finding the vacancy at site \vec{r} at time t . We start with the vacancy at a random site along the border, where the corners have a doubled probability. So $P(\vec{r}, 0)$ is simply proportional to $4 - n(\vec{r})$. This must then be normalized using the dimensions of the island, x_I and y_I , to obtain:

$$P(\vec{r}, 0) = \frac{4 - n(\vec{r})}{2x_I + 2y_I} \quad (4.9)$$

There are two possibilities for the vacancy to be at site \vec{r} at time t : either it was there at $t = 0$ and has not moved since, or it came from a neighboring site at $t = t'$ and has not moved since then. This means that $P(\vec{r}, t)$ can be expressed recursively by:

$$P(\vec{r}, t) = P(\vec{r}, 0)e^{-\frac{t}{\tau(\vec{r})}} + \sum_{n.n.} \int_0^t P(\vec{r}', t')e^{-\frac{t-t'}{\tau(\vec{r})}} \frac{1}{\tau_0} dt' \quad (4.10)$$

Here the sum is over the nearest neighbors (*n.n.*), $P(\vec{r}', t')$ is the probability that the vacancy is at a neighboring site \vec{r}' at time t' , dt'/τ_0 is the probability that the vacancy goes from \vec{r}' to \vec{r} in a time interval dt' , the exponential is the probability that the vacancy does not leave \vec{r} in the time interval $[t', t]$, and the integral is over all possible values of t' .

The expected total amount of time $E_{time}(\vec{r})$ (notice that this is an expectation value, not an energy) that the vacancy is at \vec{r} is obtained by integrating $P(\vec{r}, t)$ over all t . Using the above expression this gives:

$$E_{time}(\vec{r}) = \int_0^\infty P(\vec{r}, t) dt \quad (4.11)$$

$$E_{time}(\vec{r}) = P(\vec{r}, 0) \int_0^\infty e^{-\frac{t}{\tau(\vec{r})}} dt + \sum_{n.n.} \int_0^\infty \int_0^t P(\vec{r}', t')e^{-\frac{t-t'}{\tau(\vec{r})}} \frac{1}{\tau_0} dt' dt \quad (4.12)$$

By changing the variable of integration in the second part from t to $t'' = t - t'$ this simplifies to:

$$E_{time}(\vec{r}) = P(\vec{r}, 0) \int_0^\infty e^{-\frac{t}{\tau(\vec{r})}} dt + \sum_{n.n.} \frac{1}{\tau_0} \int_0^\infty \int_0^\infty P(\vec{r}', t')e^{-\frac{t''}{\tau(\vec{r})}} dt' dt'' \quad (4.13)$$

$$E_{time}(\vec{r}) = P(\vec{r}, 0) \int_0^\infty e^{-\frac{t}{\tau(\vec{r})}} dt + \sum_{n.n.} \frac{1}{\tau_0} \int_0^\infty e^{-\frac{t''}{\tau(\vec{r})}} dt'' \int_0^\infty P(\vec{r}', t') dt' \quad (4.14)$$

$$E_{time}(\vec{r}) = P(\vec{r}, 0)\tau(\vec{r}) + \frac{\tau(\vec{r})}{\tau_0} \sum_{n.n.} E_{time}(\vec{r}') \quad (4.15)$$

Multiplying both sides by $\tau_0/\tau(\vec{r})$ and inserting equations 4.8 and 4.9:

$$[n(\vec{r}) + (4 - n(\vec{r}))\lambda]E_{time}(\vec{r}) = \frac{4 - n(\vec{r})}{2x_I + 2y_I}\tau_0 + \sum_{n.n.} E_{time}(\vec{r}') \quad (4.16)$$

This gives a number of equations with an equal number of unknowns. This has exactly one solution. We now claim that this solution is that $E_{time}(\vec{r})$ is constant for all \vec{r} , and show that this is indeed one solution, and therefore the only² solution:

$$E_{time}(\vec{r}) = E_{time} \quad \forall \vec{r} \quad (4.17)$$

$$[n(\vec{r}) + (4 - n(\vec{r}))\lambda]E_{time} = \frac{4 - n(\vec{r})}{2x_I + 2y_I}\tau_0 + n(\vec{r})E_{time} \quad (4.18)$$

Now $n(\vec{r})E_{time}$ can be subtracted on both sides, and then the term $4 - n(\vec{r})$ also cancels out, so that remains:

$$E_{time} = \frac{\tau_0}{(2x_I + 2y_I)\lambda} \quad (4.19)$$

which is indeed independent of \vec{r} , and a solution of equation 4.16. The expected lifetime of the vacancy is obtained by summing $E_{time}(\vec{r})$ over all \vec{r} :

$$\sum_{\vec{r}} E_{time}(\vec{r}) = \frac{\tau_0}{2\lambda} \frac{x_I y_I}{x_I + y_I} \quad (4.20)$$

It follows that for islands with the same area the vacancy lives longest in square islands. This is logical, since the vacancy visits the border less frequently than in an elongated island.

Note that at no point in the proof, it is used that the island has a rectangular shape. Equation 4.19 therefore also holds for randomly shaped (connected) islands, if $2x_I + 2y_I$ is replaced by the length of the border (and the condition of equation 4.9 is satisfied).

A more direct argument to derive equation 4.20 is to multiply the average probability to find the vacancy at the border of $\frac{2x_I + 2y_I}{x_I y_I}$ with the recombination rate of $\frac{\lambda}{\tau_0}$. At first sight, this approach might seem unjustified. After all, since the vacancy

²That is, if the equations are independent. Although the definition via $P(\vec{r}, t)$ uniquely determines $E(\vec{r})$, generally speaking, this need not be the case for these equations. However, since all states have the same energy, the claim that $E(\vec{r})$ is constant is logical

starts at the border at time $t = 0$, the situation at this time differs significantly from the average over an ensemble of surface vacancies, each with their own starting moment at the border. The probability to find the individual surface vacancy at the border at $t = 0$ is 100%. The probability of $\frac{2x_I+2y_I}{x_I y_I}$, used in our simple argument, reflects the ensemble average of the probability per vacancy to be at the border, for the present case that inside the vacancy island all positions are energetically equivalent. However, this large discrepancy is completely removed if we average the probability distribution over the entire lifetime of the vacancy, since, integrated over its lifetime, it has to reflect the average behavior of the entire ensemble, which has an equal occupation probability for each site in the vacancy island.

4.3 Exact numerical calculations

The jump length distribution of the vacancy assisted diffusion of embedded indium atoms in Cu(100), can be described with a continuum model for a radially symmetric geometry, as has been shown in [42], where it was derived that the jump length distribution $p(r)$ follows a modified 0^{th} order Bessel function.

$$p(\vec{r}) = \frac{1}{2\pi} \frac{c}{D_{eff}} K_0 \left(\sqrt{\frac{c}{D_{eff}}} r \right) \quad (4.21)$$

The width of this function is determined by the effective diffusion coefficient D_{eff} , which is proportional to the mean square displacement $\langle r^2 \rangle$ of the vacancy-indium pair; c is a parameter, associated to the recombination of the vacancy. Both D_{eff} and c are obtained from the return probabilities: $\langle r^2 \rangle \propto \frac{D_{eff}}{c} = \frac{\hat{p}_{perp} + \hat{p}_{opp}}{4\hat{p}_{rec}}$ [42]. The parameter R_{eff} introduced in the modified 0^{th} order Bessel functions in the previous chapter (equations 3.1 and 3.2) is defined as $\frac{c}{D_{eff}}$.

In addition to this analytical result, it is also possible to calculate the jump length distribution from exact numerical calculations. There are two advantages to the latter approach. First, exact numerical calculations make it relatively easy to compute the jump length distribution of a tracer particle in structures that do not have radial symmetry, such as the square islands on a (100) terrace. The second advantage is that exact numerical calculations make it easy to include the modifications of the activation energy barriers for the diffusion of a vacancy near the indium atom, as was shown in [42].

The model describes the evolution starting with the situation of an indium atom and a neighboring vacancy in the center of a large island. The recombination of the vacancy can only take place at the border of the island. The activation energy barrier for the recombination of the vacancy E_R may differ from the activation energy barrier for the diffusion of the vacancy E_D . The corresponding ratio λ between the probabilities for a recombination step and a diffusion step at the border of an island is given by equation 4.6.

Following the argument in [42] there are five possibilities. Either the vacancy recombines without trading places with the tracer particle, or the vacancy returns to the tracer particle. The vacancy can return from the same side, from the side opposite to the initial position of the vacancy or from one of the two sides perpendicular to the line connecting the initial positions of the vacancy and the tracer particle. The probability for recombination is p_{rec} , the probability for the return to the same side is p_{eq} , the probability for the return to the opposite side is p_{opp} and the probabilities for the return to each of the perpendicular sides are p_{perp} . Because the presence of the indium atom locally lowers the activation energy for the diffusion of a vacancy, the probability to return from the same side is orders of magnitude larger than all the other probabilities. Following the approach in [42], the recombination probability and the return probabilities are normalized with respect to p_{eq} .

$$\hat{p}_{eq} = 0 \quad \hat{p}_{perp} = \frac{p_{perp}}{1 - p_{eq}} \quad \hat{p}_{opp} = \frac{p_{opp}}{1 - p_{eq}} \quad \hat{p}_{rec} = \frac{p_{rec}}{1 - p_{eq}} \quad (4.22)$$

We can determine these probabilities for arbitrary island geometries and initial conditions with an exact numerical calculation, in which the diffusion steps of the vacancy are followed until it either recombines or returns to the tracer particle. The probability that a vacancy is present at site \vec{s} after n diffusion steps is $Q_n(\vec{s})$. The position of the indium atom is $\vec{0}$, the initial position of the vacancy is \vec{v} . This defines $Q_0(\vec{v}) = 1$ and $Q_0(\vec{s}) = 0 \forall \vec{s} \neq \vec{v}$. The probability that the vacancy transfers from site \vec{s}' to \vec{s} in one diffusion step is $p(\vec{s}' \rightarrow \vec{s})$. The fixed position of the indium atom at position $\vec{0}$ requires $p(\vec{0} \rightarrow \vec{s}) = 0$. The steps of the vacancy are defined by the recursive relation:

$$Q_{n+1}(\vec{s}) = \sum_{n.n.} Q_n(\vec{s}') p(\vec{s}' \rightarrow \vec{s}) \quad (4.23)$$

The sum is taken over the nearest neighbors (*n.n.*) of the position \vec{s} . Along the border of the island, the transition probabilities out of the island might differ from those within the island, depending on the value of λ . The slight changes in equation 4.23 that are caused by this are also taken into account. From equation 4.23 we can calculate the return probabilities by summing over all the steps of the vacancy. For example:

$$p_{eq} = \sum_{n=0}^{\infty} Q_n(\vec{v}) p(\vec{v} \rightarrow \vec{0}) \quad (4.24)$$

$$p_{rec} = \sum_{border} \sum_{n=0}^{\infty} Q_n(\vec{s}) p(\vec{s} \rightarrow border) \quad (4.25)$$

Figure 4.1 shows the initial configuration of the exact numerical calculation. The vacancy and the indium atom are at neighboring positions in the center of the island. In view of the rapid exchange between the indium atom and the vacancy, when they are positioned next to each other, we introduce a new set of coordinates that refer to

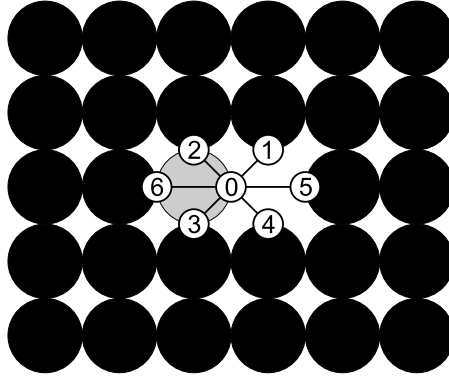


Figure 4.1: *Initial geometry used in the exact numerical calculations for the vacancy assisted diffusion of indium atoms in Cu(100). The black circles are Cu atoms, the grey circle is an indium atom, incorporated in the surface. The vacancy, shown as an absent circle, is present next to the indium atom. The numbers denote possible positions of the indium-vacancy pair. The initial configuration shown here is one of the two possibilities for position 0.*

the combined position of the atom and the vacancy. For example, the configuration of figure 4.1 is symbolized by the position marked by "0". Note that the mirrored configuration, with the indium atom and the vacancy exchanged, corresponds to the same position "0". With these new coordinates, the description of the motion is no longer dominated by the rapid back-and-forth exchange events between the atom and the vacancy, but rather concentrates on the other events, in which the vacancy is re-approaching the indium atom from one of the other sides (or annihilates). Positions 1 to 6 are the positions that can be reached in one step from position 0, where a 'step' now refers to an entire random walk of the vacancy, which either brings it back to the indium atom or leads to its annihilation at the island perimeter. Let $P_n(\vec{r})$ be the probability that the pair is at position \vec{r} after n steps. To start, we define $P_0(0) = 1$. The following steps are calculated with the recursive equation of the type.

$$P_{n+1}(0) = \frac{1}{4}\hat{p}_{perp} \sum_{i=1}^4 P_n(i) + \frac{1}{2}\hat{p}_{opp} \sum_{i=5}^6 P_n(i) \quad (4.26)$$

The probability that the indium atom ends up at a location \vec{r} , when the vacancy recombines, can now be calculated for every site in the island. For instance, the probability the indium atom ends up at site \vec{r} between 0 and 5 when the vacancy recombines is

$$p(\vec{r}) = \frac{1}{2}\hat{p}_{rec} \sum_{n=0}^{\infty} [P_n(0) + P_n(1) + P_n(4) + P_n(5)] \quad (4.27)$$

The probability that the indium atom has moved over a particular distance r when

the vacancy recombines is the sum of all probabilities $p(\vec{r})$ at a distance r from the initial position of the vacancy-indium pair.

Figure 4.2 shows the numerically computed distribution of jump lengths $p(r)$ for a tracer atom in a symmetric island with a width of 401 atomic spacings without a modified barrier for the annihilation of the vacancy at the island perimeter, i.e. for $\lambda = 1$. We obtained the return and recombination probabilities from [42], where EAM calculations for the In/Cu system had been used to obtain return and recombination probabilities for an island with a width of 401 atomic spacings at a temperature of 320 K. The return probabilities are $\hat{p}_{perp} = 0.46$, $\hat{p}_{opp} = 0.018$, the recombination probability is $\hat{p}_{rec} = 0.046$. In figure 4.2 the continuum model of equation 4.21 is also drawn in. We observe that for this simple case the numerical model is in good agreement with the continuum model. There is a mismatch between the continuum model and the numerical model for small jumps because the Bessel function in the expression for the continuum model diverges for $r \downarrow 0$.

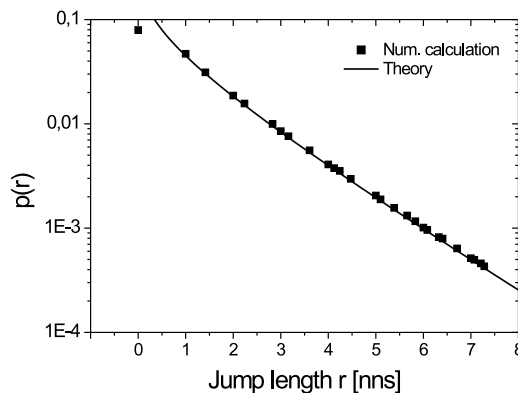


Figure 4.2: *Theoretical jump length distribution for vacancy assisted diffusion of indium atoms in Cu(100) for $\lambda = 1$. The unit of jump length is the nearest neighbor spacing (nns). The solid line is the continuum model distribution function from [42]. The solid squares are the result from the exact numerical calculations described here. The island size is 401×401 nearest neighbor distances. No modified barrier for the annihilation of the vacancy at the island perimeter was used. We obtained the return and recombination probabilities of $\hat{p}_{perp} = 0.46$, $\hat{p}_{opp} = 0.018$, the recombination probability is $\hat{p}_{rec} = 0.046$, obtained from the EAM calculations of [42].*

Figure 4.3 shows the result from the exact numerical calculation and the continuum model for different values of λ . It shows that when λ is lower than unity, i.e. when recombination is more difficult than regular diffusion, the jump length distribution is wider. This is because when recombination becomes more difficult, the vacancy has a longer life time. This makes it return more often to the indium atom and displace it on average over a larger distance.

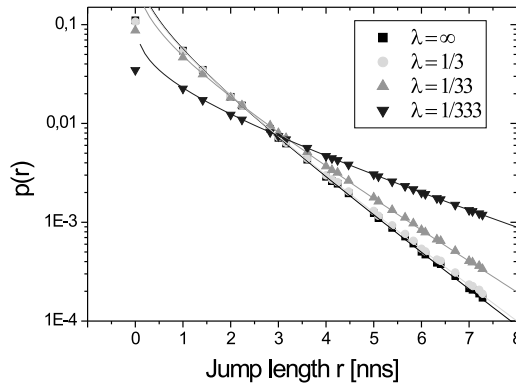


Figure 4.3: *Theoretical jump length distribution for vacancy assisted diffusion of indium atoms in Cu(100) for different λ . The solid lines result from the continuum model of [42]. The symbols are the result from the exact numerical calculations. The terrace width is 51×51 nearest neighbor distances. Jump length distributions are shown for different ratios λ between the rates for the recombination and the diffusion of a vacancy. Lower values of λ , i.e. more difficult recombination, result in displacements of the tracer atom over larger distances.*

4.4 Exact numerical calculations application in 2D islands

In the previous section we have used our exact numerical calculation to confirm earlier results by Van Gastel and Somfai et al. [41, 42]. In addition, we have briefly explored the effect of an additional activation energy for the recombination of a surface vacancy and the width of the jump length distribution. In this section, the exact numerical calculations will be used to investigate the behavior of a surface vacancy in terms of residence times and probability of visit for every individual site in a small island, the dimensions of the island being 54×43 atomic spacings, equal to those of the island used for the analysis of the measurements in Chapter 3.

In order to find the residence time of a vacancy with an exact numerical calculation, the discrete equivalent of $P(\vec{r}, t)$ has to be determined. In the exact numerical calculation, time is not continuous, but proceeds in discrete steps, which we choose to match the average time between two subsequent jumps of a surface vacancy. Now $Q_n(\vec{s})$ is defined as the probability that the vacancy is found at site \vec{s} at time step n given that it started in the origin at $t = 0$. At every time step $n \rightarrow n + 1$, the vacancy is transferred to one of its nearest neighbor positions. The corresponding recursive relation is

$$Q_{n+1}(\vec{s}) = \frac{1}{4} \sum_{n.n.} Q_n(\vec{s}') \quad (4.28)$$

If the vacancy is located next to a boundary (step edge), a further displacement of the boundary will lead to its annihilation. The rate for this differs from the normal diffusion rate by a factor λ . Here, we consider the case where $\lambda < 1$, i.e. where annihilation is suppressed. In our calculation of the discrete evolution of the probabilities, we simply account for the reduced annihilation rate by adding an amount $(1 - \lambda)Q_n(\vec{s})$ to the righthand side of equation 4.28, for positions \vec{s} along the border (and a double correction for corner positions, next to two step sites).

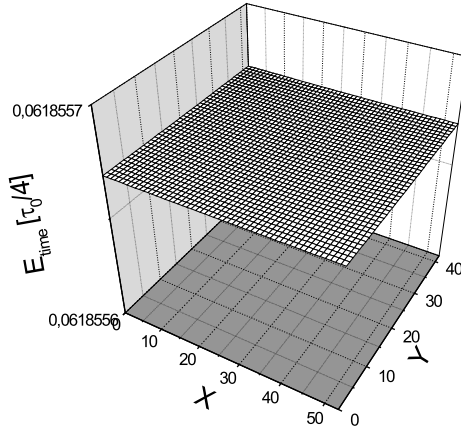


Figure 4.4: Exact numerical calculation for the expected amount of time each site is occupied by a surface vacancy during the lifetime of that vacancy. The surface vacancy starts at a random position at the perimeter of an island with dimensions 54×43 nearest neighbor distances. The value for $\lambda = \frac{1}{3}$ (temperature dependence is absorbed into λ). As shown in equation 4.17, the residence time does not depend on the location within the island.

The discrete equivalent of equation 4.11 is

$$E_{time}(\vec{s}) = \sum_{n=0}^{\infty} Q_n(\vec{s}) \quad (4.29)$$

The unit of time is the expectation value for the time of one diffusion step $\frac{1}{4}\tau_0$, where $\frac{1}{\tau_0}$ is the exchange rate of the vacancy with each of the four nearest neighbor Cu atoms. The result of the exact numerical calculation is the expectation value for the amount of time each site in an island is occupied by the vacancy, during the full lifetime of the vacancy. The result for a vacancy island, sized 54×43 nearest neighbor distances and $\lambda = \frac{1}{3}$ (temperature dependence is absorbed into λ) is shown in figure 4.4. The vacancy initially starts at a random position at the perimeter of the island. Figure 4.4 confirms the solution of equation 4.17 that E_{time} does not depend on the location within the island. Furthermore, the value of the average residence

time per site in figure 4.4 matches the prediction of equation 4.19 precisely.

$$E_{time} = \frac{\tau_0}{\lambda} \frac{1}{2(x_I + y_I)} = 0.06185567 \frac{1}{4} \tau_0 \quad (4.30)$$

The exact numerical calculations enable us to also compute the probability that the vacancy has visited a site at least once, for each site inside the vacancy island. The probability that a vacancy is at site \vec{s} after n steps, and has not visited site ν yet is written as $Q_{\nu,n}(\vec{s})$. This probability must obey the following recursive relation

$$Q_{\vec{\nu},n+1}(\vec{s}) = \sum_{n.n.} Q_{\vec{\nu},n}(\vec{s}') p(\vec{s}' \rightarrow \vec{s}), \quad (4.31)$$

where the sum of course excludes the contribution from site ν , if that would be one of the nearest neighbors of s . We can formally include that contribution by extending our definition to $Q_{\nu,n}(\nu)$ as the probability that the vacancy visits position ν for the first time in the n^{th} time step. In order for equation 4.31 to remain valid with this definition we need to choose the probability $p(\vec{\nu} \rightarrow \vec{s})$ to be identical to zero. The probability that $\vec{\nu}$ is visited by the vacancy at least once is

$$Q_{visit}(\vec{\nu}) = \sum_{n=0}^{\infty} Q_{\vec{\nu},n}(\vec{\nu}) \quad (4.32)$$

Relations 4.31 and 4.32, can be used to exactly compute the probability that a site is visited at least once for each individual site in the island. Figure 4.5 shows that the result strongly depends on the value of λ . For large λ , or easy recombination, the vacancy has a high probability to annihilate before visiting the center of the island. Note, that in all calculations, the vacancy starts its random walk at the island perimeter, in order to mimic the practical situation of vacancies being created at the step. In the limit of vanishingly small λ , or infinitely difficult recombination, the probability for a site to be visited at least once, becomes equal for all sites. This means that when recombination is difficult, the history of a vacancy, inside the island, is erased.

In view of this effect of λ on the ‘memory’ of the vacancy, it is interesting to observe how the probability to visit a site inside an island at least once depends on the location of creation of surface vacancies. In figures 4.6a and b the visitation probability for sites in a small island (10×10 nearest neighbor distances) is plotted for high and for low λ . In these two cases, a vacancy can only be created along the border. In figures 4.6c and d similar calculations have been performed, with the difference that in these cases the vacancy could be created with equal probability at any site inside the island. As expected, we find that for low λ , or difficult recombination of the vacancy, the results are not very different (figures 4.6b and d). This is because the large number of ‘reflections’ of the vacancy from the island edge effectively erases the memory of the vacancy’s origin. When λ is high, or recombination is easy, the change in boundary condition for the locations where surface vacancies are created, has a dramatic effect on the visitation probability distribution.

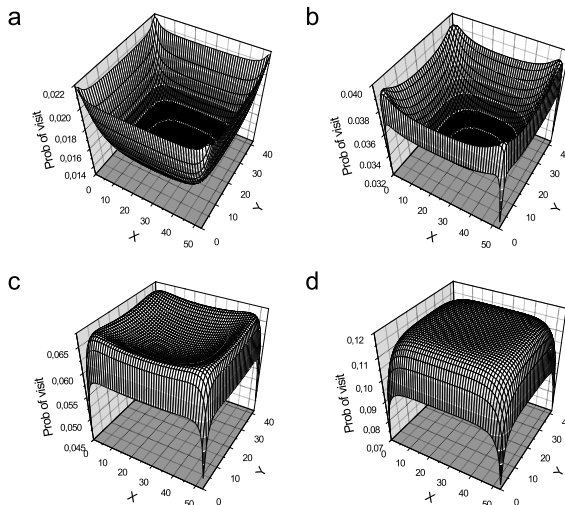


Figure 4.5: *Probability for a vacancy to visit a site at least once for various λ . a.) $\lambda = 0.5$ b.) $\lambda = 0.2$ c.) $\lambda = 0.1$ d.) $\lambda = 0.05$. The vacancy island is 54×43 nearest neighbor distances large. As λ decreases, the history that the vacancy was created at the perimeter gets more and more erased.*

4.5 Jump length distribution in small islands

In this section we employ Monte Carlo simulations to compute the dependence of the jump length distribution on the activation energy for the annihilation of a surface vacancy E_R . The geometry is again that of an island with a square lattice. The annihilation of surface vacancies only takes place at the border of the island. The presence of an indium atom in Cu(100) locally changes the diffusion behavior of the surface vacancy. This influence of the tracer particle on the behavior of the surface vacancy needs to be taken into account. The exact numerical calculations, described in section 4.4 show that the width of the jump length distribution depends on the recombination probability of the surface vacancy at the border. Here, we will model the diffusion and annihilation of a surface vacancy, after it has been created. A distribution of the modelled jump lengths will be calculated for several values of E_R . These distributions will be compared to the experimental data of Chapter 3. This approach will allow us to extract a reliable value for E_R from the experiment. Due to the complexity of the system, the Monte Carlo method is the only appropriate approach to compute the jump length distribution for the vacancy assisted diffusion of indium atoms in an island in Cu(100), for the actual island dimensions, while properly including the interactions between a vacancy and an indium atom and between a vacancy and a step.

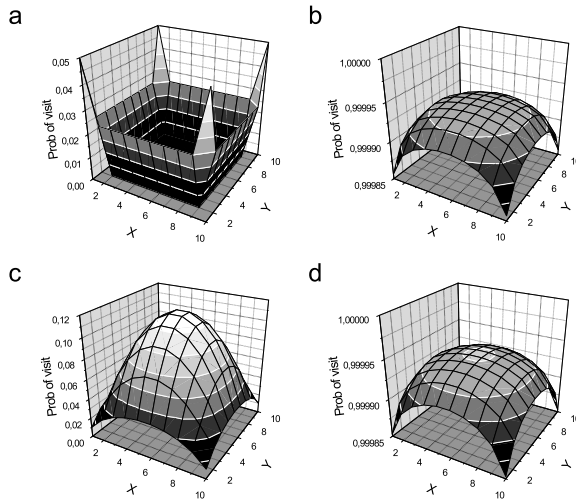


Figure 4.6: Probability for a vacancy to visit a site at least once, depending on vacancy creation site and λ . a.) creation only along the border and easy annihilation, $\lambda = \infty$, b.) creation only along the border and difficult annihilation, $\lambda = 3 \cdot 10^{-6}$, c.) creation everywhere in the island and easy annihilation, $\lambda = \infty$, d.) creation everywhere in the island and difficult annihilation, $\lambda = 3 \cdot 10^{-6}$. In all cases the vacancy island is 10×10 nearest neighbor distances large. When λ is high, the distribution of visitation probabilities depends sensitively on the vacancy creation location.

4.5.1 Monte Carlo simulations

The Monte Carlo method uses a probabilistic description of the system under consideration [100, 101]. The decision which and whether a pre-defined transition occurs at a particular time step, is made using random numbers. This allows us to construct individual trajectories of vacancies, e.g. originating at the border and diffusing through a vacancy island until they are annihilated again at the border. Even for relatively small islands, a prohibitively large number of possible trajectories exists. Therefore the simulation process is repeated only for a limited number of individual trajectories. This number is chosen sufficiently large that the averaged quantities of interest, such as the average vacancy life time, the distribution of visitation probabilities and the jump length distribution of embedded indium atoms have all converged to the values for a hypothetical exact calculation within an acceptably small statistical error. To prevent waste of computer time on non-interesting parts of the phase space of the system, the method of *importance sampling* [102] is used.

A computer has to iterate the process of interest a large number of times to find the average value of the observable. We require a pseudo random number generator that does not exhibit typical artifacts like periodicity or preferred outcomes at least for the number of iterations needed in our Monte Carlo simulation [104].

The random number generator used here is based on the random number generator supplied by the MS Visual C++ compiler. To extent its range of 2^{15} to our needs (2^{30}), the pseudo random numbers are produced by two calls to the random number generator. To prevent periodicity, the seed of the random generator is changed every golden section of the period of the combined random generator. The resulting, modified random number generator passed tests for periodicity and preferred outcomes successfully over the $\sim 10^9$ calls we use in the Monte Carlo simulation.

4.5.2 Application to jump length distributions

In this section the Monte Carlo simulation will be used to compute the dependence of the jump length distribution of indium atoms and other quantities on the activation energy for the annihilation of surface vacancies E_R . The result should be suitable for direct comparison with the experiment of Chapter 3, which will allow us to determine E_R for Cu(100). The reason to use Monte Carlo simulations is that in this case we have to model the vacancy assisted diffusion of indium atoms in a small island. For the exact numerical calculations, we had to introduce the simplification that the return probabilities for vacancies to indium atoms were not different for indium atoms close to the center of a small island and indium atoms in the center of large terraces. Due to the proximity of the border in small islands, this simplification is not justified. This, together with the interaction between the indium atom and the vacancy and the recombination probability for vacancies at the border, makes that the system is too complex for an analytical calculation.

Since we are interested in the difference between the activation energies for annihilation of a surface vacancy and for regular diffusion, we introduce the activation energy difference $E_{ES} = E_R - E_D$. In terms of this new quantity, the definition of λ (equation 4.6) becomes

$$\lambda = e^{-\frac{E_{ES}}{k_B T}} \quad (4.33)$$

We validated our Monte Carlo calculation by first reproducing the results from the exact numerical calculations in section 4.3. Vacancies were initially put next to the indium atom, in the middle of an island with a size of 401×401 nearest neighbor distances. The temperature was set at 320 K . The diffusion of each vacancy through the island was followed. As the vacancy recombined at the border of the island, the jump length of the indium atom was recorded. This process was repeated many times for several values of λ . The resulting jump length distributions were compared to the result of the exact calculations and to the experiments of reference [41]. The results from the Monte Carlo simulation were in good agreement with the experimental results and the results from exact numerical calculations.

We can now investigate the jump length behavior of the vacancy indium pair as a function of the initial location of the indium atom and the relative recombination probability λ . For the next simulations we put the vacancy and the indium atom in

an island sized 54×43 nearest neighbor distances, the size of the vacancy island in the experiments in chapter 3. The temperature was set at 288 K , the same value as in the experiments. The initial positions of the indium atom are shown in figure 4.7. The initial position of the vacancy is a random site along the border. The jump length distributions from the simulations are shown in figure 4.8. Figure 4.8 shows

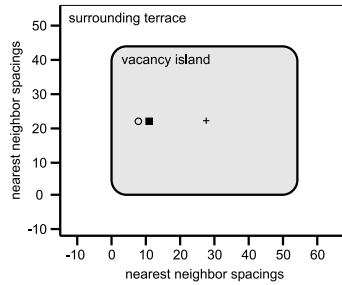


Figure 4.7: *Different initial positions for the indium atom in the Monte Carlo simulations on the position dependence of the jump length distributions*

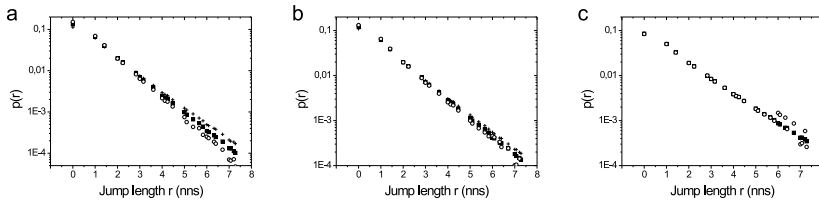


Figure 4.8: *Jump length distributions for different initial positions of the indium atom (symbols correspond to the positions indicated in figure 4.7) and various λ . a.) $\lambda = \infty$, b.) $\lambda = \frac{1}{3}$, c.) $\lambda = \frac{1}{33}$. Only for large λ , the width of the jump length distribution depends noticeably on the initial position of the indium atom. The indium atom position distributions shown in figure 4.11a and c, show that when the vacancy annihilates, the indium atom preferentially ends up at the second row. The jump length distribution of the indium atom, starting at 7 nearest neighbor spacings from the island perimeter (open circles), for low values of λ , shown in c.), exhibits a higher probability for jumps to the second row.*

that for large λ , the jump length distribution becomes narrower when the initial position of the indium is placed closer to the border. This is easy to understand. After all, when the vacancy is closer to the border, it is more likely to find the border. If the recombination probability is high, the vacancy recombines rapidly. In this case, the number of returns to the indium atom is smaller, leading to a smaller average displacement of the indium atom. When λ is small, the vacancy is more likely to ‘reflect’ from the border and return into the island. Because the vacancy is present inside the vacancy island for a longer time, it will have a larger probability

to visit all sites in the vacancy island equally often. This is supported by figure 4.6 where the probability is shown that a vacancy visits a site at least once. This effect is reflected in the jump length distributions for small λ . The width of the distribution shows almost no dependence on the initial location of the indium atom.

The principle of detailed balance dictates that when recombination of surface vacancies is easy, their creation must also be easy. The results shown in figure 4.8a represent the situation where the border of a vacancy island is an ideal source-and-sink combination for surface vacancies. Fitting the modified 0th order Bessel function of equation 4.21 to these simulation results, we can plot the width parameter $\sqrt{\frac{D_{eff}}{c}}$ of the distribution as a function of the distance to the ideal source-and-sink combination. The result of this procedure is shown in figure 4.9, which shows that as the indium is placed further away from the source-and-sink, the jump length distribution gets wider. The reason is simply that as the vacancy starts its random walk,

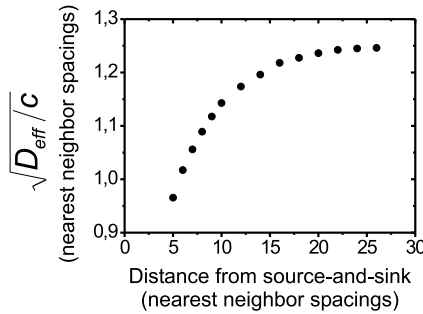


Figure 4.9: A plot of $\sqrt{\frac{D_{eff}}{c}}$ (effectively the width of the jump distance distribution) versus the distance to the nearest source-and-sink for surface vacancies. These widths were determined by fitting equation 4.21 (Bessel function) to the jump distance distributions obtained from Monte Carlo simulations and the distance to the sink was varied by adjusting the size of the vacancy island. The borders of these islands were an ideal source-and-sink for surface vacancies. This plot shows that the width of the jump distance distribution is a monotonically increasing function of the distance to the nearest sink.

after having displaced the indium atom at a larger distance from the sink, its probability to find the sink and annihilate there before returning once more to the indium atom is reduced. This means that the lifetime of the vacancy is increased and thus it returns on average more often to the indium atom, resulting in a larger average displacement and a wider jump length distribution.

4.5.3 Application to the distribution of indium atom positions

This section describes simulations to determine the redistribution of the indium atoms in an island. The geometry of the Monte Carlo simulation is a vacancy island with a size of 54×43 nearest neighbor distances. The initial position of the indium atom is a randomly chosen site in the top layer inside the vacancy island. The initial position of the vacancy is a randomly chosen site along the border of the vacancy island. After the vacancy has diffused through the island, it recombines with probability λ at the border of the island. Immediately after this event, a new vacancy is created again at a random site along the border of the vacancy island. The temperature is set at 288 K , the temperature of the experiment. The simulations differ with respect to the previous simulations in the sense that after the recombination of a surface vacancy, the position of the indium atom is *not* reset.

In these simulations indium atoms were allowed to reside right at the border of the vacancy island. This aspect requires us to pay attention to how the presence of the indium atom, locally influences the rates of annihilation and creation of surface vacancies. We used the diffusion barriers for vacancies close to an indium atom, as calculated by Somfai et al. with the Embedded Atom Model [42], and combined these with the condition of detailed balance to determine by which factor the vacancy annihilation and creation rates were modified by the presence of a nearby indium atom.

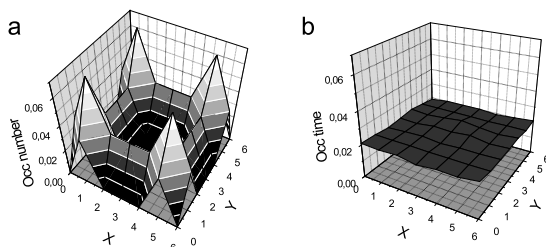


Figure 4.10: *a.) Distribution of the location where indium atoms end up when the vacancy is annihilated, obtained from a Monte Carlo simulation. b.) The corresponding distribution of the average time spent by the indium atom per site on the surface is completely flat. This shows that the structure in the distribution of panel (a) is a purely kinetic effect, the presence of the indium near the border leading to enhanced rates of creation and annihilation of surface vacancies. In both figures, the island dimensions are 7×7 nearest neighbor distances, $\lambda = \frac{1}{333}$ and temperature $T = 288\text{ K}$. Precisely the same result is obtained from the equivalent exact calculation (not shown here).*

In figure 4.10a the distribution is shown of where indium atoms end up when the vacancy is annihilated for a small vacancy island, as obtained from the Monte Carlo simulation. It shows the surprising result that the indium atoms most often end up at the second row from the border. Precisely the same result is obtained

from the equivalent exact calculation (not shown here). This distribution seems to defy equilibrium thermodynamics, since there is no energetic preference for any site in the island for the indium atoms, also not for the second row from the border. However, figure 4.10a is *not* the probability distribution of indium atoms within the island. For that distribution, one should also take into account the time the indium atom spends at each site in the vacancy island. Near the border, this time is the inverse creation rate of vacancies per site. As the presence of the indium atom near the border lowers the activation energy for the creation of vacancies, this creation rate is significantly increased and the amount of time that the indium atom spends near the border until its next jump is reduced accordingly. Figure 4.10b shows the distribution for the time an indium atom on average spends at each site. In accordance with thermodynamics, this visitation time distribution is flat, thus if one would measure the position of an indium atom at regular time intervals, one would find the indium atom equally often everywhere. Similar results have been

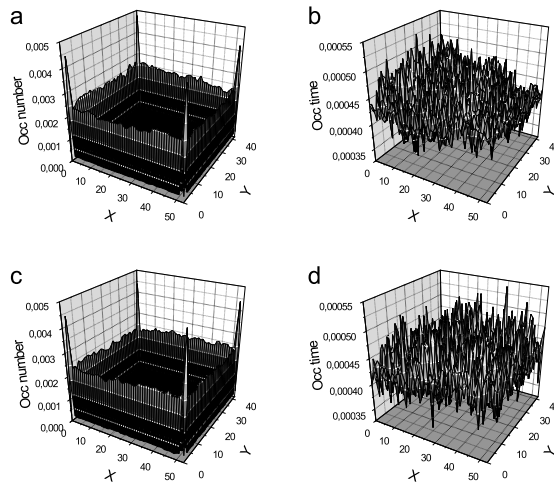


Figure 4.11: *Distribution of the positions where indium atoms end up when a vacancy is annihilated, obtained from a Monte Carlo simulation for a.) $\lambda = 0.1$ and c.) $\lambda = 0.01$. Corresponding distributions of average time spent by the indium atom per lattice site for b.) $\lambda = 0.1$ and d.) $\lambda = 0.01$. For both calculations, the island dimensions were 54×43 nearest neighbor distances and temperature was $T = 288$ K. For this large island, exact calculations could not be performed. Therefore only simulation results are shown.*

obtained from simulations for larger islands, of the size used in the experiments (figure 4.11) and from exact calculations for small islands. Figure 4.11a shows the position distribution and figure 4.11b shows the distribution of average visitation times for a relatively high $\lambda = 0.1$, figure 4.11c and figure 4.11d show equivalent results for a relatively low $\lambda = 0.01$. Again, the sites where the indium atom ends

up with the highest probability, are on the second row. However, the rate at which the indium atom leaves these sites is so high that the fraction of time spent per site by the indium atom is equal for all sites inside the vacancy island. Figures 4.11b and 4.11d confirm the expectation that the shape of the visitation time distribution does not depend on λ .

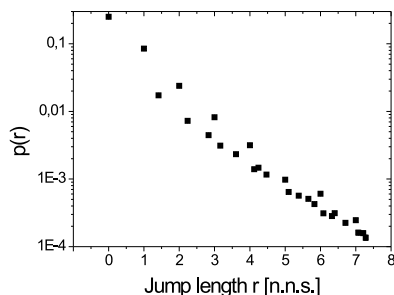


Figure 4.12: *Distribution of lengths of jumps from the second row from the border of the vacancy island, obtained from Monte Carlo calculations. The island dimensions were 54×43 nearest neighbor distances, $\lambda = \frac{1}{33}$ and the temperature $T = 288$ K. Jump lengths are expressed in nearest neighbor distances (n.n.d.).*

The effect of the increased number of visits to the second row by the indium atom, and the higher mobility to leave from there, has an influence on the jump length distribution, as shown in figure 4.12. Jump lengths of an integer number of nearest neighbor distances have a higher probability, which is caused by jumps from the second row, to another location within the second row. Because at larger jump lengths there are more jump vectors from the second row into the island than to another location within the second row, the effect becomes smaller for larger jump lengths. Precisely this effect has also been responsible for the few higher points in the jump length distribution of figure 4.8c, for low λ and an indium atom position close to the island edge.

4.6 Recombination barrier at the upper and lower sides of a step

In order to obtain an estimate for the additional energy barriers for vacancy recombination from the lower side and from the upper side of a step, we confronted the measurements of Chapter 3 with the results of Monte Carlo simulations, of the type described in the previous section. Several values for the relative recombination probability λ were used in these simulations. Equation 4.33 associates the value of

λ with the difference E_{ES} between the activation energy for the annihilation of a surface vacancy and the energy barrier for regular vacancy diffusion.

We first concentrate on the annihilation of surface vacancies from inside the vacancy islands, i.e. vacancy annihilation from the lower terrace. Selected results from our Monte Carlo simulations are shown in figure 4.13 together with the experimental data from figure 3.5. Figure 4.13 shows that the simulated jump length

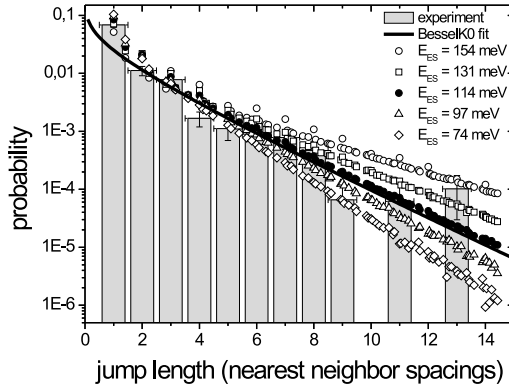


Figure 4.13: *Jump distance distribution inside a vacancy island. Plotted are the experimental data of Chapter 3 (grey bars), the 0^{th} order modified Bessel function fitting the experimental data (solid black line) and the jump distance distributions from five Monte Carlo simulations. These Monte Carlo calculations, simulate the "slide puzzle" diffusion of an In atom inside a vacancy island of 54×43 nearest neighbor distances, which is the same size as the vacancy island used in the experiment. For each simulation a different value was used for the activation energy for the annihilation of a surface vacancy at the edge of the vacancy island. The simulation with an energy barrier of 114 meV best fits the Bessel function and the experiment and the other simulations serve to illustrate the sensitivity of the distribution to this energy barrier.*

distribution with $E_{ES}^{inside} = 114 \text{ meV}$ best fits the experimental data, albeit with a large statistical error margin of 30 meV.

A similar procedure was followed for the experimental jump length distribution of figure 3.5 for indium atoms outside the vacancy island. The result is shown in figure 4.14. The two simulated jump length distributions in figure 4.14 are for activation energies for the annihilation of surface vacancies of 0 meV and -114 meV , i.e. for the absence of an additional barrier or for the case of an extreme lowering of the barrier even with respect to that for regular diffusion. The two computed distributions are nearly identical; only in the case of an enhanced barrier, the distribution is changed (cf. figure 4.13). Changing the parameter λ in the calculation cannot make the distribution any steeper. Nevertheless, the experimental distribution is steeper than the two simulated distributions. There are several potential reasons for

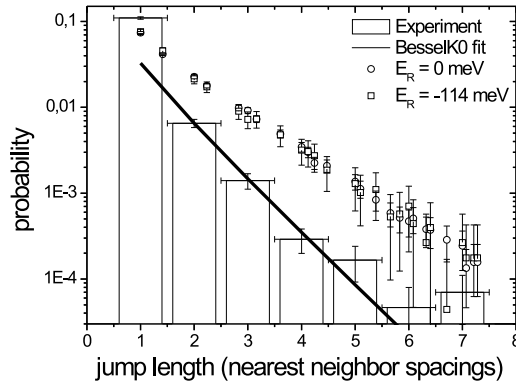


Figure 4.14: *Jump distance distribution outside a vacancy island. Plotted are the experimental data of Chapter 3 (white bars), the 0^{th} order modified Bessel function fitting the experimental data (solid black line) and the jump distance distributions from two Monte Carlo simulations. In the Monte Carlo simulations, the used range of distances to the step was between 5 and 15 nearest neighbor distances, similar to the procedure followed in the experiment (Chapter 3). The activation energy for the annihilation of a surface vacancy approaching the step from the upper side is set to 0 meV in one simulation, and to -114 meV (reduced barrier) in the other. The results of the two simulations almost coincide, but even at these low values for the energy barrier, the simulated jump distance distributions are wider than the experimental distribution.*

the discrepancy between calculation and experiment for the jump length distribution outside the island. In the experiment, there were several indium atoms close together, which may have had an effect on the diffusion properties of the vacancies that was not included in the model. As discussed in section 3.4.3, stress relaxation at the step edge should be expected to enhance the diffusion rates on the upper terrace, close to the step, effectively biasing the random walk of the vacancy to the step and thereby reducing the return probabilities of the vacancy to the indium atom in the upper terrace. This in turn should result in a smaller average displacement of the indium atom. The measurements of the vacancy-mediated diffusion on the upper side of a step, were performed next to a relatively small vacancy island, located inside a large vacancy island. The ‘reflection’ of vacancies at the lower side of the border of this larger island, might cause the vacancies to visit the upper side of the border of the smaller vacancy island more often. This could lead to an unusually narrow jump distance distribution. At this point, we can only conclude that the activation energy for the annihilation of surface vacancies at the upper side of a step is low, $E_{ES}^{\text{outside}} \lesssim 0$ meV.

4.7 Vacancy encounter probability as a function of the distance to an ideal source-and-sink

In this section we use Monte Carlo simulations to quantify the systematic error that has been made in the initial analysis of the STM data of vacancy-mediated diffusion of embedded indium atoms in Chapter 3. Measurements analyzed in Chapter 3 for the motion of indium atoms outside the vacancy island were performed in an area between 5 and 15 nearest neighbor distances from the edge of the vacancy island, as indicated in figure 4.15. At this distance we must have measured an effective $\sqrt{\frac{D_{eff}}{c}}$

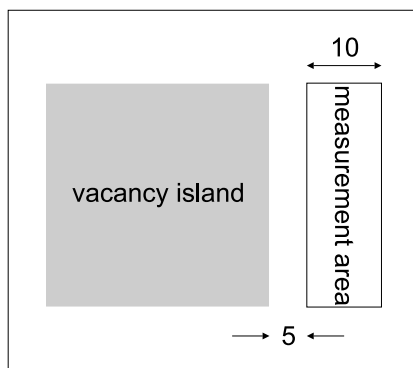


Figure 4.15: *The jump distance distribution outside the vacancy island (grey area) was not measured directly at the step, but in an area of 10 nearest neighbor distances wide, starting at a distance of 5 nearest neighbor spacings from one edge of the vacancy island.*

that is higher than the $\sqrt{\frac{D_{eff}}{c}}$ that a measurement would have yielded directly at the step (cf. figure 4.9). The vacancies that are created and annihilated without leaving the area between 0 and 5 nearest neighbor distances from the step, are never detected. This has introduced a systematic error in our analysis of the jump length and waiting time distribution measured for indium atoms in the upper terrace. This error has made our initial estimate of the difference in activation energy for the creation of surface vacancies inside and outside a vacancy island too low.

Using Monte Carlo simulations for precisely the geometry of figure 4.15, we have calculated the probability that a vacancy, once it is created, reaches a distance from the step of 10 nearest neighbor spacings. The outer contour of figure 4.15 is also an upward step, i.e. the vacancy island of interest is located inside a bigger vacancy island. In section 4.6 we found the high activation barrier for the creation of vacancies on the lower side of a step. We expect only a low number of surface vacancies created at the lower side of the border of this bigger island. Therefore, in the model, we ignore the presence of the border of this bigger island and instead we locate the vacancy island of interest inside a large terrace.

The procedure in the calculations was as follows. New vacancies were created on the upper terrace in the atom row directly adjacent to the grey vacancy island in figure 4.15. The diffusion of each vacancy was followed until its annihilation, again at the edge of the vacancy island. During its diffusion, the vacancy had the possibility to enter the measurement area, marked by the rectangle in figure 4.15. From this simulation we obtained the probability for vacancies in the upper terrace to reach the n^{th} atom row from the border of the vacancy island, before recombining. Once a vacancy is at the n^{th} row, it is able to displace an indium atom at this distance from the border of the vacancy island. The probability that a surface vacancy reaches the n^{th} row can be expressed formally as a Boltzmann factor with an activation energy E_P . This energy serves as the systematic error in the activation energy difference for the creation of a surface vacancy inside and outside a vacancy island that we obtained from the analysis of the motion of the indium atoms in Chapter 3.

The average probability that a vacancy, once created, encounters an In-atom on the terrace on the lower side of the step before it annihilates is defined as p^{inside} . This probability was determined to be 0.7, based on simulations with the annihilation barrier E_{ES}^{inside} of 114 meV, determined above. In other words, surface vacancies created inside the vacancy island encountered on average 70% of the embedded indium atoms before their annihilation. Because of the multiple reflections of the vacancies from the island edges, caused by the annihilation barrier, p^{inside} did not depend noticeably on the distance of the indium atoms to the edge. The probability $p^{outside}$ can be defined in a similar way for a vacancy encountering an In atom on the terrace on the upper side of the step.

In the one-dimensional case, the probability that a vacancy, on the k^{th} row does not pass the n^{th} row before recombining is defined as $P_k(n)$. This probability $P_k(n)$ is equal to the probability that the vacancy moves to site $k \pm 1$, multiplied by $P_{k\pm 1}(n)$ for both $+1$ and -1 . Starting at $P_1(n)$ where the vacancy can diffuse into the terrace or annihilate, $P_k(n)$ is described by the following set of equations:

$$P_1(n) = \frac{\lambda + P_2(n)}{\lambda + 1} \quad (4.34)$$

$$P_k(n) = \frac{1}{2}(P_{k-1}(n) + P_{k+1}(n))$$

$$P_n(n) = \frac{1}{2}P_{n-1}(n)$$

Where λ is defined in equation 4.33. Solving these equations leads to:

$$P_k(n) = (n - k + 1)P_n(n) \quad (4.35)$$

Inserting equation 4.35 into equation 4.34 gives after simplification

$$1 - P_1(n) = \frac{1}{1 + n\lambda} \quad (4.36)$$

Here $1 - P_1(n)$ is $p^{outside}$, the probability that a vacancy created at the upper side of a step *does* pass the n^{th} row before recombining.

$$e^{-\frac{E_P}{k_B T}} = p^{outside} = \frac{1}{1 + n e^{-\frac{E_{ES}}{k_B T}}} \quad (4.37)$$

In the limiting case that $E_{ES} \rightarrow +\infty$

$$E_P \rightarrow 0$$

In the limiting case that $E_{ES} \rightarrow -\infty$

$$E_P \rightarrow k_B T \ln(n) - E_{ES}$$

In our case E_{ES} on the upper side of the step is small, thus the latter limit applies to our case. For two dimensions, an equivalent model can be constructed. The probabilities P_k can be found with exact numerical calculations, in essentially the same way as in equations 4.24 and 4.25. Figure 4.16, shows the result of the 2-dimensional exact numerical calculations of the probability that a vacancy reaches a distance n of 5, 10 and 15 nearest neighbor distances from the step for various recombination energies. We plotted the sum of E_P and E_{ES} as a function of E_{ES} . We expect the value of $E_{ES}^{outside} \lesssim 0 \text{ meV}$. Figure 4.16 shows that for $E_{ES} =$

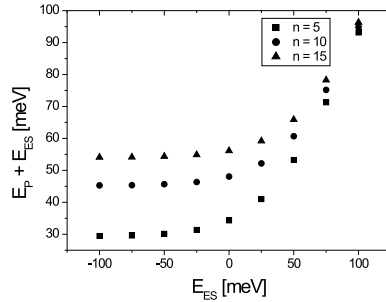


Figure 4.16: The sum of E_P and E_{ES} as a function of E_{ES} for various distances to the step n .

0, the values of E_P for n values of 5, 10 and 15 nearest neighbor distances, are respectively 34 meV , 48 meV and 56 meV . Averaging these values gives us the error that this effect has introduced in the experimentally determined difference between the activation energies for the formation of a surface vacancy at upward and downward steps. $E_F^{inside} - E_F^{outside}$ is lowered by $46 \pm 11 \text{ meV}$. The error margin is determined from the spread in the calculated values of E_P for n is 5, 10 and 15 nearest neighbor distances. Note that this effect is strongest on the side

of the step where the additional activation energy for the formation/annihilation of a surface vacancy is small (or negative), as is the case outside the vacancy island, while it is as good as absent when this energy is large and positive, as is the case on the inside. With this correction, the true activation energy difference for the creation of surface vacancies between the upward and downward steps is:

$$\Delta E_F^{inside} - E_F^{outside} = 136 \pm 12 meV$$

With this new activation energy difference for the creation of surface vacancies, taking all the error margins into account, we can construct a nearly complete energy landscape for a surface vacancy at a close-packed step on the Cu(100) surface, where the information on the lower side of the step is consistent with that on the upper side.

4.8 Conclusion

The energy diagram shown in figure 4.17, forms the conclusion of the combined experimental and theoretical analysis of vacancy-mediated diffusion of embedded indium atoms in Cu(100), as presented in Chapter 3 and Chapter 4. It shows that surface vacancies are created predominantly at the upper side of a step, while the step acts as an efficient mirror for surface vacancies approaching it from the lower side. In order to complete figure 4.17, we have combined the activation energy difference for the formation and annihilation of surface vacancies and the activation energy difference for the diffusion of vacancies inside and outside the vacancy island, obtained from the experiments in Chapter 3 and the analysis in this chapter, with the activation energy for the diffusion of surface vacancies and the formation energy of a surface vacancy, obtained from Embedded Atom Model calculations in [41, 58]. The sum of the latter two energies has been experimentally determined in reference [41] to be $717 \pm 30 meV$. Chapter 5 describes the experiments performed to obtain a separate experimental value for the activation energy for the diffusion of surface vacancies.

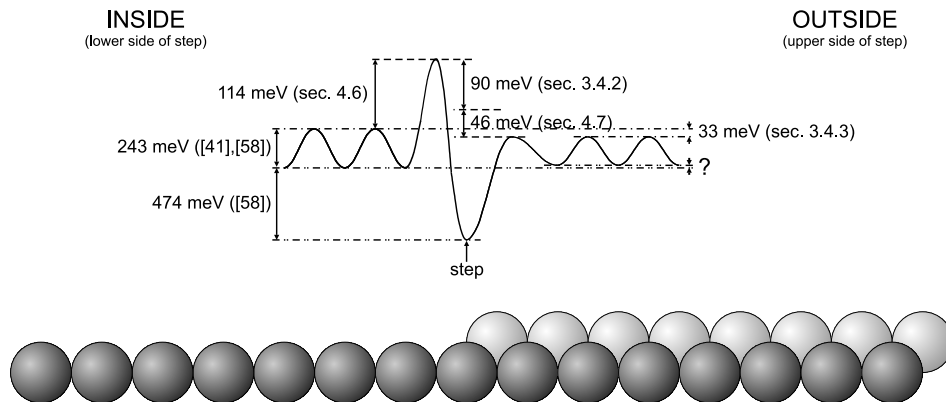


Figure 4.17: *Energy landscape for the creation of a surface vacancy and the diffusion of an indium-vacancy pair. The references between brackets next to each energy value, show from which section or publication the energy is obtained. The deep minimum corresponds to the ground state situation without a surface vacancy. Inside the vacancy island the activation energy for the creation of surface vacancies is 136 meV higher than outside the vacancy island. Accordingly there is also an activation energy barrier for the annihilation of surface vacancies that approach the step from the lower side. This causes the mirror effect at the lower side of a step for surface vacancies. Outside the vacancy island, the activation energy for the annihilation of surface vacancies is at most as high as the diffusion barrier and an annihilation barrier lower than the diffusion barrier cannot be ruled out. The activation energy for the diffusion of the indium-vacancy pair is 33 meV lower in the upper terrace in the immediate vicinity of the step. We ascribe this effect to stress relaxation at the step. The creation energy of surface vacancies was taken from calculations with the Vienna ab initio simulation package (VASP) published in [58]. The diffusion barrier for the indium-vacancy pair was obtained by subtracting this calculated vacancy creation energy from the experimental value obtained in [41] for the sum of the activation energy for the diffusion of the indium-vacancy pair and the creation energy of a surface vacancy.*

CHAPTER 5

Direct observation of the diffusion of an individual surface vacancy

This chapter describes the low-temperature STM experiment and its analysis that we have performed to acquire direct information on the diffusion characteristics of an individual surface vacancy in Cu(100). The result is in excellent agreement with the prediction of the activation energy for the diffusion of surface vacancies, obtained from first-principles calculations. The experimental information on the diffusion barriers forms the closing piece of our analysis, started in Chapter 3 and 4, of the energy landscape for the formation, diffusion and annihilation of surface vacancies in the Cu(100) surface.

5.1 Introduction

Chapters 3 and 4 have presented experimental and theoretical results mainly on the creation and annihilation of surface vacancies in Cu(100). In this chapter, the focus is on the energetics of the random walk a vacancy performs between these two events. The special shape of the jump length distribution of embedded indium atoms (modified 0th-order Bessel function), found in this thesis (Chapter 3) and in previous work [36, 39, 41, 42, 43], indicates that the surface vacancies in Cu(100) behave like random walkers that diffuse through the top layer following a "slide puzzle" mechanism [38]. Calculations by Grant et al. [58] using the VASP (Vienna *ab initio* simulation package) [105, 106, 107, 108] total energy code, employing ultra-soft pseudo potentials [109, 110, 111, 112] and the Perdew-Wang 1991 version of the generalized gradient approximation [113], have predicted a formation energy for a surface vacancy in Cu(100) of 474 *meV*. The value for the sum of the vacancy formation energy and the activation energy for the diffusion of a surface vacancy in this surface has been measured by Van Gastel et al. [41] to be 717 ± 30 *meV*. Subtracting these two numbers, we arrive at an estimate for the activation energy for the diffusion of a surface vacancy of 243 ± 30 *meV*. In this chapter, we use low-temperature observations on Cu(100) to directly determine the activation energy for the diffusion of surface vacancies. Together with the above experimental value for the sum of the formation and diffusion energies this provides us with an experimental value for the formation energy of a surface vacancy.

5.2 Experimental procedures

The experiments described in this chapter have been performed in the new programmable temperature STM system described in section 2.4. The Cu sample was cut by spark erosion from a 5N purity single crystal. The crystal was chemically etched and polished parallel to the (100)-plane with an accuracy of 0.1° [90]. After introduction into the ultra high vacuum system, with a base pressure of $2 \cdot 10^{-10}$ *mbar*, the sample was further cleaned with several cycles of ion bombardment with 1000 *eV* Ar⁺ ions and annealing to 690 *K* [91]. The ion bombardment was performed with a focused, differentially pumped ion gun, fitted with a Wien mass filter. The condition of the freshly cleaned sample is shown in figure 5.1. After cleaning the sample, it was cooled by a He-cooled flow cryostat to a temperature of 85 *K* in about 150 minutes. While the sample was cooling down, we noticed some condensation of residual gas on the sample. Most of these impurities could be removed by flashing the sample quickly to 373 *K*, and letting it cool rapidly to 85 *K* again. As was estimated already in Chapter 3, at this temperature, the density of spontaneously created vacancy islands is so low that we would have to search a surface area, the size of a small city to find just one vacancy. This forces us to create the surface

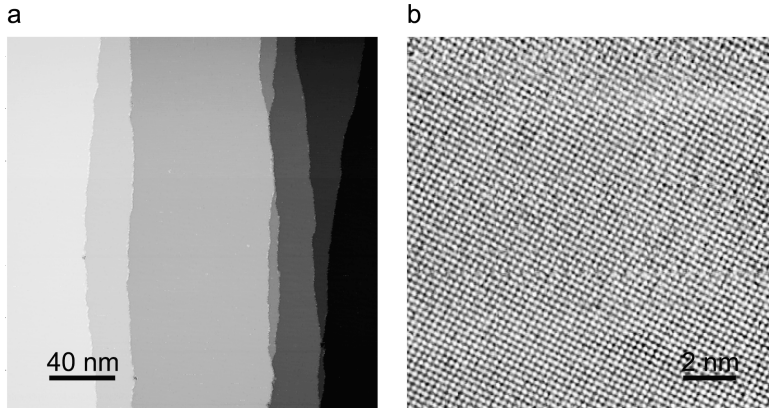


Figure 5.1: STM images of the surface condition of the Cu(100) sample after the cleaning procedure. a.) Large scale image of the Cu(100) surface. The image was processed by adding the image containing the error (dZ) signal to the standard height image as described in [78]. $T = 293$ K, $V_t = -0.50$ V, $I_t = 0.1$ nA. b.) Small scale image of the Cu(100) surface. The copper atoms in the square lattice of Cu(100) are clearly visible. To increase contrast, the original and the differentiated height maps have been mixed. $T = 99$ K, $V_t = -0.04$ V, $I_t = 0.5$ nA.

vacancies ourselves. The vacancies were created with an Ar^+ ion erosion treatment on a freshly prepared surface at 85 K. At the employed ion energy of 500 eV, the maximum ion current density from the focussed ion gun was $2.2 \cdot 10^{-5}$ A/m² at a beam diameter of 9 mm. When the ion energy was lowered further, the ion current rapidly became too low to be useful. Within an enthalpy of vaporization of copper of $\Delta_f H^0 = 337.4 \pm 1.2$ kJ/mol [114], the energy required to remove a single atom from a copper crystal is 3.5 eV. The ion energy of 500 eV was clearly too high to create individual vacancies. Indeed, after irradiating the surface at this energy we observed that the majority of impact sites were small vacancy islands with nearby adatom clusters [59]. Therefore, we lowered the ion impact energy to 50 eV by applying a bias voltage to the sample of 450 V. This still mostly resulted in multi-atom defects i.e. small vacancy islands and adatom clusters, but individual missing atoms, i.e. single surface vacancies, were also occasionally observed. The low-temperature, 50 eV ion erosion treatment formed the final step in the preparation of the surface. In this respect, we obtained our best result for 0.01 ML of removed atoms, which we could obtain at an ion dose of approximately $1.4 \cdot 10^{10}$ ions/cm². After this final preparation step, the STM scan head was placed over the sample and the STM tip was brought into tunnelling range. At the end of this procedure the mechanical contact between the coarse-approach piezo motor and the sample holder was lifted, which resulted in a further lowering of the sample temperature to 77 K. This is the temperature at which the STM measurements have been performed. The time passed between the low-temperature ion erosion treatment and the STM obser-

vation was typically 80 minutes, which was short enough at the temperature of 77 to 85 K that individual vacancies could still be observed, i.e. not all had annihilated before the first STM images were recorded.

5.3 Qualitative observation and quantitative analysis

For the low-temperature STM observations we set the tunneling conditions such, that the atomic lattice of Cu(100) was clearly visible. Typically, this was achieved for a tunnelling (sample) voltage of 0.15-0.30 V and a tunnelling current of 0.1 nA . The temperature of the sample was $77 \pm 2 K$. Areas of $20 \times 20 nm^2$ were searched for impact sites resulting from the low energy ion erosion treatment. When such an impact site was found, the field of view was reduced to $10 \times 10 nm^2$, in search for a possible, single surface vacancy in the direct vicinity of the impact location. When a vacancy was found, the motion of the vacancy was followed by imaging the same area multiple times, until the vacancy had moved out of the field of view. Unfortunately, we have been able to perform only 5 of such observations, which has resulted in a high error margin on the diffusion activation energy (see below). The motion of a single surface vacancy is shown in figure 5.2. The white arrow points at

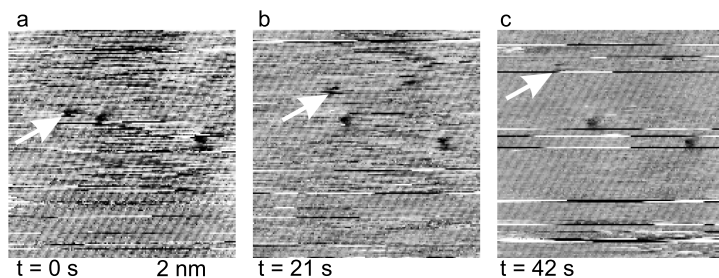


Figure 5.2: A sequence of three consecutive STM images of ion erosion damage on Cu(100) at $77 \pm 2 K$. The arrow points at a single surface vacancy, diffusing through the surface. The acquisition time for each frame was 21 s. $V_t = -0.29 V$, $I_t = 0.1 nA$.

the surface vacancy. Two other dark regions can be seen in figure 5.2, which are two- or three-vacancy clusters. We have observed many of such nano-clusters. Although these were not mobile at 77 K , they did fluctuate in shape (orientation). The high resolution images allow us to determine the displacement of the surface vacancy by simply counting the number of atoms between its initial and its final position. In this procedure we corrected for the modest amount of drift (thermal drift and piezo creep) between consecutive images. From the acquisition time per image, and the mean square displacement of the surface vacancies over all consecutive images, we have determined an average jump rate for surface vacancies in Cu(100) at $T = 77 K$ to be $\nu_{jump} = 0.18 \pm 0.1 Hz$.

Unfortunately, we have only obtained reliable results at a single temperature. As a consequence, we cannot construct the Arrhenius plot for surface vacancy diffusion, $\ln(\nu_{jump})$ versus the inverse temperature, and determine the activation energy and the pre-exponential factor (attempt frequency) for this process independently. Instead, we simply assume that the process obeys the Arrhenius law

$$\nu_{jump} = \nu_0 e^{-\frac{E_D}{k_B T}} \quad (5.1)$$

where ν_0 is the attempt frequency and E_D is the activation energy. For the value for the attempt frequency we take $1 \cdot 10^{13} \text{ Hz}$. With relation 5.1 we can now determine the activation energy for the diffusion of a single surface vacancy to be $210 \pm 34 \text{ meV}$. This last piece of information completes the puzzle of the life cycle of a surface vacancy in Cu(100).

5.4 Birth, life and death of a surface vacancy in Cu(100)

We start this section by comparing the diffusion energy determined above with the sum $717 \pm 30 \text{ meV}$ of the formation and diffusion energies of surface vacancies in Cu(100), determined in the experiment of van Gastel et al. [41]. The difference between these two experimental numbers of $507 \pm 45 \text{ meV}$ is our experimental value for the vacancy formation energy in the Cu(100) surface. This number compares very favorably with the value of 474 meV obtained from *ab initio* calculations by Grant et al. [58]. We combine the energies determined here with the results of the previous two chapters to construct the final version of the energy diagram of the life cycle of an individual surface vacancy in Cu(100), now based entirely on experimental data. The result is shown in figure 5.3. The step serves as the source (and sink) of surface vacancies. The activation energy for the creation of surface vacancies is $136 \pm 12 \text{ meV}$ higher on the lower side of the step, i.e. inside the vacancy island, than on the upper side (outside), which makes the formation frequency much lower on the inside than on the outside. This difference in formation barrier is accompanied by the existence of a significant activation energy for the annihilation of surface vacancies of $114 \pm 30 \text{ meV}$ on top of the regular diffusion barrier. This causes the mirror-effect for surface vacancies at upward steps, which makes the lifetime of vacancies on the inside of a vacancy island much longer than on the outside. Outside the vacancy island, the activation energy for the annihilation of surface vacancies does not exceed the diffusion barrier. The sum of the formation energy and the activation energy for the diffusion of surface vacancies in the upper terrace in the vicinity of the downward step is $33 \pm 9 \text{ meV}$ lower than the equivalent sum of energies in the lower terrace. This effect is associated with stress relaxation at the step. We assume that the stress effect is absent inside a vacancy island, so that the diffusion barrier there is equal to the value determined by our low-temperature experiment for extended terraces.

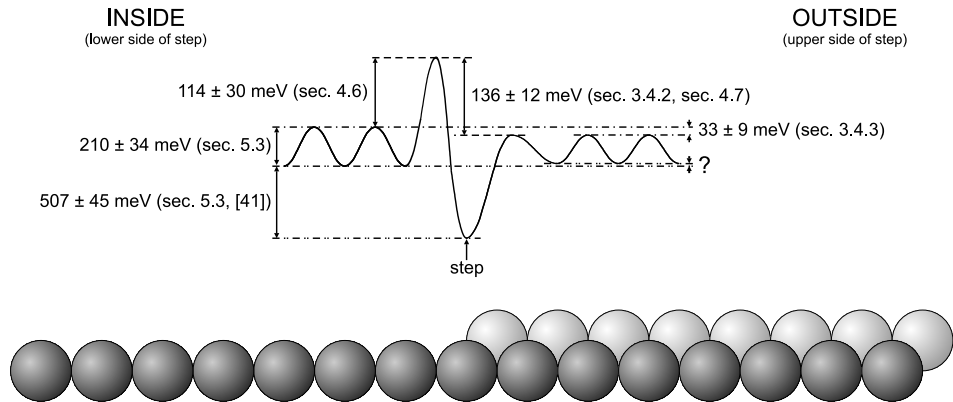


Figure 5.3: Energy landscape for the creation, diffusion and annihilation of a surface vacancy in Cu(100). The references between brackets next to the energy value, show from which section or publication the energy barrier is obtained.

With this, we have obtained a seemingly complete energy diagram for surface vacancies in Cu(100). Now that we have verified that vacancies are generated and annihilated at the steps and we know the asymmetry between vacancy creation and annihilation processes at the upper and lower sides of steps, the next questions that present themselves naturally concern the role of the step orientation. Equivalently, one may ask whether these processes are equally efficient everywhere along the step. In particular, we anticipate that kinks play a special role. Depending on the edge mobility of surface vacancies and their detachment rates from edge and kink sites, this could noticeably concentrate the formation and annihilation of surface vacancies along the $\{001\}$ oriented parts of the steps, e.g. near the ‘corners’ of vacancy and adatom islands.

CHAPTER 6

Coalescence of vacancy islands

This chapter describes STM observations of the coalescence of single monolayer deep vacancy islands in Cu(100). The coalescence mechanism of vacancy islands shows a remarkable feature. Vacancy islands are observed to diffuse through the surface. This can bring them closer to each other. We find that the vacancy islands coalesce spontaneously well before the distance between their edges has reduced to zero. This seems to be in contrast with the coalescence behavior of adatom islands on the same surface. We interpret this behavior as the consequence of a mechanical instability of the narrow strip of material between two nearly touching vacancy islands, which leads to a spontaneous rupture of the surface layer and a merger of the two vacancy islands. We argue that the tensile surface stress of Cu(100) forms the driving force behind the instability.

6.1 Introduction

In the previous chapters it was shown that vacancies on average move all the copper atoms in Cu(100) approximately once every ten seconds at room temperature. This shows that vacancies, like adatoms, can play an important role in the mobility and evolution of crystal surfaces. Vacancy diffusion provides an extra pathway for surfaces to decrease roughness.

Hoogeman et al. have shown before on Ni(100) that in a relatively short time, surfaces damaged by ion erosion evolve to an intermediate, near-equilibrium state with, in most cases, only two height levels, either with adatom islands or with vacancy islands. From there, they evolve further to their entirely flat, step free, ground state via one or more coarsening mechanisms. The dominant mechanism for this ripening, and with that the appearance of this intermediate state, critically depends on the amount of material removed from the surface by ion erosion [115]. Hoogeman's rough surface was first annealed to a point where most of the height differences in the surface had been removed and the lateral length scales were relatively large. This part of the evolution of surfaces has been observed in great detail on damaged Pt(111) surfaces by Michely et al. [116]. A classification of the different outcomes used by Hoogeman et al. is shown in figure 6.1.

Surface ripening can take place via the dynamic coalescence of mobile clusters of adatoms or surface vacancies, but also via the exchange of individual adatoms or single surface vacancies between clusters. Detailed experimental investigations on Ag(111) of these two surface ripening mechanisms have been performed by Rosenfeld et al. [63]. In a coalescence event, two adatom islands merge by moving close to each other until they coincidentally touch and fuse together. The driving force behind the merging is the lowering of the total energy by reducing the step density (total length of the step per unit surface area). This type of surface ripening is also known as Smoluchowski ripening [68]. Also vacancy islands can merge following this mechanism. In the framework of this chapter, the ripening via the dynamic coalescence of mobile clusters plays a more important role than the second ripening mechanism where adatom islands can exchange individual adatoms via detachment diffusion and re-attachment. Because surfaces lower their total energy when the step density is reduced, larger adatom islands tend to grow, while smaller adatom islands decrease size. This process is called Ostwald ripening [64, 65]. This type of coarsening is driven by the fact that the local density of adatoms, in the direct vicinity of a small adatom island is higher than that close to a large adatom island. The ripening of vacancy islands follows the same mechanism, only in that case single surface vacancies are exchanged.

This is described by the Gibbs-Thomson relation for the surface vacancy density ρ_r in the vicinity of a (circular) vacancy island with radius r , with respect to the

equilibrium density ρ_∞ for an infinitely large island [63]

$$\frac{\rho_r}{\rho_\infty} = e^{\frac{\gamma\Omega}{k_B T r}} \quad (6.1)$$

where γ is the step free energy and Ω is the area per atom. The classical mean field model from [64] predicts that the change in vacancy island surface area A as a function of time t follows

$$\frac{dA}{dt} = -\frac{2\pi\Omega D}{\ln\lambda}(\rho_r - \rho_{eq}) \quad (6.2)$$

where D is the vacancy diffusion constant, λ a screening length over which the exchange of vacancies can still take place and ρ_{eq} the equilibrium vacancy density averaged over all vacancy islands in the ensemble. Equation 6.2 shows that the larger islands in an ensemble grow, while the smaller ones shrink as a function of time

For the kinetics of Ostwald ripening we can identify two limiting cases. In one extreme case, the surface diffusion rate fully limits the rate of vacancy exchange between vacancy islands and the density of surface vacancies decreases as a function of the distance to the nearest vacancy island. In the other extreme, the rate is determined fully by an additional energy barrier for the attachment of a surface vacancy to a vacancy island, and the density of surface vacancies is close to constant [63].

If exactly an integer number of atomic layers is removed from an otherwise perfectly flat surface, these diffusion processes will make the surface evolve to an entirely flat configuration. In all other cases, the deviation from an integer number of monolayers will result in a surface with either adatom islands or vacancy islands.

In this chapter we produced a situation between the configurations shown in figure 6.1b and figure 6.1c. Between 20 and 30 percent of an atomic layer was removed. In this state, a high density of square vacancy islands is present.

In the present study on Cu(100) we find that the distance over which vacancy islands coalesce is significantly more than one lattice spacing. This effect of coalescence over a distance has also been observed for vacancy islands in Ag(111) [66] and in Ni(100), where it was ascribed to the presence of tensile surface stress [115]. Many questions have remained unanswered. For example, why does this effect only occur when two downward steps are close together? Why does the surface not spontaneously ‘rip apart’ elsewhere? Is this behavior different for curved and straight steps?

In this chapter we will consider several possible causes for the rupture of the narrow strip of surface atom layer between two nearby downward steps. Based on the experiment described in section 6.2, and its analysis in sections 6.3 and 6.4, we will compare these scenarios in section 6.5.

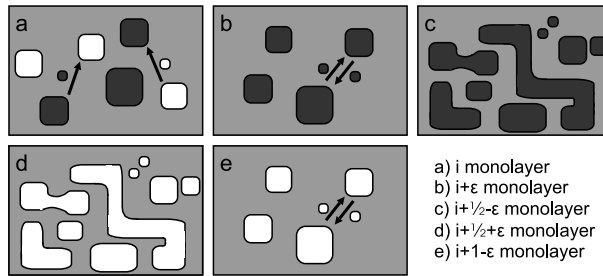


Figure 6.1: Various possible configurations obtained after removing specific amounts of material from a crystal surface. a.) Exactly an integer number of monolayers is removed from the surface. Adatoms diffuse from ad-islands into vacancy islands and, similarly surface vacancies diffuse from vacancy islands to ad-islands, restoring a completely flat surface. b.) Slightly more than an integer number of monolayers is removed, resulting in a low density of vacancy islands, one monolayer deep. The surface ripens by exchange of highly mobile surface vacancies between vacancy islands. Smaller islands decrease in size while larger islands grow. c.) Slightly less than half a monolayer is removed. A high density of vacancy islands is present. The distance between these structures is relatively small. This allows ripening of the surface not only via the exchange of surface vacancies, but also via merging or coalescence of vacancy islands. d.) Slightly more than half a monolayer is removed. A surplus of adatom islands is present. The distance between these structures is relatively small. This allows ripening of the surface not only via the exchange of adatoms, but also via merging or coalescence of adatom islands. e.) Slightly less than an integer number of monolayers is removed, resulting in a low density of adatom islands, one monolayer high. The surface ripens by exchange of highly mobile ad-atoms between these ad-islands. Smaller islands decrease in size while larger islands grow. After [115].

6.2 Experimental procedures

The Cu sample ($4.8 \times 4.8 \times 2.0 \text{ mm}^3$) was cut by spark erosion from a 5N purity single crystal. The crystal was chemically etched and polished parallel to the (100)-plane with an accuracy of 0.1° [90]. After introducing the sample in the UHV chamber with a background pressure of $1 \cdot 10^{-10} \text{ mbar}$, the sample was cleaned by several cycles of ion bombardment of 600 s with 600 eV Ar^+ at a current density of $2.4 \cdot 10^{-3} \text{ A/m}^2$ and annealing at 690 K. This cleaning procedure is similar to the cleaning procedure used earlier for the experiments in chapter 3. An impression of the cleaned surface can be found in figure 3.1.

After cleaning, vacancy islands were created in the Cu(100) surface at $317 \pm 7 \text{ K}$ by a mild ion erosion treatment of 25 s with 600 eV Ar^+ with a current density of $2.0 \cdot 10^{-3} \text{ A/m}^2$. This preparation step removed typically 20-30% of the top monolayer of the surface. The time between this preparation step and the start of the measurement was 1.5 hours. The result of the sample preparation is shown in figure 6.2. The surface of the sample is in a state between those shown schematically in figures 6.1b and c.

Measurements were performed at a temperature of $308 \pm 3 \text{ K}$ with the pro-

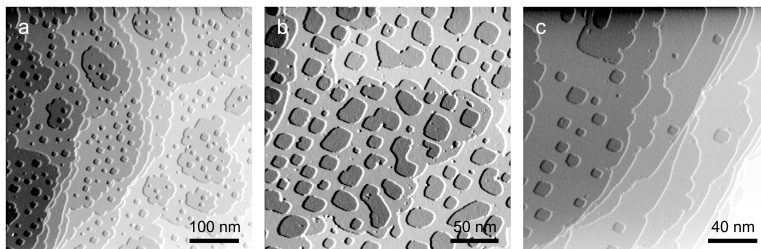


Figure 6.2: *The Cu(100) decorated with vacancy islands of one atomic layer deep. Images are shown on several length scales (see scale bars). To increase contrast, the original and the differentiated height maps are mixed. The additional differential contrast has been chosen to be bright at the locations where the surface steps up from left to right. Tunnel parameters: a.) $V_t = -0.70$ V, $I_t = 0.1$ nA. b.) $V_t = -1.00$ V, $I_t = 0.1$ nA. c.) $V_t = -0.70$ V, $I_t = 0.1$ nA.*

grammable temperature STM described in section 2.2, inside the ultra-high vacuum chamber described in section 2.3.

6.3 Qualitative observations

With the STM areas of typically 200×200 nm² were selected. A surface region of this size looks like the examples shown in figure 6.2. The STM images show terraces, typically 100 nm wide, containing several vacancy islands. The vacancy islands are all one atomic layer deep, but differ in lateral dimensions. The distance between the vacancy islands is such that there is a reasonable probability that vacancy island collisions take place within an observation period of several hours. The experiments spanned between 6.5 and 12 hours of time with images taken continually every 35 to 105 s. Placing the consecutive STM images one after another, one forms a movie, showing the evolution of the surface.

The density of atoms removed from the surface is large enough for the distances between the vacancy islands to be relatively small. The coalescence of vacancy islands shows a remarkable feature. Unlike the coalescence of adatom islands, where the islands only coalesce when they touch [8], vacancy islands only approach down to a particular distance [63, 115]. When the distance between the islands reaches a particular threshold value, the islands suddenly merge. We will refer to such sudden mergers as ‘snap events’. Such a snap event involves rapid or even collective motion of a large number of atoms between the two vacancy islands. Two snap events can be seen in figures 6.3 and 6.4 and one more is shown in figure 6.5. In addition, the shapes of several other vacancy islands in these figures indicates that also they are the result of recent snap events. The events in figures 6.3 and 6.4 illustrate the two extremes of the orientation of the two islands with respect to each other, before the snap event takes place. Figure 6.3 shows snapping via the corners of two vacancy

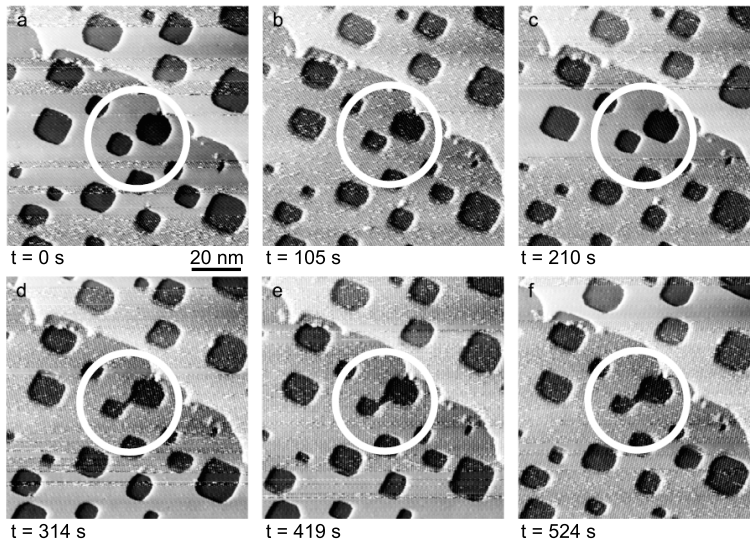


Figure 6.3: Sequence of STM images showing the formation of a narrow channel (‘snapping’) between two vacancy islands via their corners (corner-to-corner event). a.-c.) The surface before the snap event. The vacancy islands slowly diffuse as a whole as a result of random fluctuations in their shape. On the time scale of these STM images the resulting changes in vacancy island position are within one atomic spacing. d.) Within the acquisition time of a single STM image the vacancy islands connect via the formation of a narrow channel between their corners. e.,f.) The early stages of the evolution of the new, joint vacancy island towards its square equilibrium shape. For all images: $V_t = -0.70$ V, $I_t = 0.1$ nA.

islands (corner-to-corner), figure 6.4 shows snapping via the ‘straight sides’ of two vacancy islands (side-to-side).

The characteristic feature of these snap events is the timescale at which they take place. In figures 6.3a-c and 6.4a-c two pairs of vacancy islands that are about to snap are indicated. The islands are separated by a narrow strip of remaining surface layer, with a width of a few nm. The vacancy islands diffuse as a whole through the surface, but the mobility of the clusters at this temperature is such that the timescale for the marked islands to traverse the small, remaining distance between them would still be in the order of tens of minutes or more. Note that the distance between the two islands in figure 6.4c, just before snapping side-to-side, is smaller than the distance between the two islands in figure 6.3c, just before snapping corner-to-corner. Figures 6.3d and 6.4d show that a channel has formed between the two highlighted vacancy islands. These events happen on a timescale of at most a few seconds, at least two orders of magnitude faster than a ‘collision’ due to regular vacancy island diffusion would take. Figures 6.3e,f and 6.4e,f show the early stages of the relaxation of the two newly formed vacancy island towards the equilibrium shape of vacancy islands in Cu(100). The evolution of merged islands has been

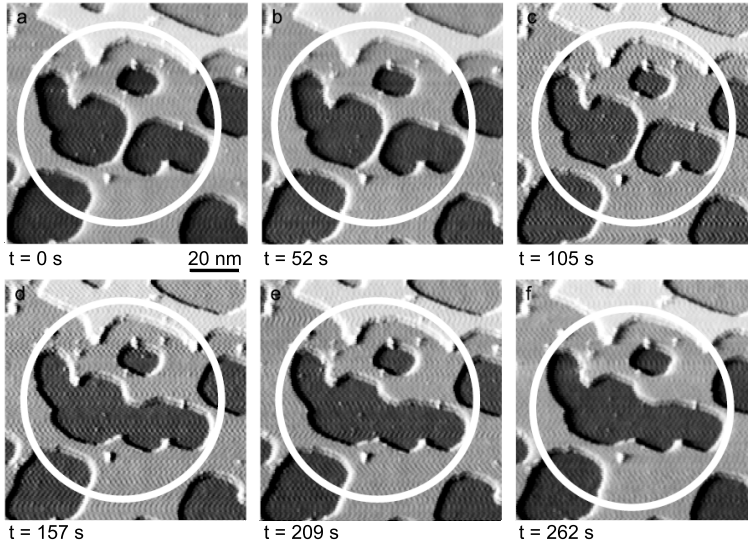


Figure 6.4: Sequence of STM images showing the merger of two vacancy islands via the straight sides (side-to-side event). *a.-c.)* The surface before the snap event. Note that the distance between the highlighted islands in (c), just before snapping is smaller than the distance just before the corner-to-corner snap event shown in figure 6.3c. *d.)* Within the acquisition time of one frame the vacancy islands merge together via the sides. *e.,f.)* The early stages of the evolution of the joint vacancy island towards its square equilibrium shape. For all images: $V_t = -0.70$ V, $I_t = 0.1$ nA.

investigated earlier in [8, 63, 117] and will not be discussed here.

In one experiment we elevated temperature to a higher level. This experiment shows examples of Ostwald ripening in this surface. Several examples where small islands are followed until they disappear, are indicated with circles in figure 6.5.

In the next section, the snap events will be quantitatively described. We will see that the difference in snapping distance between side-to-side and corner-to-corner encounters observed in this section, is systematic. We will also see that the vacancy islands change their shape somewhat before snapping. The conclusions drawn from the observations of this section and the quantitative analysis in section 6.4, will be further discussed in the concluding section 6.5.

6.4 Quantitative analysis

The measured series of STM images have been subjected to image analysis, by the use of appropriate software filters to find the precise locations of island boundaries and step edges. The software filter sequence is described in the Appendix A (section A3). With these results, various parameters have been determined, such as the distances between neighboring vacancy islands, the orientation of the two islands

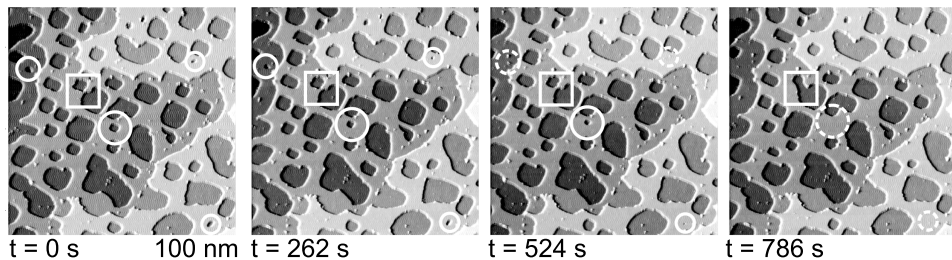


Figure 6.5: Sequence of STM images showing the two ripening mechanisms, simultaneously active for vacancy islands in Cu(100) at $T = 350$ K. The circled islands all disappear slowly by exchanging single vacancies with their larger neighbors (Ostwald ripening). The dashed circles indicate the position of disappeared islands. The islands indicated by the squares increase their size by coalescing (Smoluchowski ripening). For all images: $V_t = -0.70$ V, $I_t = 0.1$ nA.

with respect to each other and the internal dimensions (shape) of each island. The definition of the measured dimensions is shown in figure 6.6. The distance between the edges of two neighboring islands is d , while α denotes the orientation of the two neighboring islands with respect to each other. The lengths of the diagonals of each individual vacancy island are referred to as d_{\perp} and d_{\parallel} . Our distance and orientation measurements were exclusively performed on nearest-neighbor vacancy island pairs.

The difference in timescales between the diffusive motion of vacancy islands, and the snapping events is evident in figure 6.7, which shows the edge-to-edge distance d as a function of time for two vacancy island pairs. In both cases (figure 6.7a and b) the two vacancy islands slowly approach each other, at a speed in the order of 3 nm/h. Superimposed on this slow approach are random fluctuations in the distance due to position and shape fluctuations of the individual islands. These distance fluctuations are limited to ± 0.5 nm and have a characteristic time scale of a few minutes at this temperature. In both examples in figure 6.7 the two islands suddenly snap together after 20 to 25 minutes, when the edge-to-edge distance has decreased to some 2.5 nm. From figure 6.7, it becomes clear that the snap event takes place at a very short timescale, two orders of magnitude faster than the time scale of 1 hour or more, expected from the extrapolated vacancy island diffusion behavior of the first 20 minutes. In none of the 26 observed snap events have we been able to image the snapping vacancy island in an intermediate configuration, i.e. during the formation of the first contact. This implies that the time scale for the actual snap process must be well below the acquisition time of the STM images of roughly 1 minute.

Not all vacancy island pairs were observed to snap at the same distance. The distribution of measured snap distances, defined as the edge-to-edge distance d in the last STM image before the snap event, is shown in figure 6.8a. The distribution

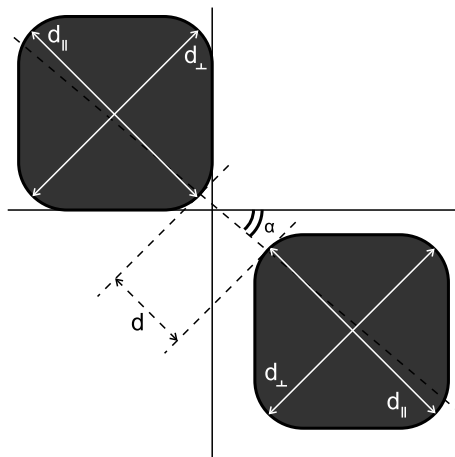


Figure 6.6: Definition of the measured dimensions of two neighboring vacancy islands. The equilibrium shape of the vacancy islands resembles a square with rounded corners. For the true shape of 2-dimensional islands in Cu(100) we refer to work by Giesen et al. [14]. The distance d is the shortest distance between the vacancy islands. The angle α indicates the orientation of this shortest connection. The deviation of the island shape from rectangular is investigated by measuring the lengths of the island's diagonals. The diagonal pointing in the direction of the other island is called $d_{||}$, the diagonal pointing perpendicular to the direction of the other island is called d_{\perp} .

runs from a minimum snap distance of $1.2 \pm 0.3 \text{ nm}$ to a maximum distance of $5.3 \pm 0.9 \text{ nm}$. Most snap events occurred at a distances between 2 nm and 4 nm .

In addition to the distances at which snap events occur, we have measured the relative orientation angle α of vacancy island pairs, in the last STM image before they snapped. The α -distribution is plotted in figure 6.8b. Most snap events occur between $\alpha = 30^\circ$ and $\alpha = 45^\circ$. Interestingly, the two distributions in figures 6.8a and 6.8b are correlated, i.e. there is a relation between the snap angle and the snap distance. This correlation becomes visible if we combine the two distributions in the form of the polar plot in figure 6.9. The average distance for corner-to corner events ($\alpha = 42^\circ \pm 6^\circ$) is $3.3 \pm 0.5 \text{ nm}$, while the average snap distance for side-to-side events ($\alpha = 0^\circ \pm 4^\circ$) is distinctly smaller, namely $2.3 \pm 0.4 \text{ nm}$. The average distance for snap events of island pairs that have an intermediate orientation in the range of 10 to 40 degrees (on average $31.8^\circ \pm 6^\circ$) is $3.0 \pm 0.5 \text{ nm}$.

Our STM observations contain several strong indications of a significant attractive force between neighboring vacancy islands. We have already seen two examples (figure 6.7) that the distance between neighboring vacancy islands decreases with time. This seems to be a general trend for all vacancy island pairs at close distance. The second indication for attractive interaction between vacancy islands is that they change their shape when they are in each other's vicinity. This is illustrated by figure 6.10, which shows how two vacancy islands changed their shape

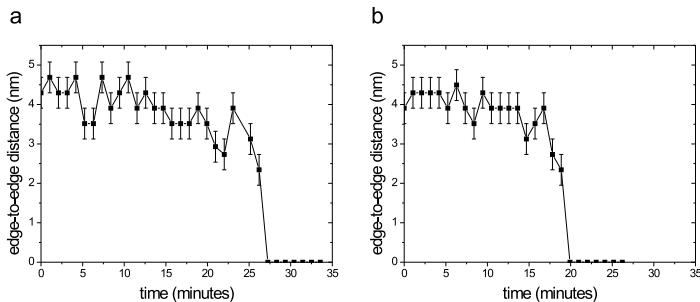


Figure 6.7: *The shortest edge-to-edge distance d for two pairs of islands as a function of time. In both cases we observe a slow, decreasing trend in the distance, on which distance fluctuations are superimposed with an amplitude in the order of 0.5 nm . For both island pairs we observe a sudden merger from a distance in the order of 2.5 nm .*

as a function of their distance d . The increase in the relative elongation R as the neighboring vacancy islands approached each other shows how much they deviated from their original, symmetric shape. The parameter R is defined as $R = 2 \frac{d_{\parallel} - d_{\perp}}{d_{\parallel} + d_{\perp}}$. The two islands of figure 6.10 were both approximately $11 \times 11 \text{ nm}^2$ in size and they were orientated corner-to-corner. When the distance between the islands was $4\text{-}5 \text{ nm}$ or larger, the shape of the islands was more or less square ($R \approx 0$). We observed an increase in R for *both* vacancy islands as the distance between the island decreased. This means that the two islands elongated simultaneously along the mutual d_{\parallel} -direction. This is the direction connecting the two islands. At a distance of 2.4 nm between the two vacancy islands, the change in R corresponded to an elongation of about 2 lattice spacings (0.5 nm) in the parallel direction and a narrowing of 2 lattice spacings in the perpendicular direction. This elongation of the vacancy islands announces an imminent snap event. In section 6.5.5 this effect will be discussed further.

In the next concluding section, the findings of this section and the observation of section 6.3 will be used to find an explanation for the snap events that result in the coalescence of vacancy islands.

6.5 Discussion and conclusion

The coalescence of vacancy islands involves the approach of two vacancy islands, and a snap event where a corridor is formed between the two vacancy islands. Reports in literature show that this surprising behavior is not observed in the coalescence event of adatom islands [8].

The qualitative observations in section 6.3 show that there is a sudden transport

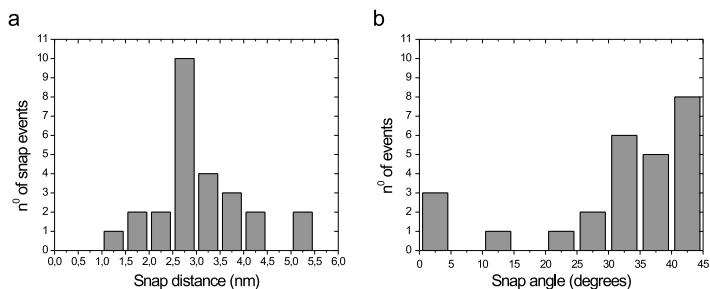


Figure 6.8: a.) Distribution of the snap distance i.e. the minimum value of the shortest distance d between neighboring vacancy islands, from which they snapped. The distribution ranges from 1.2 ± 0.3 nm to 5.3 ± 0.9 nm. Most snap events take place at distances between 2 nm and 4 nm. b.) Distribution of snap angles. The distribution shows a clear preference for snapping in the diagonal direction, i.e. for angles around 45° .

of atoms away from the strip of surface between two vacancy islands, resulting in the formation of a corridor between neighboring vacancy islands well before the edges of the two vacancy islands would be expected to touch for the first time due to island motion and edge fluctuations. The timescale at which the snap event takes place, is much smaller than the timescales at which the vacancy islands diffuse towards each other. This indicates that for the formation of this channel between the vacancy islands, a mechanism different from random diffusion is at work.

Quantitative observations, where the distance between two neighboring islands is followed in time confirm that the snap event takes place within one minute, while in the 20 minutes before, the distance between the two neighboring islands had changed only by a modest amount.

The snap distance distribution in figure 6.8a shows that most of the snap events occur when the distance between neighboring vacancy islands is around 3 nm. When also the angle α between the coalescing islands is considered, as has been done in the polar plot in figure 6.9, it becomes clear that there is a difference between coalescence side-to-side, and coalescence corner-to-corner. Most snapping events occurred when islands were under a non-zero angle with respect to each other. It was observed that when the vacancy islands were not exactly aligned corner-to-corner, or even in the case where the vacancy islands were aligned side-to-side, but one of the vacancy islands was considerably smaller, the connection was formed between the corner of one of the islands and the side of the other island. True corner-to-corner events were rare because the probability to find two vacancy islands exactly oriented corner-to-corner was lower than that to find a pair at a somewhat different orientation. Snap events that occurred side-to-side were even more rare because apart from the precise alignment, the islands also need to be roughly the same size

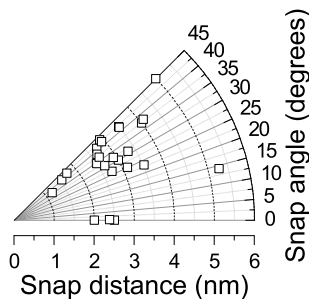


Figure 6.9: Polar plot of the distances and the corresponding angles at which the snap events have been observed to take place. Most events take place at non-zero angle. The probability for vacancy islands to coalesce side-to-side is low because the islands should be aligned exactly side-to-side and have equally long sides facing each other. The probability that both conditions are fulfilled is low. The most probable orientations at which vacancy islands coalesce are between 25° and 45° , the intermediate orientations. In most of these intermediate cases the snap event took place between the corner of one island and the side of the other island. Notice that although there is considerable scatter in the snap distances, the snap distance is on average somewhat shorter at 0° (side-to-side) than at 45° (corner-to-corner).

to prevent the corner of the smaller island to act as the site where the snap event took place.

The other striking effect, which was observed just before corner-to-corner snap events was that the vacancy islands were elongating towards each other. The magnitude of the deformation indicates that the elongation is not a mere lattice deformation, but rather a change in the equilibrium shape for vacancy islands that are in each other's proximity.

Five possible mechanism and driving forces are considered as potential causes for the snapping events; accelerated Ostwald ripening by the increasing exchange of vacancies, step fluctuations, chain formation of surface vacancies, step interactions, and surface stress. In the rest of this section, these five mechanisms are discussed and compared with the observations of sections 6.3 and 6.4 and observations taken from the literature.

6.5.1 Accelerated Ostwald ripening

The first mechanism that we consider as a potential cause for the observed snap events is accelerated Ostwald ripening. As islands approach, the probability that a single surface vacancy, detached from one of the two islands reaches the other island increases strongly. This leads to an increase in the rate at which Ostwald ripening between two nearby islands takes place. A similar mechanism has been observed for Ni(100) by Hoogeman, et al. [115]. They showed that enhanced Ostwald ripening gives rise to anomalously rapid decay of vacancy islands. The ripening tends to

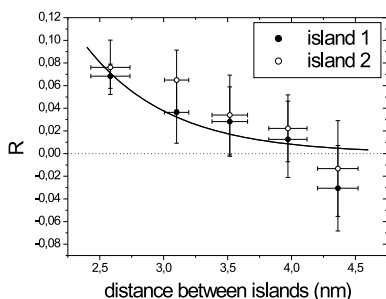


Figure 6.10: Vacancy island elongation measured for two neighboring vacancy islands versus the edge-to-edge distance, d , between the islands. The vacancy islands had approximately the same size ($11 \times 11 \text{ nm}^2$) and were oriented under an angle $\alpha = 37^\circ$ (corner-to-corner). The elongation parameter R is defined as $R = 2 \frac{d_{\parallel} - d_{\perp}}{d_{\parallel} + d_{\perp}}$. The islands did not coalesce during the measurement. The solid curve serves to guide the eye. R becomes larger for both islands as the distance d between the islands becomes smaller. This shows that as the islands approach each other, they elongate in the direction towards each other. When the distance between the two neighboring islands is large, the value of R should approach zero (dotted line).

make the smaller island become smaller and the larger island larger. The net effect is to make the distance between the two vacancy islands increase, which, in turn, lowers the rate of vacancy exchange. Ostwald ripening thus definitely does not lead to an accelerated reduction of the distance between the islands and thus to a rapid merger.

6.5.2 Step fluctuations

The second phenomenon that we consider as a possible cause for the rapid snapping are step fluctuations. Figure 6.7 shows the effect of such fluctuations in step position on the distance between two neighboring vacancy islands. Superimposed on the slow drift in island separation are variations of at most $\pm 0.5 \text{ nm}$ on a characteristic time scale of 1.7 minutes. By contrast, most snap events occur when the edge distance between vacancy islands is 2-3 nm, which is well outside of the window of step fluctuation amplitudes. This rules out step fluctuations to be solely responsible for the snapping of vacancy islands. However, in combination with another mechanism, which should operate over a large distance, the step fluctuations could still play the role of ‘trigger’ for the snapping.

6.5.3 Spontaneous clustering of surface vacancies

The third scenario that we consider involves a possible self-organization of surface vacancies. When individual surface vacancies would cluster between two neighboring vacancy islands, this might lead naturally to the formation of a ‘channel’ between these islands. The difference in average distance between vacancy islands snapping corner-to-corner and side-to-side might then be a kinetic effect, caused by a corresponding difference in the activation energy for the creation of vacancies at kinks and at straight steps. As the kink density at island corners is higher, more vacancies may be expected to be created in the corner regions of vacancy islands.

There are several arguments against a scenario involving local enhancements of the concentration of surface vacancies. First of all, one would expect this scenario to be equally applicable to the generation of adatoms at the corners of adatom islands, which would make it difficult to explain why the snapping at a distance is observed only for vacancy islands and not for adatom islands [8]. An important second argument is that at room temperature, the density of vacancy islands is low, approximately 1 in 10^9 atoms is missing. Even when the density could be enhanced locally by an appreciable factor, as a result of the local generation of the surface vacancies, it seems highly unlikely that this would result in significant vacancy densities between neighboring vacancy islands. A third argument against this type of explanation is that even though vacancies might be formed and annihilated only at specific locations, in particular in the corner regions, this has no influence on the equilibrium density distributions of the vacancies. In other words, such a kinetic preference for vacancy creation and annihilation near the corners in itself would not serve as a thermodynamic basis for a local enhancement of the vacancy density between the corners of two nearby vacancy islands.

6.5.4 Step interactions

A possible driving force behind snap events might be step interactions [118, 119]. Surface defects, in particular steps, can interact in various ways. Charge redistribution at a step will result in an electrostatic dipole moment and the dipoles on different steps will interact. In addition, each step is dressed by a configuration of elastic lattice distortions of which the amplitude decays as a function of the distance to the step [120, 121, 122]. When two steps are in each others vicinity, these distortion patterns tend to frustrate each other, naturally leading to an increase in the total energy and thus a repulsive interaction between the steps. Also this has the formal appearance of a dipole-dipole interaction. Finally, at finite temperatures, meandering steps will experience an additional repulsion on thermodynamic grounds, as the impossibility for the steps to cross each other reduces the total number of allowed configurations for each individual step and therefore increases the step free energy [123]. At room temperature, the first two sources of step interaction domi-

nate and the interaction energy falls off as A/L^2 , where L is the distance between the steps (expressed in atomic spacings). For steps on Cu(100), the constant A has been determined to be 3 meV per interatomic spacing along the steps, based on the analysis of terrace width distributions, measured by Giesen et al. in STM images [124]. In our experiment, however, the vacancy islands were observed to snap over relatively large distances of typically 10 lattice spacings. At this large distance, the reduction in step interaction energy is thus as small as 0.03 meV per lattice spacing. On the other hand, the step formation energy on Cu(100) is as high as 169 meV per lattice spacing [125]. Thus the step formation energy on Cu(100) is more than three orders of magnitude higher than the reduction in the step interaction energy at the distance between the vacancy islands before they snap and can safely be ruled out as the main driving force for the snapping of vacancy islands.

6.5.5 Surface Stress

Atoms at the (100) surface of a copper crystal do not have the same number of neighbors as they would have in the bulk of the crystal, namely 8 instead of 12. Although the surface responds to this by relaxations of the surface and near-surface interlayer distances, this undercoordination still puts the entire surface under tensile stress [2, 126]. Steps are locations in the surface where stress relaxation can take place. In particular, at the upper side of a step the interatomic spacings in the direction parallel to the surface and perpendicular to the step may be compressed slightly with respect to the regular, bulk interatomic spacing. In section 3.4.3 it was proposed that this stress relaxation might be the cause of the observed decrease in diffusion barrier for surface vacancies at the upper terrace, close to a step.

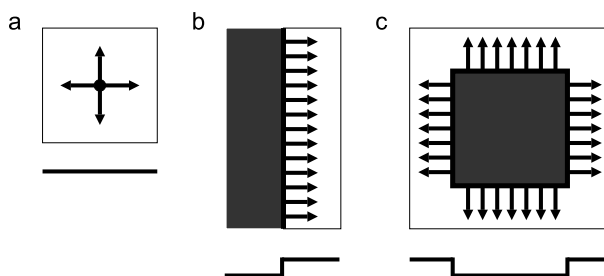


Figure 6.11: *Surface stress and stress relaxation for various structures in the surface. a.) Inside a terrace, the symmetric stress does not lead to atomic displacements. b.) At steps, the symmetry is broken and atoms can relax sideways in response to the surface stress. Most of this relaxation will take place in the upper terrace, where the lattice of the upper terrace in the vicinity of the step edge is slightly compressed in the direction perpendicular to the step edge. c.) Stress relaxation takes place in a similar way at the boundaries of a vacancy island. As indicated by the arrows, stress relaxation takes place in the upper terrace in all directions away from the center of the vacancy island.*

Cartoon images in figure 6.11 show the direction of stress relaxation at steps. In a large, defect free terrace, atoms are surrounded on all sides by neighbors. This situation is shown in figure 6.11a. Due to the symmetry of this configuration, no stress relaxation can take place. At the location of a step the balance of surface stress is disrupted. As a response the lattice of the upper terrace in the vicinity of a step edge is slightly compressed in the direction perpendicular to the step edge. In this way the tensile stress in Cu(100) is locally relaxed (figure 6.11b). This effect also takes place in the first few atomic spacings inside adatom islands and, similarly, in the first few spacings outside vacancy islands (figure 6.11c). However, the suggested stress relaxation by a receding step introduces a problem at curved steps, particularly at the corners of adatom and vacancy islands where the step curves over an angle of 90° . The problem is visualized on an exaggerated scale for a vacancy island in figure 6.12. The atoms at the straight sections of the step move in the direction

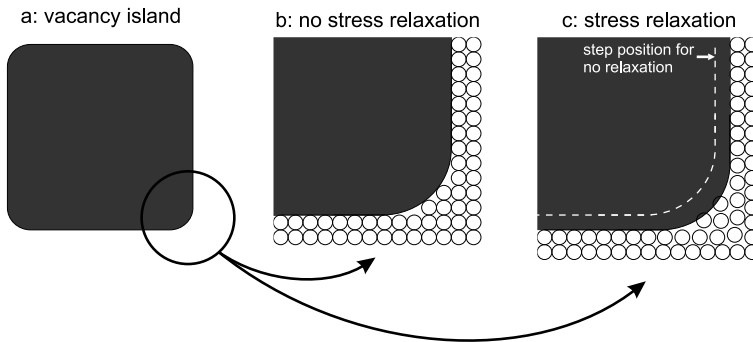


Figure 6.12: Exaggerated, schematic view of the frustration of stress relaxation in the upper terrace close to vacancy island corners. a.) a cartoon image of a vacancy island. b.) Magnification of one of the vacancy island corners in the case of absence of stress relaxation. The circles are the atoms in the upper terrace. c.) Effect of stress relaxation in the vicinity of the corner. Although the relaxation along the sides of the island make the lattice in the upper terrace, close to the step, slightly more compact, this relaxation tends to make the lattice close to the corners slightly less compact.

perpendicular to the step edge, into the upper terrace. In this translation, the lattice spacing parallel to the step edge does not change. This makes that the area of the vacancy island is slightly larger than in the absence of stress relaxation. Since the number of step atoms does not change this implies that the interatomic spacing for atoms at the corner regions of a vacancy island must be stretched parallel to the step edge. We see that the relaxation of the stress along the straight sections naturally leads to an *increase* in the stress near the corners. Similarly, the corners of adatom islands might also introduce a frustration of the stress relaxation, since there the combined relaxations from the straight sections may tend to overcompensate the stress.

When two vacancy islands are placed with their corners close to each other, the strains and stresses of the two islands in the direction parallel to the two corner edges will add up. We speculate that it is this effect that eventually leads to a mechanical instability, where the narrow, residual strip of first-layer material between the two vacancy islands is no longer stable against fluctuations in the positions of the two edges. This will lead to rapid removal of atoms out of this region and fusion of the two vacancy islands.

For vacancy islands approaching side-to-side, the situation is somewhat different. Naively one would expect that in this case there would be no special tendency for the islands to snap together from a distance, because there are no curved steps and thus no strain fields parallel to the step direction. However, at finite temperatures, such as room temperature, the steps fluctuate in shape and position [7, 14], as is illustrated by the distance fluctuations in figure 6.7. These step fluctuations superimpose temporarily curved sections on the equilibrium shape including the ‘straight’ sections. These curved regions are necessarily accompanied by strain fields, as before, mostly concentrated in the upper terrace. This situation is drawn schematically in figure 6.13. Because the typical curvature involved in these fluctuations is much smaller than that at the corners of vacancy islands, the associated strain fields are much smaller. For these two reasons, we expect that two vacancy islands oriented side-to-side can approach to a closer distance than vacancy islands oriented corner-to-corner before they snap together. Step fluctuations occur randomly both in space and time. Therefore, we expect that vacancy islands that approach each other side-to-side display a wider statistical variation in snap distances than corner-to-corner pairs, which should include much shorter distances. Unfortunately, side-to-side events are rare because both vacancy islands should be exactly aligned and the step length of the opposing steps should be the same. Although the side-to-side snap distances in figure 6.9 are indeed somewhat smaller than the average snap distance for corner-to-corner events, the small number of side-to-side events in our data does not allow us to draw conclusions on the statistical variation and on the minimal snap distance for these events. In the more frequently occurring intermediate case, where the corner of one vacancy island is close to a straight section of the other vacancy island, the average distance at which the snap event takes place is found to be between the average side-to-side and corner-to-corner snap distances.

For adatom islands, the lattice deformation caused by the stress relaxation leads to a compression of the island. In the adatom islands case, stress relaxation would not promote, but rather counteract island snapping.

The elongation of the islands towards each other, shown in figure 6.10, also fits into the picture of island snapping promoted by a locally strained surface. The enhancement of the local strain when two islands meet corner-to-corner will indeed be in favor of the observed elongation, since this will reduce the area of the unfavorably strained region between the two vacancy islands and thus tend to lower the

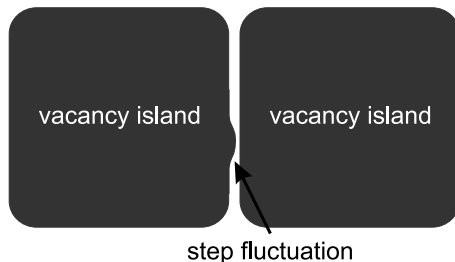


Figure 6.13: Schematic image of an exaggerated step fluctuations that might induce a snap event between the straight steps of a pair of side-to-side oriented islands. The strain field associated with this curved step triggers the snap event.

energy somewhat. For the corner-to-corner pairs of vacancy islands in Cu(100), we observe that the equilibrium shape changes from a rounded square to a (rounded) diamond.

The maximum elongation of the vacancy island was observed when the distance between two corner-to-corner oriented islands was 2.4 nm . At that point, for both islands, the ratio $\frac{d_{\parallel}}{d_{\perp}}$ was 1.07. Both islands had roughly the same size, $11 \times 11 \text{ nm}^2$. It is easy to show that, even though the enclosed area remains constant, the elongation has hardly any effect on the length of the straight sections of the vacancy island (increase by only 0.05 lattice spacings), but the elongation of the island causes the introduction of 2 extra kinks in each straight step. The kink formation energy has been determined by Giesen et al. to be $128 \pm 3 \text{ meV}$ [14, 51, 127]. The total energy involved in the excess kink formation due to the elongation of islands is 1.0 eV per island. Clearly, the reduction of the width of the remaining region between the two vacancy islands by approximately 4 interatomic spacings has lowered the total strain energy sufficiently to justify the 2.0 eV energy ‘investment’ in the elongation of the two structures. The step formation energy is 680 meV/nm (EAM calculations [125]). The total amount of step formation energy involved in the formation of a channel between the two vacancy islands at $d = 2.4 \text{ nm}$ is 3.3 eV (two steps are formed). This energy is in the same order of magnitude as the energy already ‘invested’ in the shape change of the two islands.

In this chapter we have shown that vacancy islands merge before their boundaries touch. We suggest that the explanation of these premature mergers can be found in local strain fields near curved steps.

Appendix

A Image processing

In this appendix, the sequence of software filters is briefly described, that was used for processing the data in chapter 3 and chapter 6. Only the filter sequences are discussed. Details on the software filters themselves can be found in the references cited. In the first section, the filter sequence is shown that enabled the objective determination of the position of indium atoms inside and outside a vacancy island. This filter sequence was used for the data in chapter 3. Section A2 describes a filter sequence to correct for thermal drift. In the third section, the filter sequence is shown, that was used to determine the shapes and positions of vacancy islands, as well as the distances between them. This filter sequence was used to process the data in chapter 6.

A1 Indium recognition

The first filter sequence that was used to find incorporated indium atoms is schematically indicated in figure A1. Four inputs are required to find the indium atoms: the raw STM images, the average size and shape of an indium atom, a threshold value for the detection of steps and a threshold value for the detection of incorporated indium atoms. The raw STM data is first filtered with a planar background subtraction [128] to remove the slope and offset in the STM data. The result is convoluted [128] with the average indium atom by cross correlation [128, 129]. Compared to incorporated indium atoms, steps have a similar shape but a much larger height. That is why steps stand out in the convolution image. The steps are filtered out by taking the local derivative [128] of the background subtracted image and replacing pixels with values, larger than the step detection threshold, with zero and pixels with a lower value with one. The convolution image is multiplied by this step removal image. Noise is reduced by applying an erosion and a dilation filter [128, 130]. These operations move the maxima in the image from their original positions. To circumvent this effect, the indium atom sized areas with values larger than the indium atom detection threshold were set to one, the rest of the image was set to zero. The resulting image was multiplied with the original convolution image. The

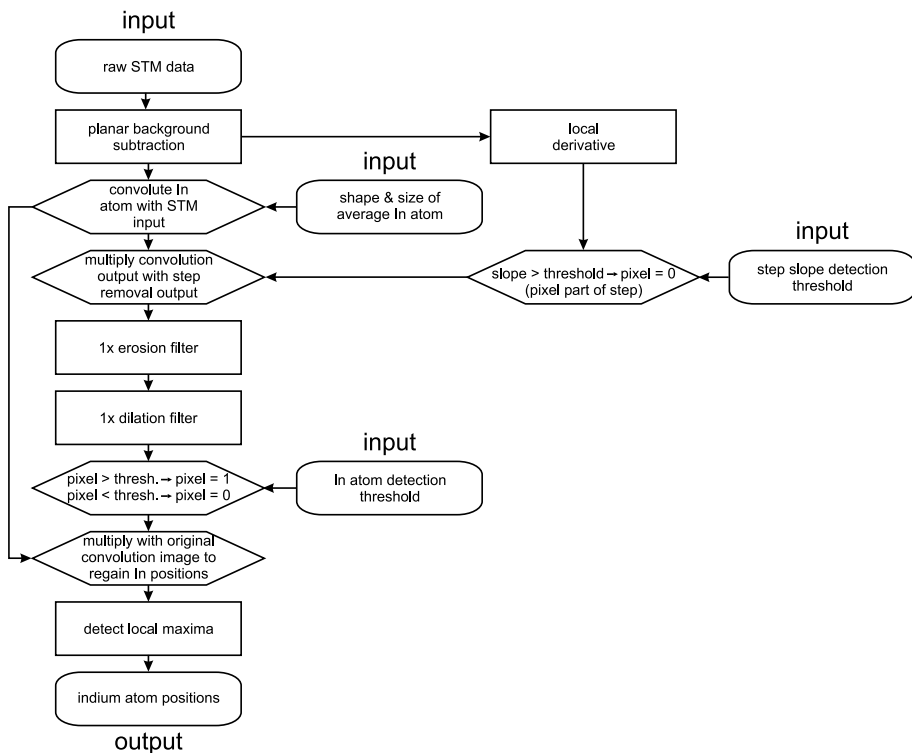


Figure A1: Filter sequence for detection of indium atoms inside and outside a vacancy island.

maxima in the resulting image are the coordinates of incorporated indium atoms. These coordinates are the output of the filter. This filter sequence was used to detect incorporated indium atoms in chapter 3.

The second method to detect indium atoms also uses the raw STM images and the shape and size of the average indium atom. This method is schematically indicated in figure A2. The raw STM images are background subtracted [128]. In this filter, in stead of directly finding sites where indium atoms convolute best, the images are searched for specific features, unique to indium atoms. This avoids the usage of "external" thresholds. The features of interest are the shape and size of the first and second derivative of an average incorporated indium atom. From both input images, the local first and second derivative are taken [128]. For each pixel in the differentiated STM data, the local surroundings are compared to the first derivative of the average indium atom. The same treatment is performed for the second derivative. Only the areas are selected, where the first and second derivative of the STM data both are similar to the first and second derivative of an indium atom. The center of these areas are the coordinates of the incorporated indium atoms.

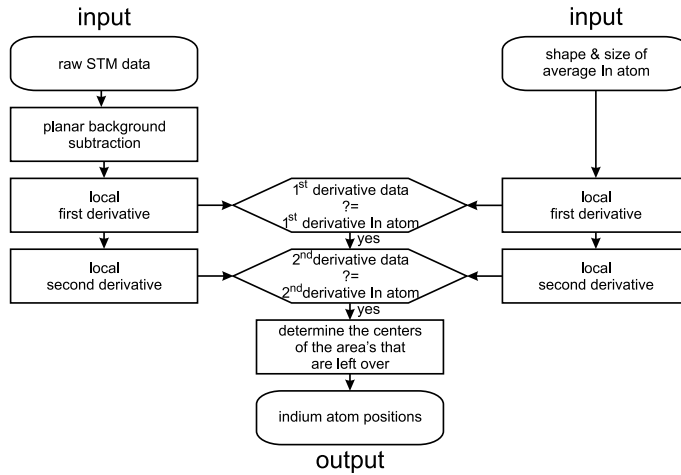


Figure A2: Filter sequence for detection of indium atoms inside and outside a vacancy island.

A2 Drift correction

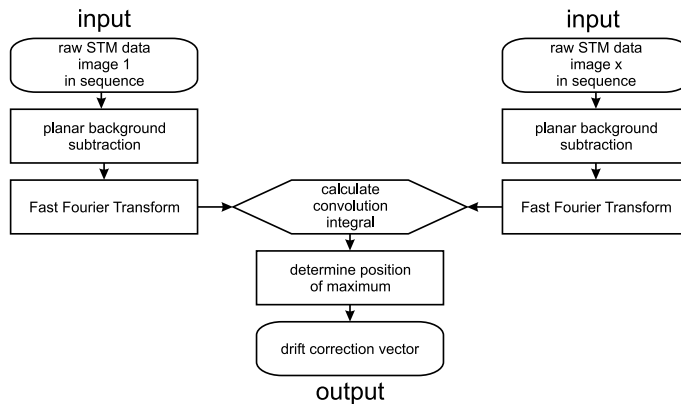


Figure A3: Filter sequence for the determination of the motion caused by thermal drift.

Although the programmable temperature STM used in this thesis is thermally stable, thermal drift between images is unavoidable. Some of the thermal drift is filtered out manually during the measurement by changing the offset voltages on the scan piezo in the lateral directions. Apart from this coarse drift correction, software filters are still necessary to compensate the thermal drift completely. The filter sequence used to correct the thermal drift vector between images is based on the determination of the convolution integral between entire images [128]. A schematic of this sequence is shown in figure A3. The convolution image is built

by multiplying the Fast Fourier Transformations [128, 129] of the first image of a sequence and image x of the same sequence. The vector starting at the position of the maximum of the convolution image and ending at the nearest corners of this image, is the correction vector for the displacement between images 1 and x due to thermal drift.

A3 Vacancy island detection

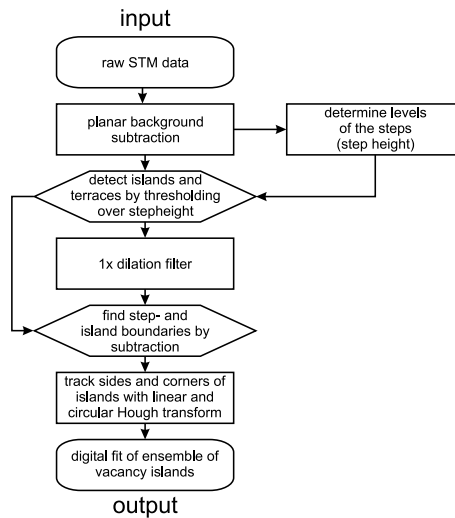


Figure A4: Filter sequence for the digital fit to vacancy islands. From the digital fit, the parameters island separation distance d , orientation angle α , and the internal dimensions d_{\parallel} and d_{\perp} , used in chapter 6 can be determined.

The filter sequence for detecting vacancy islands is shown in figure A4. It starts with a planar background subtraction from the raw STM image. To avoid residual slopes, caused by the uneven distribution of terraces, the most common slopes in x - and y -direction were determined with a slope distribution from the differentiated image. This tilted plane is subtracted from the raw data. The average height offset of the resulting image is determined and subtracted. These two operations produce the planar background subtracted image. The levels of the terraces are determined by making a pixel value distribution of the planar background subtracted image. The heights of structures on the surface are mostly integer numbers of step heights. Thus, the peaks in the pixel value distribution are the terrace levels. These levels are used as a threshold for locating the terraces and the vacancy islands inside them. Applying a dilation filter [128, 130], one slightly shrinks the islands. The boundaries of the vacancy islands are found by subtracting the dilation filtered image from the image with the located vacancy islands. Terrace ledges are found the same way,

by considering the terraces as very large islands. The position and orientation of island sides, and the shape and position of island corners are determined with respectively the linear and the circular Hough transformation [128, 131, 132]. This results in a digital fit of the ensemble of vacancy islands present in the STM image. These fits enable the determination of the island separation distance d , orientation angle α , and the internal dimensions d_{\parallel} and d_{\perp} , used in chapter 6.

Bibliography

- [1] H.L. Davis, J.R. Noonan, *J. Vac. Sci. Technol.* **20**, 842 (1982)
- [2] R.C. Cammarata, *Progr. Surf. Sci.* **46**, 1 (1994)
- [3] W. Kossel, *Nachr. Ges. Wiss. Göttingen*, 135 (1927)
- [4] I.N. Stranski, *Z. Phys. Chem.* **136**, 259 (1928)
- [5] F. Besenbacher, *Rep. Prog. Phys.* **59**, 1737 (1996)
- [6] K. Morgenstern, *Phys. Stat. Sol. (B)* **242**, 773 (2005)
- [7] L. Kuipers, M.S. Hoogeman, J.W.M. Frenken, *Phys. Rev. Lett.* **71**, 3517 (1993)
- [8] W.W. Pai, A. K. Swan, et al., *Phys. Rev. Lett.* **79**, 3210 (1997)
- [9] R.G. Parr, Y. Weitao, *Density-functional Theory of Atoms and Molecules* (Oxford University Press Inc., New York, 1995)
- [10] M.S. Daw, M.I. Baskes, *Phys. Rev. B* **29**, 6443 (1984)
- [11] S.M. Foiles, M.I. Baskes, M.S. Daw, *Phys. Rev. B* **33**, 7983 (1986)
- [12] M. Finnis, J. Sinclair, *Philos. Mag. A* **50**, 45 (1984)
- [13] P. Stolze, *J. Phys. Condens. Matter* **6**, 9495 (1994)
- [14] M. Giesen, C. Steimer, H. Ibach, *Surf. Sci.* **471**, 80 (2001)
- [15] G.S. Bales, A. Zangwill, *Phys. Rev. B* **41**, 5500 (1990)
- [16] N. Néel, T. Maroutian, et al., *Phys. Rev. Lett.* **91**, 226103 (2003)
- [17] G. Ehrlich, F.G. Hudde, *J. Chem. Phys.* **44**, 1039 (1966)
- [18] R.L. Schwoebel, E.J. Shipsey, *J. of Appl. Phys.* **37**, 3682 (1966)
- [19] R.L. Schwoebel, *J. Appl. Phys.* **40**, 614 (1969)
- [20] M. Copel, M.C. Reuter, et al., *Phys. Rev. Lett.* **63**, 632 (1989)
- [21] R. M. Tromp, M.C. Reuter, *Phys. Rev. Lett.* **68**, 954 (1992)
- [22] D.J. Eaglesham, F.C. Unterwald, D.C. Jacobson, *Phys. Rev. Lett.* **70**, 966 (1993)
- [23] H.J. Osten, J. Klatt, et al., *J. Appl Phys.* **74**, 2507 (1993)
- [24] K. Schroeder, A. Antons, et al., *Phys. Rev. Lett.* **88**, 046101 (2002)
- [25] A. Hirnet, K. Schroeder, et al., *Phys. Rev. Lett.* **88**, 226102 (2002)
- [26] A. Antons, K. Schroeder, et al., *Phys. Rev. Lett.* **89**, 236101 (2002)

- [27] Th. Schmidt, R. Kröger, et al., Phys. Rev. Lett. **96**, 066101 (2006)
- [28] J. Camarero, J. Ferrón, et al., Phys. Rev. Lett. **81**, 850 (1988)
- [29] H.A. van der Vegt, H.M. van Pinxteren, et al., Phys. Rev. Lett. **68**, 3335 (1992)
- [30] S. Esch, M. Hohage, et al., Phys. Rev. Lett. **72**, 518 (1994)
- [31] H.A. van der Vegt, M. Breeman, et al., Phys. Rev. B **51**, 14806 (1995)
- [32] H.A. van der Vegt, W.J. Huisman, et al., Surf. Sci. **330**, 101 (1995)
- [33] H.A. van der Vegt, Ph.D. thesis, Universiteit van Amsterdam (1995)
- [34] B. Poelsema, R. Kunkel, et al., Appl. Phys. A **53**, 369 (1991)
- [35] M. Breeman, Ph.D. thesis, Rijksuniversiteit Groningen (1993)
- [36] R. van Gastel, Ph.D. thesis, Universiteit Leiden (2001)
- [37] R. van Gastel, M.F. Roşu, et al., Surf. Sci. **555**, 11 (2004)
- [38] R. van Gastel, E. Somfai et al., Nature **408**, 665 (2000)
- [39] R. van Gastel, E. Somfai et al., Phys. Rev. Lett. **86**, 1562 (2001)
- [40] J.W.M. Frenken, R. van Gastel, et al., Appl. Phys. A **75**, 11 (2002)
- [41] R. van Gastel, E. Somfai et al., Surf. Sci. **521**, 10 (2002)
- [42] E. Somfai, R. van Gastel et al., Surf. Sci. **521**, 26 (2002)
- [43] R. van Gastel, J.W.M. Frenken et al., The Chemical Physics of Solid Surfaces, vol 11, Surface Dynamics, ed. D.P. Woodruff, (Elsevier, Amsterdam, 2003), p. 351
- [44] H. Dürr, J.F. Wendelken, J.K. Zuo, Surf. Sci. **328**, L527 (1995)
- [45] J.J. de Miguel, A. Sánchez, et al., Surf. Sci. **189/190**, 1062 (1987)
- [46] M. Breeman, D.O. Boerma, Surf. Sci. **269/270**, 224 (1992)
- [47] H.-J. Ernst, F. Fabre, J. Lapujoulade, Phys. Rev. B **46**, 1929 (1992)
- [48] T. Maroutian, L. Douillard, H.-J. Ernst, Phys. Rev. B **64**, 165401 (2001)
- [49] J. Kallunki, J. Krug, M. Kotrla, Phys. Rev. B **65**, 205411 (2002)
- [50] J.C. Girard, S. Gauthier, et al., Surf. Sci. **301**, 245 (1994)
- [51] M. Giesen-Seibert, F. Schmitz et al., Surf. Sci. **329**, 47 (1995)
- [52] C.-L. Liu, Surf. Sci. **316**, 294 (1994)
- [53] O.S. Trushin, K.Kokko, et al., Phys. Rev. B **56**, 12135 (1997)
- [54] G. Boisvert, L.J. Lewis, Phys. Rev. B **56**, 7643 (1997)
- [55] L.S. Perkins, A.E. DePristo, Surf. Sci. **294**, 67 (1993)
- [56] T. Flores, S. Junghans, M. Wuttig, Surf. Sci. **371**, 1 (1997)
- [57] T. Flores, S. Junghans, M. Wuttig, Surf. Sci. **371**, 14 (1997)
- [58] M.L. Grant, B.S. Swartzentruber et al., Phys. Rev. Lett. **86**, 4588 (2001)
- [59] Th. Michely, C. Teichert, Phys. Rev. B **50**, 11156 (1994)
- [60] M. Morgenstern, Th. Michely, G. Comsa, Philos. Mag A **79**, 775 (1999)
- [61] G. Costantini, F. Buatier de Mongeot, et al., Phys. Rev. Lett. **86**, 838 (2001)

- [62] Th. Michely, M. Kalff, et al., *Phys. Rev. Lett.* **86**, 2589 (2001)
- [63] G. Rosenfeld, K. Morgenstern, et al., *Appl. Phys. A* **69**, 489 (1999)
- [64] M. Zinke-Allmang, L.C. Feldman, M.H. Grabow, *Surf. Sci. Rep.* **16**, 377 (1992)
- [65] W. Ostwald, *Z. Phys. Chem.* **34**, 495 (1900)
- [66] M. Eßer, K. Morgenstern, et al., *Surf. Sci.* **402-404**, 341 (1998)
- [67] D.C. Schlößer, K. Morgenstern, et al., *Surf. Sci.* **465**, 19 (2000)
- [68] M. von Smoluchowski, *Phys. Z.* **17**, 585 (1916)
- [69] L. Kuipers, R. W. M. Loos et al., *Rev. Sci. Instr.* **66**, 4557 (1995)
- [70] L. Kuipers, Ph.D. thesis, Universiteit van Amsterdam (1994)
- [71] M. S. Hoogeman, D. Glastra van Loon et al., *Rev. Sci. Instr.* **69**, 2072 (1998)
- [72] M. S. Hoogeman, Ph.D. thesis, Rijksuniversiteit Leiden (1998)
- [73] M. J. Rost, Ph.D. thesis, Universiteit Leiden (2001)
- [74] R. Young, J. Ward, F. Scire, *Rev. Sci. Instr.* **43**, 999 (1972)
- [75] G. Binnig, H. Rohrer et al., *Phys. Rev. Lett.* **49**, 57 (1982)
- [76] C.J. Chen, *Introduction to Scanning Tunneling Microscopy* (Oxford University Press, Oxford, 1993)
- [77] W.J. Kaiser, J.A. Stroscio, *Scanning Tunneling Microscopy* (Academic Press, Boston 1993)
- [78] M. J. Rost, L. Crama et al., *Rev. Sci. Instr.* **76**, 053710 (2005)
- [79] E. P. Th. M. Suurmeijer, Th. Mulder, J. Verhoeven, *Basisboek Vacuümtechniek* (Nederlandse Vacuümvereniging, 2000)
- [80] G.L. Kellogg, *Surf. Sci. Rep.* **21**, 1 (1994)
- [81] G. Ehrlich, *Surface Diffusion: Atomistic and Collective Processes*, M.C. Tringides, eds, NATO ASI Series B, Vol. 360, (Plenum Press, New York, 1997), p. 23
- [82] H.-C. Jeong, E.D. Williams, *Surf. Sci. Rep.* **34**, 171 (1999)
- [83] Z. Zhang, M.G. Lagally, *Science* **276**, 377 (1997)
- [84] M. Poensgen, J.F. Wolf et al., *Surf. Sci.* **274**, 430 (1992)
- [85] K. Morgenstern, G. Rosenfeld et al., *Phys. Rev. Lett.* **74**, 2058 (1995)
- [86] K. Morgenstern, E. Lægsgaard, F. Besenbacher, *Phys. Rev. Lett.* **86**, 5739 (2001)
- [87] O. Bénichou, G. Oshanin, et al., *Phys. Rev. E* **64**, 020103 (2001)
- [88] M.L. Anderson, N.C. Bartelt, B.S. Swartzentruber, *Surf. Sci.* **538**, 53 (2003)
- [89] J.B. Hannon, C. Klünker, et al., *Phys. Rev. Lett.* **79**, 2506 (1997)
- [90] R.J.I.M. Koper, Surface Preparation Laboratory, <http://www.surface-prep-lab.com>
- [91] R.G. Musket, W. McLean, et al., *Appl. Surf. Sci.* **10**, 143 (1982)
- [92] H. Brune, K. Bromann et al., *Phys. Rev. B* **52**, R14380 (1995)
- [93] X.Y. Wang, Z.Y. Pan, et al., *Surf. Sci.* **545**, 137 (2003)

- [94] C. Ratsch, A.P. Seitsonen, M. Scheffler, Phys. Rev. B **55**, 6750 (1997)
- [95] C. Ratsch, M. Scheffler, Phys. Rev. B **58**, 13163 (1998)
- [96] H. van Beijeren, R. Kutner, Phys. Rev. Lett. **55**, 238 (1985)
- [97] M.J.A.M. Brummelhuis, H.J. Hilhorst, J. Stat. Phys. **53**, 249 (1988)
- [98] Z. Toroczkai, Int. J. Mod. Phys. B **11**, 3343 (1997)
- [99] T.J. Newman, Phys. Rev. B **59**, 13754 (1999)
- [100] Topics in Current Physics, vol 7, Monte Carlo Methods in Statistical Physics, ed. K. Binder (Springer-Verlag, Berlin, 1979)
- [101] K. Binder, Rep. Prog. Phys. **60**, 487 (1997)
- [102] N. Metropolis, A.W. Rosenbluth, et al., J. Chem. Phys. **21**, 1087 (1953)
- [103] G.D. Birkhoff, Proc. Natl. Acad. Sci. **17**, 656 (1931)
- [104] W.H. Press, B.P. Flannery, Numerical Recipes in C: The art of Scientific Computing (Cambridge University Press, Cambridge, 1992)
- [105] G. Kresse, J. Hafner, Phys. Rev. B **47**, 558 (1993)
- [106] G. Kresse, J. Hafner, Phys. Rev. B **49**, 14251 (1994)
- [107] G. Kresse, J. Furthmüller, Comput. Mater. Sci. **6**, 15 (1996)
- [108] G. Kresse, J. Furthmüller, Phys. Rev. B **54**, 11169 (1996)
- [109] D. Vanderbilt, Phys. Rev. B **41**, 7892 (1990)
- [110] A. Pasquarello, K. Laasonen, et al., Phys. Rev. Lett. **69**, 1982 (1992)
- [111] K. Laasonen, A. Pasquarello, Phys. Rev. B **47**, 10142 (1993)
- [112] G. Kresse, J. Hafner, J. Phys.: Condens. Matter **6**, 8245 (1994)
- [113] J.P. Perdew, Electronic Structure of Solids '91, ed. P. Ziesche, H. Eschrig (Akademie Verlag, Berlin, 1991), p. 11
- [114] CRC Handbook of Chemistry and Physics 82nd edition 2001-2002, ed. D.R. Lide (CRC Press LLC, Boca Raton, 2001)
- [115] M.S. Hoogeman, M.A.J. Klik, et al., J. Phys.: Condens. Matter **11**, 4349 (1999)
- [116] Th. Michely, T. Land, et al., Surf. Sci. **272**, 204 (1992)
- [117] M. Li and J.W. Evans, Phys. Rev. B **69**, 035410 (2004)
- [118] P. Nozières, Solids far from Equilibrium, ed. C. Godrèche (Cambridge University Press, Cambridge, 1992), p.1
- [119] J. Lapujoulade, Surf. Sci. Rep. **20**, 191 (1994)
- [120] L.D. Landau, E.M. Lifschitz, Course of Theoretical Physics, vol 7, Theory of Elasticity (Pergamon Press, Oxford, 1959)
- [121] K.H. Lau, W. Kohn, Surf. Sci. **65**, 607 (1977)
- [122] L.E. Shilkrot, D. J. Srolovitz, Phys. Rev. B **53**, 11120 (1996)
- [123] M. Bernasconi, E. Tosatti, Surf. Sci. Rep. **17**, 363 (1993)

-
- [124] M. Giesen, G. Schulze Icking-Konert, Surf. Rev. Lett. **6**, 27 (1999)
- [125] M. Karimi, T. Tomkowski, et al., Phys. Rev. B **52**, 5364 (1995)
- [126] J.B. Hudson, Surface Science: An Introduction (John Wiley & Sons, New York, 1998)
- [127] G. Schulze Icking-Konert, M. Giesen, H. Ibach, Phys. Rev. Lett. **83**, 3880 (1999)
- [128] J.C. Russ, The Image Processing Handbook, 4th edition (CRC Press, Boca Raton, 2002)
- [129] J.W. Cooley, J.W. Tukey, Math. Comput. **19**, 297 (1965)
- [130] M.J.J. Jak, C. Konstapel, et al., Surf. Sci. **494**, 43 (2001)
- [131] P.V.C. Hough, Int. Conf. on High Energy Accelerators and Instrumentation, ed. L. Kowarski, (CERN, Genève, 1959)
- [132] R.D. Duda, P.E. Hart, Comm. ACM **15**, 11 (1972)

Living on the Edge: Birth, Life and Death of Surface Vacancies

On the smallest scale, metals are built up of atoms, regularly stacked in a crystal lattice. In this Thesis, we concentrate on the surface of a metal crystal, namely the (100) surface of copper: Cu(100). In particular, we focus on height variations that break up the surface into terraces that are bound by ledges, usually one atomic spacing high. Two sides of a step can be considered. The upper side, where the upper terrace ends, and the lower side at which a new terrace originates from underneath the upper terrace.

Previous experiments on the Cu(100) surface have shown that occasionally one single atom in the top layer of the crystal is missing. This leaves a void, the size of one atom, in the square surface grid. Such a void is called a surface vacancy. These surface vacancies can be displaced by a jump of one of the four neighboring atoms into the void. In contrast to what one might intuitively expect surface vacancies play a significant role in transport over surfaces; on Cu(100) they are more effective than adatoms. On average, every atom in the copper surface, investigated in this Thesis is displaced every ten seconds by the transit of a surface vacancy! The research described in this thesis is focused on unravelling the full life cycle of a surface vacancy.

The measurement devices with which the experiments, described in this thesis, were performed, are two so-called scanning tunnelling microscopes. Both have the special ability to compensate for large temperature changes during measurement. These microscopes and the experimental set-ups in which they are housed are described in chapter 2.

The life cycle of the surface vacancy starts with its birth. The locations at which surface vacancies are predominantly created are the upper side of a terrace ledge. The upper side is the delivery room for most surface vacancies. The creation of a surface vacancy on the lower side of a terrace ledge is very unlikely, albeit not impossible. The measurements and analysis that lead to this conclusion are described in chapters 3 and 4. From the work described in these two chapters, we can also con-

clude that the upper side of a terrace ledge is the location where surface vacancies predominantly end their life cycle. When surface vacancies reach the lower side of a terrace ledge, they are likely to "stay alive", returning back into the lower terrace. The lower side of a terrace ledge acts as an efficient mirror for surface vacancies.

Between birth and death, the surface vacancy moves through the terrace, each time changing places with one of its nearest neighbor atoms. The direction and timing of these exchanges are completely random, although the vacancy follows the directions of the surface grid. At room temperature, every second, on average 100 *million* exchanges take place. This exchange rate is too high to be followed even with the fastest possible scanning tunnelling microscope. Luckily, the rate at which these exchanges take place strongly depends on temperature. Cooling the sample down to $-196\text{ }^{\circ}\text{C}$ we can increase the average waiting time between exchanges to 7 seconds. This has enabled us to follow the motion of individual surface vacancies with the scanning tunnelling microscope.

Unfortunately, the rate of spontaneous creation of surface vacancies also strongly reduces when the temperature is dropped. We estimate that we would typically have to search the area of a small city to find *one* spontaneously created surface vacancy. This is a rather time-consuming business with a microscope that has a maximum field-of-view of one millionth of one millionth of a square meter. Instead, single surface vacancies were artificially created at the low temperature of $-196\text{ }^{\circ}\text{C}$ and their motion at this temperature was monitored with the scanning tunnelling microscope, as is reported in chapter 5 of this thesis. The results obtained in this chapter allow us to close the cycle and complete the picture of the birth, life and death of a surface vacancy in Cu(100).

In chapter 6, a special aspect of coarsening behavior is investigated that we observed during experiments on clusters of surface vacancies, so-called vacancy islands. During the equivalent coarsening of structures formed by atoms added *on top* of a surface, islands of these adatoms have been observed to move as a whole, which leads to collisions between these adatom islands and result in island merger. Surprisingly, vacancy islands merge prematurely. Long before two vacancy islands touch, the merging event takes place by a rupture of the surface between the two islands. The investigated surface of copper is under tensile stress. In chapter 6 it is argued how this tensile stress can be the cause of this peculiar merging behavior of vacancy islands.

Levend op het randje: Geboorte, leven en dood van oppervlakte vacatures

Metalen zijn op de kleinste schaal opgebouwd uit atomen, regelmatig gestapeld in een kristalrooster. In dit proefschrift richten we ons op het oppervlak van een metaalkristal, namelijk het (100) oppervlak van koper: Cu(100). De aandacht is voornamelijk gericht op hoogtevariëaties die het oppervlak opdelen in terrassen, begrensd door terrasranden. Deze hoogtevariëaties zijn meestal één atomaire afstand hoog. We beschouwen twee kanten van zo'n terrasrand. De bovenkant, waar het bovenste terras eindigt, en de onderkant, waar een nieuw terras ontspringt van onder het bovenste terras.

Uit voorgaande experimenten is gebleken dat op enkele plaatsen in een kristaloppervlak, één metaalatom ontbreekt. Zo'n lege positie in het vierkante rooster van het oppervlak, ter grootte van één atoom, wordt een oppervlakte vacature genoemd. Een vacature kan zich door het oppervlak verplaatsen doordat één van de vier naburige atomen in deze leegte springt. In tegenstelling tot wat men intuïtief zou verwachten, spelen deze vacatures een belangrijke rol in het transport over oppervlakken; op Cu(100) zijn ze daarbij effectiever dan individuele atomen op het oppervlak. Gemiddeld verandert ieder atoom in het onderzochte koperoppervlak eens per tien seconde van plaats door de passage van een vacature! In dit proefschrift wordt het onderzoek beschreven naar het verloop van de volledige levenscyclus van een vacature in een oppervlak.

De apparatuur waarmee de metingen, beschreven in dit proefschrift, zijn uitgevoerd, wordt gevormd door twee zogenaamde rastertunnelmicroscopen. De hier gebruikte microscopen hebben de speciale eigenschap dat ze grote temperatuurveranderingen tijdens het meten kunnen opvangen. Deze microscopen, en de opstellingen waar ze zijn ingebouwd, worden beschreven in hoofdstuk 2.

De levenscyclus van een oppervlaktevacature, begint bij de geboorte. De plaat-

sen waar het merendeel van de vacatures in een oppervlak worden gecreëerd, liggen aan de bovenzijde van een terrasrand. De bovenzijde van een terrasrand kan worden beschouwd als de kraamkamer voor oppervlaktevacatures. De vorming van een oppervlakte vacature aan de onderzijde van een terrasrand is onwaarschijnlijk, maar niet onmogelijk. De metingen en de analyse die leiden tot deze conclusie worden beschreven in hoofdstukken 3 en 4. Uit het werk, beschreven in deze hoofdstukken, kunnen we ook concluderen dat de bovenzijde van de terrasrand de locatie is waar het merendeel van de vacatures in een oppervlak hun levenscyclus beëindigt. Als een oppervlaktevacature de onderzijde van een terrasrand bereikt, is het zeer waarschijnlijk dat deze in "leven" blijft en weer terugkeert in het lager gelegen terras. De onderzijde van een terrasrand kan worden gezien als een effectieve spiegel voor oppervlakte vacatures.

Tussen geboorte en dood verplaatst de oppervlaktevacature zich door het oppervlak door steeds van plaats te wisselen met één van de meest nabijge buuratomen. De richting van deze sprongen en de tijdsduur tussen deze sprongen is volledig willekeurig, waarbij de vacature uiteraard wel de richtingen van het oppervlakerooster volgt. Bij kamertemperatuur vinden per seconde gemiddeld 100 miljoen van dit soort uitwisselingen plaats. Dit uitwisselingstempo is zelfs voor de snelst mogelijke rastertunnelmicroscopie te hoog om bij te kunnen houden. Gelukkig is de uitwisselingssnelheid sterk afhankelijk van de temperatuur. Door het preparaat af te koelen naar een temperatuur van $-196\text{ }^{\circ}\text{C}$, vertraagt het proces tot een gemiddelde wachttijd van 7 seconden tussen iedere uitwisseling. Hierdoor wordt het mogelijk met de rastertunnelmicroscopie de bewegingen van individuele oppervlaktevacatures te volgen.

Helaas wordt de frequentie waarmee vacatures spontaan in het oppervlak worden gecreëerd, sterk verminderd als de temperatuur daalt. We schatten dat we typisch een oppervlakte ter grootte van een kleine stad moeten afzoeken om één vacature te vinden. Gezien het maximale gezichtsveld van de rastertunnel microscopie van een miljoenste van een miljoenste vierkante meter, is dit een vrij tijdrovende bezigheid. In plaats daarvan hebben we bij een temperatuur van $-196\text{ }^{\circ}\text{C}$, kunstmatig vacatures gecreëerd. Met een raster tunnelmicroscopie konden hun bewegingen bij deze temperatuur gevolgd worden, zoals beschreven in hoofdstuk 5 van dit proefschrift. De resultaten, verkregen in dit hoofdstuk, vormen het sluitstuk waarmee we het beeld van de geboorte, het leven en de dood van een oppervlakte vacature in Cu(100) compleet maken.

In hoofdstuk 6 wordt een bijzonder aspect onderzocht van spontaan schaalvergrotingsgedrag, dat aan het licht kwam tijdens metingen aan clusters van oppervlakte vacatures, zogenaamde vacature-eilanden. Tijdens de vergelijkbare schaalvergroting van structuren gevormd door atomen die *bovenop* het oppervlak zijn geplaatst, is waargenomen dat eilanden van deze adatomen zich als geheel over het oppervlak bewegen, hetgeen aanleiding geeft tot botsingen tussen deze adatoomeilanden en resulteert in het samensmelten van eilanden. Tot onze verrassing, smelten vacature

eilanden vroegtijdig samen. Lang voordat de eilanden elkaar raken, scheurt het oppervlak tussen de twee eilanden open, resulterend in de fusie van de twee eilanden. Het onderzochte koperoppervlak staat onder trekspanning. In hoofdstuk 6 wordt beargumenteerd hoe deze trekspanning dit onverwachte fusieproces kan veroorzaken.

Curriculum Vitae

Op 9 mei 1978 ben ik geboren te Borculo. Na het behalen van mijn VWO diploma aan de Regionale Scholengemeenschap "t Rijks" te Bergen op Zoom in 1997, ben ik natuurkunde gaan studeren aan de Universiteit Leiden. Aan het eind van mijn studie, heb ik twee afstudeerstages gedaan. De eerste stage heb ik uitgevoerd aan de Universiteit Leiden bij de Grensvlak Fysica groep onder leiding van prof.dr. Joost Frenken. Daar heb ik, onder supervisie van dr. Marcel Rost de bewegingen van eendimensionale structuren op een goudoppervlak onderzocht. Mijn tweede afstudeerstage heb ik uitgevoerd bij de cluster "Mechanics, Heat and Particle Optics" van het Philips Research Laboratorium te Eindhoven. Onder supervisie van dr. Niels de Jonge, heb ik daar de veldemissie eigenschappen van koolstof nanobuizen onderzocht. Op 17 september 2002 ben ik bij prof.dr. Joost Frenken afgestudeerd.

Twee weken daarvoor ben ik als onderzoeker in opleiding in de Grensvlak Fysica groep begonnen met mijn promotieonderzoek. Het onderzoek dat ik tijdens mijn promotieperiode in het Kamerlingh Onnes Laboratorium verricht heb, staat beschreven in dit proefschrift.

Vanaf april 2007 ben ik werkzaam bij de unit Beleidsstudies van het Energieonderzoek Centrum Nederland (ECN).

Nawoord

Hoewel een proefschrift meestal op naam van één persoon staat, is de totstandkoming ervan vrijwel altijd teamwerk. Voor dit proefschrift is dat niet anders. Ik wil deze laatste pagina's van mijn proefschrift dan ook met alle plezier gebruiken om de mensen te bedanken, zonder wiens inzet dit werk niet voor u had gelegen.

Tijdens mijn promotieperiode heb ik vier Bachelor studenten mogen begeleiden. Ik kijk met veel plezier terug op de samenwerking met Thomas Beuman, Cor van Essen, Paul Ruijgrok en Jan-Willem Beenakker. Hun interesse, doorzettingsvermogen en verrassende inzichten hebben een belangrijke bijdrage geleverd aan dit promotieproject. Voor ieder van hen zal een bepaald deel van dit proefschrift dan ook bekend voorkomen. Naast deze Bachelor studenten, wil ik in het bijzonder ook de Master student Femke Tabak bedanken voor de fantastische hulp bij de afronding van de laatste experimenten.

Joost Frenken wil ik graag bedanken voor zijn rol als wetenschappelijk klankbord, evenals Marcel Rost die ik tevens wil bedanken voor zijn hulp met de STM elektronica.

De experimenten beschreven in dit proefschrift zouden niet mogelijk zijn geweest zonder professionele technische ondersteuning. Tijdens mijn promotieperiode ben ik in de gelukkige omstandigheid geweest, omringd te zijn door een aantal zeer goede experts. Het polijsten van het koperoppervlak werd verzorgd door René Koper. Ik wil Arie Kuijt, Arjen Geluk, Bert Crama, Dian van der Zalm, Els van Tol, Ewie de Kuyper, Fred Kranenburg, Hans van Kuyk, Leendert Prevo, Peter Schakel, Raymond Koehler, René Overgauw, Wilfred van der Geest en Willem Versluijs graag bedanken voor hun inzet. Daarnaast wil ik Laurens Geurts, Ruud Kuyvenhoven en Ruud Zweistra graag bedanken voor het oplossen van computerproblemen van een wat meer administratieve aard.

Voor alle vruchtbare discussies en ondersteuning bedank ik mijn (oud)vakgroeps-genoten Allard Katan, Amalia Stamouli, Amol Patil, Anne France Beker, Bas Hendriksen, Dionne Klein, Dirk van Baarle, Dong Guocai, Ellie van Rijsewijk, Elodie Fourné, Erwin Heeres, Geiske de Groot, Gert-Jan van Baarle, Jan Verhoeven, K.B. Jinesh, Kees Herbschleb, Maarten van Es, Marcelo Ackermann, Mark den Heijer, Merlijn van Spengen, Nico Koekoek, Namboodiri Pradeep, Richard van Rijn, Ste-

fania Bobaru, Sviatlana Bahatyrova, Tjerk Oosterkamp, Vincent Fokkema, Viviane Turq en Werner van Loo.

Tot slot wil ik graag mijn ouders Theo en Toos en mijn zus Kristine bedanken voor jullie onvoorwaardelijke steun en het vele geduld dat jullie al deze jaren met mij gehad hebben.

